Optical Two-Dimensional Fourier Transform Spectroscopy of Semiconductors

by

Tianhao Zhang

M.S., University of Colorado, 2002

B.S., University of Science and Technology of China, 1997

A thesis submitted to the

Faculty of the Graduate School of the

University of Colorado in partial fulfillment

of the requirements for the degree of

Doctor of Philosophy

Department of Physics

2008

This thesis entitled:
Optical Two-Dimensional Fourier Transform Spectroscopy of Semiconductors
written by Tianhao Zhang
has been approved for the Department of Physics

_____

Prof. Steven T. Cundiff

_____

Prof. Charles Rogers

Date _____

The final copy of this thesis has been examined by the signatories, and we find that
both the content and the form meet acceptable presentation standards of scholarly
work in the above mentioned discipline.

Zhang, Tianhao (Ph.D., Physics)

Optical Two-Dimensional Fourier Transform Spectroscopy of Semiconductors

Thesis directed by Prof. Steven T. Cundiff

Optical two-dimensional (2D) Fourier transform spectroscopy (FTS) is implemented in the near-IR regime and employed for the study of exciton dynamics, many-body interactions, and disorders in semiconductors. As the optical analog of multidimensional nuclear magnetic resonance, 2D FTS is based on a highly enhanced transient four-wave mixing (FWM) experiment. A FWM signal is generated by a non-collinear three-pulse sequence and heterodyne-detected with a reference to provide both amplitude and phase. With active interferometric stabilization and scanning, the evolution of FWM electric field is coherently tracked and presented on a 2D map of the absorption and emission frequencies. With capabilities that include disentangling congested spectra, identifying resonant coupling, isolating coherent pathways, determining inhomogeneous broadening, and separating complex spectra into real and imaginary parts, 2D FTS is a powerful tool to resolve problems in traditional FWM spectroscopies.

In a typical 2D spectrum of semiconductor quantum wells, diagonal peaks arise from exciton resonances and cross peaks represent their coupling, with features such as cross peak strength and absorption of continuum dominated by many-body interactions. Based on the modified optical Bloch equations with phenomenological terms including excitation-induced dephasing, excitation-induced shift, and local field effect, numerical calculations are performed to reproduce these features and determine the microscopic origin of many-body effects by comparing to the experimental amplitude and real part spectra. The dependence of 2D spectra on the excitation polarization is employed to further explore the many-body interactions. In comparison with microscopic calculations with contributions of Pauli blocking, Hartree–Fock approximation,

and higher-order Coulomb correlations, it is found that exciton correlations play the dominant role in the case of cocircular-polarized excitation. With an alternative 2D projection, Raman coherences between excited excitons are isolated. The experimental and calculated 2D spectra in this form also demonstrate the similar result on exciton correlations.

Dedication

This thesis is dedicated to my parents.

Acknowledgements

First and foremost, I would like to thank my advisor, Prof. Steve Cundiff, for his constant support, guide and encouragement throughout my graduate career. His expertise and deep insight in research have greatly enlightened me and advanced my work. His excellence and enthusiasm in science always motivate me to explore the nature further.

I also have a great gratitude to Prof. Charles Rogers, as well as Dr. Rich Mirin, Prof. David Jonas, and Prof. Dan Dessau on my thesis committee, for their invaluable advices and supports.

I am deeply grateful for the inspirations and contributions from our theory collaborators, including Prof. Torsten Meier (Universität Paderborn), Prof. Peter Thomas and Dr. Irina Kuznetsova (Philipps Universität, Marburg), as well as Prof. Shaul Mukamel and Dr. Lijun Yang (University of California, Irvine). The efficient exchanges of ideas and results with Irina and Lijun have been very beneficial and pleasant. I thank Dr. Rich Mirin (NIST) and Prof. Duncan Steel (University of Michigan) for high quality quantum well samples.

I appreciate the friendship and help from all the fellow Cundiff group members, past and present. Particularly I thank all my postdoctoral co-workers, Dr. Camelia Borca, Dr. Xiaoqin (Elaine) Li, and Dr. Alan Bristow, for their aids and encouragements. I am indebted to Ryan Smith and Alan Bristow for reading my thesis manuscript and valuable suggestions on writing. I also thank Loree Kaleth for the administrative

support.

JILA is an exceptional place for scientific research. I am grateful for the technical assistance from David Alchenberger and Tom Foote of the instrument shop, as well as Paul Beckingham, Terry Brown, and Mike Whitmore of the electronic shop in JILA.

I express my ultimate gratitude to my parents, for their lifelong love, care, and support.

Contents

Chapter

Appendix

Figures

Figure

Chapter 1

Introduction

In direct bandgap semiconductors at low temperatures, the optical properties near the fundamental gap are dominated by excitonic resonances, which correspond to the formation of bound electron and hole pairs. The carrier dynamics and coupling in semiconductors have been extensively studied by ultrafast optical spectroscopic methods, primarily transient four-wave mixing (FWM) [1]. Various experiments, including time-integrated, time-resolved, and spectrally-resolved FWM, have demonstrated that the many-body interactions among excitons and carriers dominate the nonlinear optical properties [2]. Phenomenological effects such as local field correction (LFC) [3], biexciton formation [4], excitation-induced dephasing (EID) [5], and excitation-induced shift (EIS) [6] describe the many-body interactions. Although conventional FWM spectroscopies have revealed rich information about excitons and carriers, there are some difficulties. Multiple electronic transitions can be simultaneously excited by broadband ultrafast pulses, resulting in a complicated oscillatory temporal evolution. Whether it is due to the quantum beats from resonant coupling, or the polarization interference of uncoupled oscillators often remains undetermined [7]. In addition, it is hard to isolate dynamical information from the mixed contributions of many quantum-mechanical coherent pathways in a one-dimensional spectrum. Moreover, there is an intrinsic ambiguity regarding the microscopic origins of many-body effects, as the manifestations of LFC, EID, EIS, and biexcitons are similar in FWM magnitude measurements.

Optical two-dimensional (2D) Fourier transform spectroscopy (FTS) based on, but surpassing, traditional FWM techniques is a promising tool to address these problems. As an optical analog of multidimensional nuclear magnetic resonance (NMR) spectroscopy [8], 2D FTS has been implemented for probing the vibrational and electronic states of molecular systems in the infrared (IR) and optical regimes [9, 10, 11, 12, 13, 14, 15]. Compared to traditional one-dimensional or non-Fourier transform two-dimensional spectroscopies, 2D FTS provides many advantages by coherently tracking signal phase evolution and presenting the correlation in two time periods. Congested spectra are spread out into two spectral dimensions, allowing identification of resonant couplings and isolation of coherent pathways. The preservation of phase information in 2D FTS leads to the separation of real and imaginary part spectra, making it possible to improve resolution of lineshapes and provide microscopic information unavailable in magnitude measurements. In 2D FTS, inhomogeneous broadening of the ensemble manifests itself as the diagonal elongation, leading to the separation of homogeneous and inhomogeneous linewidths. Inhomogeneous broadening can be determined to provide disorder information of the system. In contrast to NMR, optical 2D FTS provides snapshots of the coherent dynamics on the timescale of femtosecond. Besides, phase-matched directions can be employed in optical 2D FTS with non-collinear geometry, resulting in the separation of the signal from incident pulses and spatial isolation of coherent pathways. By selecting the phase-matched direction, the temporal ordering of excitation pulses, and the Fourier-transform time variables, different 2D projections can be produced for specific problems.

In 2D FTS experiments, excitation pulses are scanned with sub-optical-cycle step size and the signal phase is tracked coherently. Therefore high phase stability and pulse positioning accuracy are critical, especially for experiments in the near-IR or visible wavelength range. Various techniques have been developed to implement 2D FTS experiment, including diffractive optics [16, 17, 18, 19], femtosecond pulse shaping [20,

21, 22], and active phase stabilization [23, 24].

This thesis is focused on the implementation of 2D FTS and its applications in the study of exciton dynamics, many-body interactions, and disorders in semiconductors. The structure of this thesis is as follows. Chapter 2 is an introduction to the coherent optical properties of semiconductors. The concept of excitons in semiconductors and semiconductor nanostructures is presented, followed by discussions of the selection rules for optical transitions, the relaxation processes after optical excitation, the coherent optical spectroscopic techniques, as well as the experimental evidences for the dominance of many-body interactions in semiconductors.

In Chapter 3, the development of IR and optical 2D FTS from multidimensional NMR and the applications in the studies of vibrational and electronic states in molecular systems are first reviewed. Then the nonlinear response function, third-order polarization and double-sided Feynman diagrams are introduced. The principles of 2D FTS are presented and the advantageous features are discussed.

Chapter 4 covers the technical aspects of the 2D FTS experiments we have implemented. Details including FWM generation, the interferometric stabilization and scanning of delay, the retrieval of full signal information with Fourier transform spectral interferometry in heterodyne detection, the formation of 2D spectra, and the experimental determination of the global phase in 2D spectra are reviewed. The basic features in an amplitude 2D spectrum from a typical experiment are discussed.

In Chapter 5, the density matrix formalism and the optical Bloch equations with phenomenological modifications are introduced. Numerical calculations are performed to qualitatively reproduce the features in experimental data and demonstrate the dominance of many-body interactions. The calculated amplitude and real part spectra with different types of many-body effects are compared to the experimental spectra.

In Chapter 6, the formalism of a microscopic semiconductor theory is first introduced, followed by a discussion on the polarization dependence of 2D spectra. Ex-

perimental results of different polarization configurations are compared to microscopic calculations based on a one-dimensional tight binding model. The contributions of Pauli blocking, Hartree–Fock approximation, and Coulomb correlations beyond the Hartree–Fock limit are discussed.

An alternative form of 2D FTS that is able to isolate the Raman coherences between heavy-hole and light-hole excitons is presented in Chapter 7. Experimental 2D spectra with colinear and cocircular-polarized excitation are presented and compared to microscopic calculations with time-dependent Hartree–Fock approximation and beyond.

In addition, the 2D FTS approach is employed to study the electronic coupling and tunneling in asymmetric double quantum wells of different barrier thickness. The results are presented in Appendix A. The experimental study of exciton continuum states with 2D FTS is discussed in Appendix B.

Publications and conference presentations in frame of the thesis

Journal publications

[1] X. Li, T. Zhang, S. Mukamel, R. P. Mirin, and S. T. Cundiff, "Investigation of electronic coupling in semiconductor double quantum wells using optical two-dimensional Fourier transform spectroscopy," in preparation.

[2] L. Yang, T. Zhang, A. D. Bristow, S. T. Cundiff, and S. Mukamel, "Isolating excitonic Raman coherence in semiconductors using two-dimensional correlation spectroscopy," submitted to J. Chem. Phys.

[3] I. Kuznetsova, P. Thomas, T. Meier, T. Zhang, and S. T. Cundiff, "Determination of homogeneous and inhomogeneous broadening of quantum-well excitons by 2DFTS: An experiment-theory comparison," submitted to Phys. Stat. Solid.

[4] T. Zhang, I. Kuznetsova, T. Meier, X. Li, R. P. Mirin, P. Thomas, and S. T. Cundiff, "Polarization-dependent optical 2D Fourier transform spectroscopy of semiconductors," Proc. Natl. Acad. Sci. **104**, 14227 (2007).

[5] I. Kuznetsova, P. Thomas, T. Meier, T. Zhang, X. Li, R. P. Mirin, and S. T. Cundiff, "Signatures of many-particle correlations in two-dimensional Fourier-transform spectra of semiconductor nanostructures," Sol. Stat. Comm. **142**, 154 (2007).

[6] X. Li, T. Zhang, C. N. Borca, and S. T. Cundiff, "Many-body interactions in semiconductors probed by optical two-dimensional Fourier transform spectroscopy," Phys. Rev. Lett. **96**, 057406 (2006).

[7] C. N. Borca, T. Zhang, X. Li, and S. T. Cundiff, "Optical two-dimensional Fourier transform spectroscopy of semiconductors," Chem. Phys. Lett. **416**, 311 (2005).

[8] T. Zhang, C. Borca, X. Li, and S. T. Cundiff, "Optical two-dimensional Fourier transform spectroscopy with active interferometric stabilization," Opt. Expr. **13**, 7432 (2005).

Conference presentations

[1] T. Zhang, L. Yang, A. D. Bristow, S. Mukamel, and S. T. Cundiff, "Exciton Raman coherence revealed in two-dimensional Fourier transform spectroscopy of semiconductors," Quantum Electronics and Laser Science (QELS) Conference, San Jose, CA, May 4-9, 2008.

[2] T. Zhang, A. D. Bristow, I. Kuznetsova, T. Meier, P. Thomas, and S. T. Cundiff, "Direct determination of exciton homogeneous and inhomogeneous linewidths in semiconductor quantum wells with two-dimensional Fourier transform spectroscopy," Quantum Electronics and Laser Science (QELS) Conference, San Jose, CA, May 4-9, 2008.

[3] T. Zhang, I. Kuznetsova, T. Meier, P. Thomas, R. P. Mirin, and S. T. Cundiff, "Polarization-dependent optical 2D Fourier transform spectroscopy of quantum wells," Montana Meeting on Fundamental Optical Processes in Semiconductors (FOPS), Big Sky, MT, Jul. 23-27, 2007.

[4] T. Zhang, A. D. Bristow, S. T. Cundiff, L. Yang, and S. Mukamel, "Isolating excitonic Raman coherences using 2D Fourier transform spectroscopy," Montana Meeting on Fundamental Optical Processes in Semiconductors (FOPS), Big Sky, MT, Jul. 23-27, 2007.

[5] T. Zhang, X. Li, S. T. Cundiff, R. P. Mirin, I. Kuznetsova, P. Thomas, and T. Meier, "Experimental and theoretical studies of exciton correlations using optical two-dimensional Fourier transform spectroscopy," Quantum Electronics and Laser Science (QELS) Conference, Baltimore, MD, May 6-11, 2007.

[6] T. Zhang, X. Li, S. T. Cundiff, R. P. Mirin, and I. Kuznetsova, "Many-body interactions in semiconductors probed by optical two-dimensional Fourier transform spectroscopy," American Physical Society March Meeting, Denver, CO, Mar. 5-9, 2007.

[7] T. Zhang, X. Li, S. T. Cundiff, R. P. Mirin, and I. Kuznetsova, "Polarized optical two-dimensional Fourier transform spectroscopy of semiconductors," The 15th International Conference on Ultrafast Phenomena, Pacific Grove, CA, Jul. 31-Aug. 4, 2006.

[8] T. Zhang, X. Li, C. N. Borca, and S. T. Cundiff, "Probing the microscopic origin of many-body interactions in semiconductors using optical two-dimensional Fourier transform spectroscopy," Quantum Electronics and Laser Science (QELS) Conference, Baltimore, MD, May 22-27, 2005.

[9] T. Zhang, C. N. Borca, X. Li, and S. T. Cundiff, "Optical two-dimensional Fourier transform spectroscopy technique," Colorado Meeting on Fundamental Optical Processes in Semiconductors (FOPS), Estes Park, CO, Aug. 8-13, 2004.

Chapter 2

Coherent Optical Properties of Semiconductors

The rapid development of ultrafast lasers has paved the way to the coherent regime in semiconductors, in which the phase coherence established by optical excitation only exists on the timescale of a picosecond. The coherent behavior of excitons, electrons, and holes is critical to the understanding of many fundamental quantum mechanical processes [1]. These processes have profound influences on ultrafast electronic and optoelectronic device applications. Besides, the knowledge of carrier dynamics is essential for research activities recently emerging in coherent regime, such as quantum computing, coherent control, and ultrafast switching [25]. The carrier dynamics and coupling have been extensively studied by nonlinear optical spectroscopic tools, primarily transient four-wave mixing (FWM) and pump-probe experiments. Unlike dilute atomic systems, many-body interactions dominate the nonlinear response of semiconductors [26].

In Section 2.1, the concept of an exciton is introduced as the dominant feature for optics near band edge in direct bandgap semiconductors, followed by discussion of exciton properties in bulk semiconductor and quantum wells (Section 2.2). Then selection rules and optical excitations, including bound and unbound two-exciton states, are discussed in Section 2.3. The relaxation processes of optical excitation at different time scales is reviewed in Section 2.4, with a primary focus on the coherent regime of semiconductors. Common experimental techniques including time-integrated, time-resolved, and spectrally-resolved FWM are discussed in Section 2.5. The results of

many-body interactions in semiconductors probed with FWM experiments are reviewed in Section 2.6, with a discussion on the limits of conventional techniques.

2.1   Excitons in semiconductors

The electronic levels of a semiconductor with a periodic lattice can be canonically described by an energy band structure in momentum space. For a semiconductor in the ground state, the valence band is completely occupied by electrons and the conduction band is empty. During the optical excitation of a semiconductor with direct bandgap E_g, as shown in Fig. 2.1, a photon with sufficient energy ($\hbar\omega > E_g$) promotes an electron from a state (mostly p-like) in the valence band to a state (mostly s-like) in the conduction band. Simultaneously a vacancy is created in the valence band, which is referred as a "hole". Since the momentum of a photon can be neglected compared to that of electron or hole, the transition is essentially vertical ($\delta k = 0$). The Coulomb interaction between the excited electron and hole can be treated as a perturbation for excitations high into the conduction band. However, for excitations close to the fundamental bandgap, the attractive Coulomb force between an electron and a hole results in the formation of a bound state, known as an "exciton". The exciton can be treated as a quasi-particle, with the unbound electron-hole pairs being the continuum states. In general, excitons have a large oscillator strength and thus dominate the optical properties of direct bandgap semiconductors near band edge. The concept of quasi-particle is useful for describing basic excitation and linear response to weak external perturbations. However, the "residual" part of the Coulomb force, i.e. the interaction not accounted for in the formation of excitons, leads to the interaction between excitons and induces a nonlinear response. Excitons are usually classified into two types: Frenkel excitons of tightly-bound electron-hole pairs [27, 28], and Wannier excitons of less highly-correlated electrons and holes [29]. Excitons in semiconductors
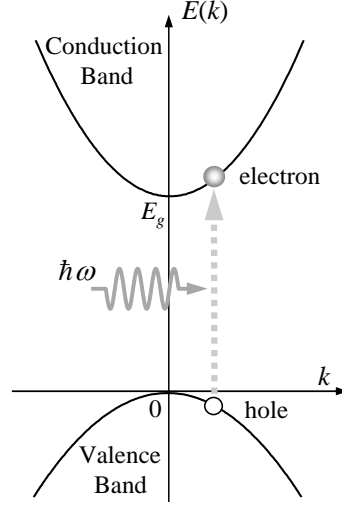
Figure 2.1: Optical excitation in a direct bandgap semiconductor. A photon promotes an electron from a valence state to a conduction state, simultaneously creating a "hole" in the valence band.

are generally the Wannier type with large radii [30].

With a structure similar to a hydrogen atom formed by an electron and a proton, an exciton presents a hydrogen-like energy level scheme. In the center-of-mass frame, the reduced mass of exciton is $\mu = m_e\, m_h/(m_e + m_h)$, and the total mass is $M = m_e + m_h$, where m_e and m_h are the respective electron and hole masses. The eigenvalues of the exciton energy are given simply by analogy with hydrogenic levels:

$$\tilde{E}(n) = -\frac{E_R}{n^2} \, , \qquad (2.1)$$

where n is the principal quantum number of the exciton, and E_R is the exciton Rydberg, i.e. the binding energy of the lowest state. E_R is determined by the reduced mass of exciton, μ, and the background dielectric constant, ϵ:

$$E_R = \frac{\mu e^4}{2\epsilon^2 \hbar^2} = \frac{\hbar^2}{2\mu a_B^2} \, , \qquad (2.2)$$

where $a_B = \epsilon \hbar^2 / \mu e^2$ is the exciton Bohr radius characterizing the space occupied by an exciton. The total energy of the exciton in the n-th excited state is a sum of the

bandgap, internal energy, and kinetic energy [2]:

$$E(n, \mathbf{k}) = E_g - \frac{E_R}{n^2} + \frac{\hbar^2}{2M}|\mathbf{k}|^2 \; , \qquad (2.3)$$

where $\mathbf{k} = \mathbf{k}_e + \mathbf{k}_h$ is the center-of-mass wavevector of exciton.

Due to the small reduced mass and large dielectric constant in background, excitons differ significantly from hydrogen atoms. The exciton binding energy is much weaker than that of the hydrogen atom and the distance between the electron and hole are quite large, according to Eqn. (2.2). Here are some typical numbers for excitons in bulk GaAs semiconductor: $E_g = 1.519\,\text{eV}$, $m_e = 0.067\,m_0$, $m_h = 0.51\,m_0$, where m_0 is the free electron mass, $\epsilon = 12.4$, $a_B = 11.0\,\text{nm}$, and $E_R = 4.2\,\text{meV}$ [31]. As the lattice constant of GaAs is $0.56\,\text{nm}$, the electron in an exciton is many lattice sites away from the hole, confirming that excitons in GaAs are the Wannier type [30].

Based on the bandgap picture of semiconductors, optical excitation and emission can be treated as a two-particle process, i.e. an electron in the conduction band and a hole in the valence band are created simultaneously in photon absorption and they can recombine radiatively to emit a photon. This treatment leads to a useful representation of the semiconductor system, known as the pair picture. In Fig. 2.2(a), where the exciton total energy $E(n, k)$ is plotted versus exciton center-of-mass wavevector k, the origin corresponds to the crystal ground state, and excitons of $n = 1, \; 2, \; 3, \ldots$ and electron-hole pairs are presented as excited states. An electron-hole pair is created along the photon line following the equation $E(k) = \hbar c k/n$, where c is the speed of light and n is the index of refraction. If the coupling between photons and excitons is included, the pair picture is then converted to the polariton picture. An anti-crossing feature occurs where the photon line and the exciton state intersect, resulting in an upper and a lower branch.

The pair picture helps explain the dominance of excitons in the optical response of semiconductors. The center-of-mass momentum of an exciton obtained by absorbing
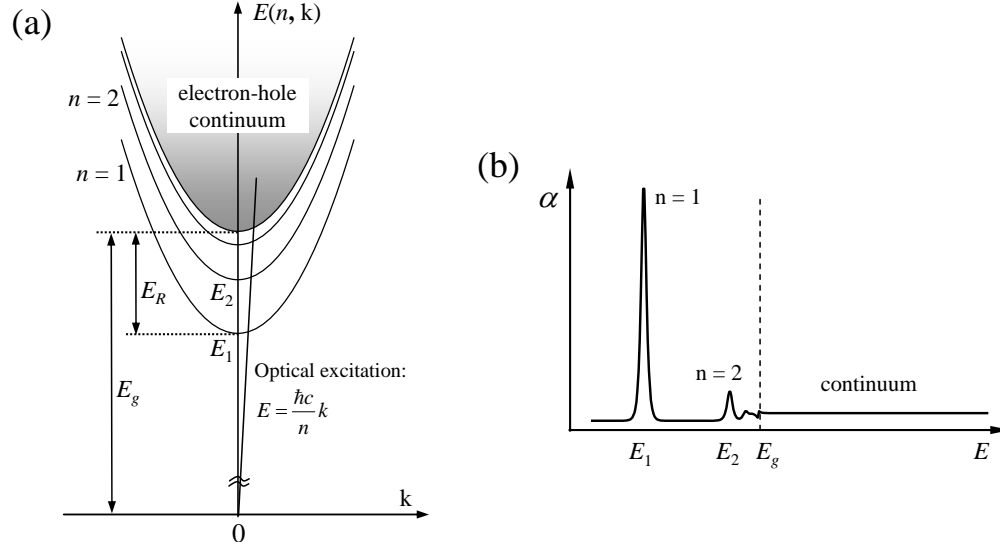
Figure 2.2: (a) The exciton total energy $E(n,k)$ versus the center-of-mass wavevector k (not to scale) and the photon line $E(k) = \hbar c k / n$; (b) A schematic figure of the linear absorption spectrum, with strong absorbing bound exciton states below bandgap.

a photon in the visible wavelength range is negligibly small compared to the extent of the first Brillouin zone, thus $\mathbf{k} \simeq 0$ in Eqn. (2.3). The photon energy needed to create an exciton bound state is less than the energy gap between the top of the valence and the bottom of the conduction band. In a schematic linear absorption spectrum depicted in Fig. 2.2(b) [31], strong hydrogenic absorption resonances corresponding to the $1s$, $2s$, ... bound excitons appear below the bandgap E_g, followed by the continuum absorption of electron-hole pairs. The continuum absorption approaches a finite value when photon energy $\hbar\omega$ decreases to E_g, instead of going to zero with a square-root law as the prediction of free-carrier theory. This difference is known as the Coulomb enhancement of continuum absorption [31]. The presence of discrete absorption lines below bandgap and enhanced absorption of electron-hole above bandgap is significantly different from the free-carrier absorption predicted with no Coulomb interaction between electrons and holes. Therefore the formation of excitons and electron-hole pairs by Coulomb interaction in semiconductors influences the linear optical response near band

edge prominently. The oscillator strength of absorption is determined by the overlapping of the electron and hole wavefunctions. Hence much larger absorption happens at bound exciton states rather than the unbound electron-hole pair states. The exciton oscillator strength $f(n) \propto 1/n^3$ for the n-th state, therefore the discrete resonance absorption decreases quickly with n. Experimentally, only the first a few lines are observable because of various broadening mechanisms, such as scattering of electron-hole pairs by phonons.

2.2 Semiconductor quantum wells

Two-dimensional heterostructures known as quantum wells can be readily fabricated with superior lattice quality by growth techniques such as molecular beam epitaxy (MBE) or metal organic chemical vapor deposition (MOCVD). In quantum wells, a layer thinner than the extent of the envelope wavefunction of electrons and holes is sandwiched between two barrier layers of another semiconductor with larger energy bandgap. If the barrier layers have sufficient thickness and energy gap, carriers will be confined in the low energy layer where they were created, but remain free to move around within that layer. One of the most widely used quantum well system consists of GaAs and $Al_x Ga_{1-x} As$ as well and barrier material, respectively [31]. The bandgap of $Al_x Ga_{1-x} As$ is larger than that of GaAs by about $0.5\,eV$, depending on the Al concentration. GaAs and $Al_x Ga_{1-x} As$ ($0 < x < 0.45$) are both direct-gap semiconductors of the zinc blende structure, with almost the same lattice constant [31]. The close lattice match reduces strain during growth and thus makes structures of many periods possible.

The wavefunction and energy levels of excitons in a quantum well are altered significantly due to the quantum confinement. The wavefunction in the growth ($\hat{\mathbf{z}}$) direction is compressed while it remains a plane wave in the in-plane ($\hat{\mathbf{x}}$-$\hat{\mathbf{y}}$) direction. The $\hat{\mathbf{z}}$-direction component is the solution to the quantum mechanical problem of a

particle in a box. With such modification to the system, the eigenvalues of the excitonic energy in an ideal two-dimensional case are:

$$\tilde{E}(n) = -\frac{E_R}{(n-\frac{1}{2})^2} \ , \tag{2.4}$$

and the Bohr radius is $(n-\frac{1}{2})\,a_B$. In addition, the exciton oscillator strength is $f(n) \propto 1/(n-1/2)^3$ for 2D excitons instead of $1/n^3$ for bulk. Thus the binding energy (oscillator strength) of $1s$ exciton in 2D case is four (eight) times that of the bulk exciton. The confinement greatly increases the exciton binding energy and absorption strength by improving the overlapping of electron and hole wavefunctions. Due to finite well and barrier thickness, excitons in real quantum heterostructures are not completely two-dimensional. A more realistic treatment of the confinement on excitonic states in quantum wells can be found in [32].

In GaAs quantum wells, while the electron states and wavefunctions in the conduction band are similar to those in bulk, the hole states and wavefunctions in the valence band are more complicated, since the valence band at the center of the Brillouin zone ($k=0$) is degenerate. For bulk GaAs with a cubic symmetry, the conduction band at the Brillouin zone center has s-orbital character with a two-fold degeneracy since the electron spin $J = \frac{1}{2}$. The valence band around $k=0$ has p-orbital character, which can be described by wavefunctions with a total angular momentum $J = \frac{3}{2}$ for the upper two sub-bands and $J = \frac{1}{2}$ for the lower sub-band. Known as the split-off band, the lower valence band is separated by $0.34\,\mathrm{eV}$ from the upper band at $k=0$ due to spin-orbit coupling. The two upper valence bands are referred as the heavy-hole (HH) and light-hole (LH) sub-bands, with projection of the angular momentum along $\hat{\mathbf{z}}$-axis J_z equal to $\pm\frac{3}{2}$ and $\pm\frac{1}{2}$, respectively.

The energy of valence bands has an anisotropic dependence on the direction of the wavevector k. The dispersion relations for HH and LH sub-bands near the center

of the Brillouin zone are [31]:

$$\varepsilon_{HH} = -(\gamma_1 - 2\gamma_2)\frac{\hbar^2 k_z^2}{2m_0} - (\gamma_1 + \gamma_2)\frac{\hbar^2 k_{xy}^2}{2m_0} \qquad \text{for} \quad J_z = \pm\frac{3}{2} \ , \qquad (2.5)$$

$$\varepsilon_{LH} = -(\gamma_1 + 2\gamma_2)\frac{\hbar^2 k_z^2}{2m_0} - (\gamma_1 - \gamma_2)\frac{\hbar^2 k_{xy}^2}{2m_0} \qquad \text{for} \quad J_z = \pm\frac{1}{2} \ , \qquad (2.6)$$

where k_{xy} and k_z are the respective in-plane ($\hat{\mathbf{x}}$-$\hat{\mathbf{y}}$ direction) and perpendicular ($\hat{\mathbf{z}}$ direction) component of the hole wavevector, in a frame defined by the corresponding quantum well geometry. m_0 is the free electron mass and γ_1 and γ_2 are the Luttinger parameters with values of $\gamma_1 \simeq 6.9$ and $\gamma_2 \simeq 2.4$ for GaAs [31]. The HH and LH sub-bands are degenerate at $k = 0$ in bulk GaAs. Consequently, the effective hole mass is also anisotropic and different for the two sub-bands: $m_{HH}^{xy} = m_0/(\gamma_1 + \gamma_2)$, $m_{HH}^z = m_0/(\gamma_1 - 2\gamma_2)$, $m_{LH}^{xy} = m_0/(\gamma_1 - \gamma_2)$, and $m_{LH}^z = m_0/(\gamma_1 + 2\gamma_2)$, where m_{HH}^{xy} and m_{HH}^z (m_{LH}^{xy} and m_{LH}^z) are the respective in-plane and perpendicular component of the hole mass in HH (LH) sub-band. The values of hole mass in the two sub-bands are $m_{HH}^z \simeq 0.5\,m_0$, $m_{HH}^{xy} \simeq 0.11\,m_0$, $m_{LH}^z \simeq 0.086\,m_0$, and $m_{LH}^{xy} \simeq 0.23\,m_0$. In quantum wells, the quantum confinement acts as a perturbation and lifts the degeneracy of the upper valence band, resulting in an energetic separation of the HH and LH sub-bands, as depicted in Fig. 2.3(a). The energy splitting of the two sub-bands near $k = 0$ is $\sim 10\,\text{meV}$ in a typical $10\,\text{nm}$ thick GaAs quantum well. The splitting is determined by the well thickness and increases as the thickness decreases. For optical excitation with pulse width larger than the splitting, excitons are formed by both HH and LH with electrons, commonly referred as HH and LH excitons.
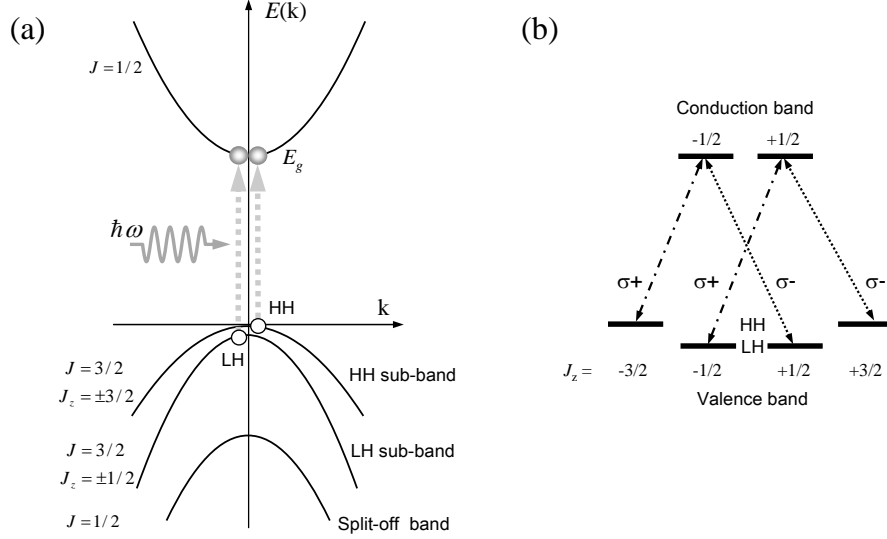
Figure 2.3: (a) The heavy-hole (HH) ($J = \frac{3}{2}, J_z = \pm\frac{3}{2}$), light-hole (LH) ($J = \frac{3}{2}, J_z = \pm\frac{1}{2}$), and split-off ($J = \frac{1}{2}$) sub-bands in the valence band of GaAs quantum wells; (b) Optical transitions between the HH and LH valence bands and the conduction band with σ^+ and σ^- circular-polarized light.

2.3   Optical transitions in quantum wells

A photon carries an angular momentum l of 1 in the dipole approximation. Due to the conservation of angular momentum, optical transitions obey the selection rule of $\Delta l = \pm 1$ for incident light perpendicular to the well plane. As the total exciton angular momentum contains contributions from the internal motion and envelope motion, the selection rule of transitions can be expressed as $\Delta l_{int} + \Delta l_{env} = \pm 1$, where l_{int} and l_{env} are the angular momentum of exciton internal and envelope motion, respectively. For dipole-allowed transitions, the only possible situation is $\Delta l_{int} = \pm 1$ and $\Delta l_{env} = 0$. This leads to a $J_z = \pm 1$ transition that occurs between a p-like valence band and an s-like conduction band, resulting in an exciton with an s-like envelope function.

In the optical excitation of a quantum well, only the electron and hole states at the center of Brillouin zone need to be considered, due to the negligible photon momentum. The upper valence band can be represented by a pair of $J_z = \pm\frac{3}{2}$ hole states for HH

sub-band and a pair of $J_z = \pm\frac{1}{2}$ hole states for LH sub-band, and the conduction band by a pair of $J_z = \pm\frac{1}{2}$ electron states, as depicted in Fig. 2.3(b). With right circular-polarized (σ^+) light, a transition can occur between $J_z = -\frac{3}{2}$ HH state and $J_z = -\frac{1}{2}$ electron state, or between $J_z = -\frac{1}{2}$ LH state and $J_z = \frac{1}{2}$ electron state, with respective transition dipole moment $\mu^{(-\frac{3}{2},-\frac{1}{2})}$ and $\mu^{(-\frac{1}{2},\frac{1}{2})}$. Similarly, transitions between $J_z = \frac{3}{2}$ HH state and $J_z = \frac{1}{2}$ electron state with dipole $\mu^{(\frac{3}{2},\frac{1}{2})}$, and between $J_z = \frac{1}{2}$ LH state and $J_z = -\frac{1}{2}$ electron state with dipole $\mu^{(\frac{1}{2},-\frac{1}{2})}$ happen with left circular-polarized (σ^-) light. The transition dipole moments for HH and LH excitons excited with left and right circular-polarized light can be expressed as [33]:

$$\mu^{(-\frac{3}{2},-\frac{1}{2})} = \mu_0\,\sigma^+ = \frac{1}{\sqrt{2}}\,\mu_0(\hat{\mathbf{x}} + i\hat{\mathbf{y}})\ , \tag{2.7}$$

$$\mu^{(-\frac{1}{2},\frac{1}{2})} = \frac{1}{\sqrt{3}}\,\mu_0\,\sigma^+ = \frac{1}{\sqrt{6}}\,\mu_0(\hat{\mathbf{x}} + i\hat{\mathbf{y}})\ , \tag{2.8}$$

$$\mu^{(\frac{3}{2},\frac{1}{2})} = \mu_0\,\sigma^- = \frac{1}{\sqrt{2}}\,\mu_0(\hat{\mathbf{x}} - i\hat{\mathbf{y}})\ , \tag{2.9}$$

$$\mu^{(\frac{1}{2},-\frac{1}{2})} = \frac{1}{\sqrt{3}}\,\mu_0\,\sigma^- = \frac{1}{\sqrt{6}}\,\mu_0(\hat{\mathbf{x}} - i\hat{\mathbf{y}})\ , \tag{2.10}$$

where μ_0 is the transition dipole modulus of HH excitons, and $\hat{\mathbf{x}}$ and $\hat{\mathbf{y}}$ are unit vectors. The transition dipole of LH excitons is $\frac{1}{\sqrt{3}}$ times that of HH excitons. The two transitions with either left or right circular-polarized light occur independently with each other, therefore the system in each case can be treated as a level scheme containing two separate two-level systems. For excitation with linear-polarized light, which is a combination of left and right circular-polarized light with equal intensity, there are two degenerate transitions between the HH state of $J_z = \pm\frac{3}{2}$ in the valence band and the conduction band, and two degenerate transitions between the LH state of $J_z = \pm\frac{1}{2}$ and the conduction band [4]. These transitions are coupled through the common electron state.

The "residual" Coulomb force between excitons, which is the part not accounted for in the formation of excitons, leads to the interactions of excitons. As a result of the

interactions, bound or unbound two-exciton states can be produced. When two excitons of opposite electron spins are close enough, they can form a bound state with lowered system energy, which is known as the biexciton [34]. On the other hand, two excitons of the same electron spins close to each other have a repulsive interaction, thus form an unbound two-exciton. There are two types of HH excitons: $(-\frac{3}{2}, -\frac{1}{2})$ and $(\frac{3}{2}, \frac{1}{2})$, and two types of LH excitons: $(-\frac{1}{2}, \frac{1}{2})$ and $(\frac{1}{2}, -\frac{1}{2})$ [33], labeled in the form of (J_z^v, J_z^c) by the hole state J_z^v and electron state J_z^c involved in the transition. Ten different kinds of two-exciton states can be formed: three from a pair of single HH excitons, labeled as f_H, three from a pair of single LH excitons, f_L, and four from a mixture of one HH exciton and one LH exciton, f_M [33]. The two-exciton $(-\frac{3}{2}, -\frac{1}{2})+(\frac{3}{2}, \frac{1}{2})$ is a bound state by two HH excitons, whereas $(-\frac{1}{2}, \frac{1}{2})+(\frac{1}{2}, -\frac{1}{2})$ is a bound state by two LH excitons, and $(-\frac{3}{2}, -\frac{1}{2})+(-\frac{1}{2}, \frac{1}{2})$ and $(\frac{3}{2}, \frac{1}{2})+(\frac{1}{2}, -\frac{1}{2})$ are two bound states of mixed excitons. Unbound states include four two-excitons formed by two identical excitons: a pair of $(-\frac{3}{2}, -\frac{1}{2})$ HH excitons, a pair of $(\frac{3}{2}, \frac{1}{2})$ HH excitons, a pair of $(-\frac{1}{2}, \frac{1}{2})$ LH excitons, and a pair of $(\frac{1}{2}, -\frac{1}{2})$ LH excitons, as well as two mixed pairs: $(-\frac{3}{2}, -\frac{1}{2})+(\frac{1}{2}, -\frac{1}{2})$ and $(\frac{3}{2}, \frac{1}{2})+(-\frac{1}{2}, \frac{1}{2})$.
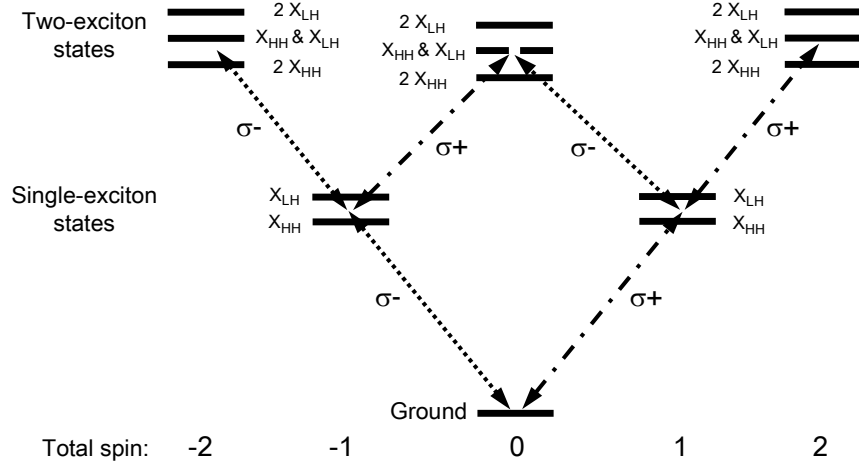
Figure 2.4: Exciton energy level scheme with doubly-excited states included and optical transitions with σ^+ and σ^- circular-polarized light.

In the exciton picture of energy level scheme depicted in Fig. 2.4, two-exciton states are included as doubly-excited states in addition to the ground state and two singly-excited HH and LH exciton states with spin $J_z = -1$ and 1 [4, 33]. A two-exciton state is presented at an energy level equal to the sum of the individual exciton transition energy plus an energetic shift [4]. For bound two-exciton states, the doubly-excited states are shifted lower by an amount equal to the biexciton binding energy, whereas the doubly-excited states of unbound two-excitons are shifted higher by the scattering energy. From left to right, the two-exciton states with total spin -2, labeled as $f_H^{(-2)}$, formed by a pair of identical $(\frac{3}{2}, \frac{1}{2})$ HH excitons, $f_H^{(0)}$ with total spin 0 by two HH excitons $(-\frac{3}{2}, -\frac{1}{2}) + (\frac{3}{2}, \frac{1}{2})$, and $f_H^{(2)}$ with total spin 2 by two identical HH excitons $(-\frac{3}{2}, -\frac{1}{2})$ are the three bottom levels of the doubly-excited states in Fig. 2.4. Mixed two-exciton states $f_M^{(-2)}$ with total spin -2 formed by HH exciton $(\frac{3}{2}, \frac{1}{2})$ and LH exciton $(\frac{1}{2}, -\frac{1}{2})$, $f_M^{(0)}$ with total spin 0 by HH exciton $(-\frac{3}{2}, -\frac{1}{2})$ and LH exciton $(\frac{1}{2}, -\frac{1}{2})$, and by HH exciton $(\frac{3}{2}, \frac{1}{2})$ and LH exciton $(-\frac{1}{2}, \frac{1}{2})$, and $f_M^{(2)}$ with total spin 2 by HH exciton $(-\frac{3}{2}, -\frac{1}{2})$ and LH exciton $(-\frac{1}{2}, \frac{1}{2})$ are the middle levels of two-exciton states. Two-exciton states $f_L^{(-2)}$ with total spin -2 formed by a pair of identical $(\frac{1}{2}, -\frac{1}{2})$ LH excitons, $f_L^{(0)}$ with total spin 0 by two LH excitons $(-\frac{1}{2}, \frac{1}{2}) + (\frac{1}{2}, -\frac{1}{2})$, and $f_L^{(2)}$ with total spin 2 by two identical LH excitons $(-\frac{1}{2}, \frac{1}{2})$ are the three top levels of the doubly-excited states.

Optical transitions between singly-excited states and doubly-excited states follow the same selection rule as that for the transitions between ground state and singly-excited states. The dipole-allowed transitions with σ^+ and σ^- circular-polarized light are depicted in Fig. 2.4, which gives a complete exciton picture of the transitions between valence band and conduction band with different circular-polarized light, including exciton interactions. In practice, different simplified models based on this picture are often used. For example, if the two-exciton states are totally neglected, an exciton picture with a ground state and four excitonic states are presented, equivalent to the electron picture in Fig. 2.3(b).

2.4   Relaxations of optical excitations

In this section, we discuss the time scales of relaxation processes following optical excitations in semiconductors. After a semiconductor is excited from thermodynamic equilibrium by an ultrafast pulse, several stages of relaxation occur until it returns to thermodynamic equilibrium. These processes include coherent relaxation, non-thermal relaxation, hot-carrier relaxation, and isothermal relaxation, in four temporally overlapped regimes [2].

The coherent regime starts right after an excitation and occurs on a time scale of picoseconds. The excitation creates a well-defined phase relation within the excited ensemble and with the incident field. Unlike atomic and molecular systems, scattering processes are so fast in semiconductors that the phase coherence is destroyed within picoseconds. Therefore, the study of coherence phenomena in semiconductors was deferred until the generation and application of ultrafast laser pulse were widely available. Many fundamental quantum mechanical processes take place in the coherent regime and have profound influences on the behaviors of excitons, electrons, and holes in the scattering.

Following the coherent regime, the distribution of excitons or free electron-hole pairs is usually non-thermal, i.e., the distribution function can not be characterized by a temperature. Non-thermal scattering processes of excitons and carriers can also be probed by optical spectroscopy. The non-thermal relaxation lasts several picoseconds. Carrier or exciton scattering can redistribute the energy within the carrier or exciton system and eventually leads to the hot-carrier regime with a thermalized distribution characterized by a temperature. This temperature is higher than the lattice temperature and can be different for subsystems of electrons, holes and excitons. The time of thermalization with lattice depends strongly on many factors, such as the interactions with phonons, thus the hot-carrier regime varies largely on timescale from several

picoseconds to hundreds of picoseconds. At the end of the hot-carrier regime, all carriers, phonons and excitons are in an equilibrium that can be described by the same temperature as that of the lattice. In the isothermal relaxation, the excess electrons and holes, or excitons recombine either radiatively or non-radiatively and return the semiconductor back to thermodynamic equilibrium.

In this work, we are focused on the coherent spectroscopic properties of semiconductors with ultrafast optical excitations. The third-order polarization $P^{(3)}$ created by the electromagnetic field of the excitation pulse is initially in phase with the field. The decay of phase coherence happens immediately after the excitation as the result of coupling to the "bath", in the Markovian limit. The characteristic time of phase relaxation, T_2, is called the decoherence time, also known as the dephasing time. Processes that destroy the phase coherence of the polarization include scattering with phonons, elastic and inelastic exciton-exciton or exciton-electron scattering, as well as scattering at impurities and crystal defects (including interface roughness and alloy fluctuations) [35]. The coherence is lost ultimately in the recombination process, which can be described by an exponential decay of the population with a lifetime T_1. Since the decoherence time T_2 describes the amplitude decay of polarization, we can derive a relation of $T_2 \leqslant 2T_1$, which gives the upper limit of T_2 as $2T_1$, in the case that no other phase destroying process but recombination happens. In general, T_2 is much smaller than $2T_1$ due to the various scattering processes in semiconductors. To characterize these scattering processes but excluding the recombination, a "pure" dephasing time T_2' can be defined with [35]:

$$\frac{1}{T_2} = \frac{1}{2T_1} + \frac{1}{T_2'} \, , \tag{2.11}$$

where T_2' is usually small for the fast scattering processes.

Linewidth broadening of the exciton resonance is common in semiconductor bulk and quantum wells. In the case of homogeneous broadening, all oscillators in the en-

semble have exactly the same resonant frequency. Therefore the polarization of every oscillator and the ensemble decays at the same rate T_2. The linewidth of the Lorentzian resonance (homogeneous linewidth) is $\Gamma_h = \hbar/T_2$, in energy units. In contrast, every oscillator in an inhomogeneous broadened system has a slightly different eigenfrequency, which follows a distribution within an interval of $\delta\omega$ centered at the resonant frequency ω_0. The polarization decay of the ensemble is faster than the decoherence of individual oscillator. All oscillators in the ensemble are in-phase when it is excited by an optical field. A phase distribution between oscillators develops with time as the result of different eigenfrequencies, causing the cancellation of polarizations from individual oscillators. The dephasing of the ensemble can be characterized roughly by a time constant $T_2^* \simeq 1/\delta\omega$, which is shorter than the decoherence time T_2 of individual oscillators. The amplitude of the emitted field from an ensemble of inhomogeneously broadened oscillators decays with T_2^*. Inhomogeneous broadening dominates in semiconductor alloys or quantum wells at low temperatures, where disorder due to composition or well thickness fluctuations localizes excitons. In high quality bulk samples or at elevated temperatures, the homogeneous broadening overwhelms inhomogeneous broadening as the result of inelastic scattering of free excitons with optic and acoustic phonons. In nonlinear spectroscopic experiments such as transient FWM, it is possible to distinguish different mechanisms of broadening and obtain the decoherence time T_2, even in the presence of inhomogeneous broadening.

2.5   Nonlinear optical spectroscopies of semiconductors

The study of the coherent dynamical response of semiconductors is only possible with ultrafast spectroscopic techniques of picosecond or femtosecond time resolution. Transient FWM and pump-probe experiments are the primary nonlinear spectroscopic methods commonly used to probe the nonlinear properties of various systems. FWM

measurements are sensitive to the coherent response, whereas pump-probe experiments can study both coherent and population dynamics.

In a generalized form of transient FWM experiments, three successive incident pulses of either different or the same frequency are used to excite a medium. The first pulse, with a wavevector $\mathbf{k}_1$, induces a polarization, i.e., a coherent superposition between the ground and excited states in the medium. The second pulse of wavevector $\mathbf{k}_2$, arrives after a delay and converts the superposition into a population. The amplitude of the population is maximal where the electric field of the second pulse interferes constructively with the polarization created by the first pulse, and minimal where they interfere destructively, forming a dynamic amplitude grating with a spatial period of $\mathbf{k}_2 - \mathbf{k}_1$. The third pulse of wavevector $\mathbf{k}_3$, arrives with a delay after $\mathbf{k}_2$ and is scattered by the dynamic grating into the phase-matched direction $\mathbf{k}_s = -\mathbf{k}_1 + \mathbf{k}_2 + \mathbf{k}_3$ as the FWM signal. The nonlinear FWM signal depends on the pulse ordering and interpulse time delays. Dynamics of the excited system can be studied by varying pulse delays. The time period between the first and second pulses reflects the coherent evolution of polarization generated by the first pulse, therefore it is called the evolution time τ. The period between the second and third pulses corresponds to the population relaxation of the excited states, usually named as the waiting time T. The time-domain behaviors of FWM as a function of τ and T provide essential information on the dynamics of polarization and population relaxation. In a simplified configuration, FWM can be generated with two pulses where the second pulse functions as both the second and third pulses in a three-pulse experiment, thus the waiting time T is always zero.

In a simple form of pump-probe spectroscopy, the medium under investigation is excited by a pump pulse and the induced changes are measured by another pulse, the probe, with a delay relative to the pump. Linear responses of the probe, such as absorption, reflectivity, Raman scattering, and luminescence are recorded and compared to the case without a pump. The probe is usually much weaker than the pump to avoid
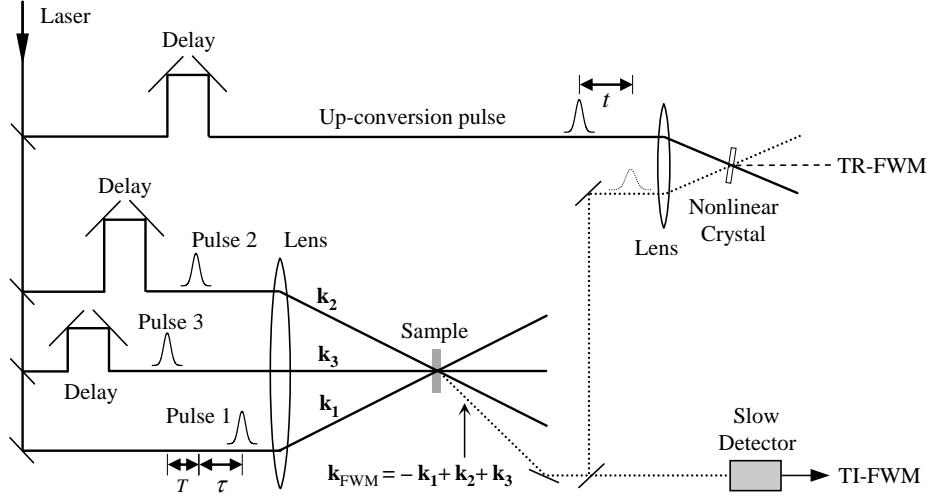
Figure 2.5: Experimental setup of three-pulse FWM generation and time-integrated (TI) and time-resolved (TR) signal detection. The signal can be measured with a slow detector for TI FWM or up-converted with a reference pulse in a nonlinear crystal for TR FWM.

introducing additional nonlinearities.

A generic FWM experimental configuration is illustrated in Fig. 2.5, where the nonlinear signal is generated by three pulses with adjustable delays τ and T. The FWM signal is commonly detected by a slow detector for the integral of signal intensity with varying delay τ, called time-integrated (TI) FWM signal. TI FWM can be expressed as:

$$S_{\mathrm{TI}}(\tau) \propto \int_0^{+\infty} |P^{(3)}(t,\tau)|^2 dt \; , \qquad (2.12)$$

where t is the signal emission time, and $P^{(3)}(t,\tau)$ is the macroscopic third-order polarization. The signal can also be measured by up-conversion with a reference in a nonlinear crystal to obtain the time-resolved (TR) FWM as a function of the real time t. TR FWM has the form:

$$S_{\mathrm{TR}}(t,\tau) \propto \int_{-\infty}^{+\infty} |P^{(3)}(t',\tau)|^2 |E(t-t')|^2 dt' \; , \qquad (2.13)$$

where $E(t)$ is the electric field of the reference. For dilute atomic systems, the temporal

behavior of TI-FWM as a function of delay τ is same as that of TR FWM as a function of the real time t. The signal spectrum can also be measured to obtain the spectrally-resolved (SR) FWM:

$$S_{\mathrm{SR}}(\omega_t, \tau) \propto \int_{-\infty}^{+\infty} |P^{(3)}(t,\tau)|^2 e^{i\omega_t t} dt ,\qquad(2.14)$$

where ω_t is the emission frequency. Moreover, it is often desirable to obtain the full information of the emitted signal including phase, for a complete characterization of the nonlinear signal. This can be accomplished by a technique known as Fourier transform spectral interferometry [36]. The signal to be measured is collinearly combined with a reference pulse, whose spectrum is well-characterized and overlapped with that of the signal, to produce a spectral interferogram. Fourier transform analysis of the interferogram allows the determination of signal amplitude and phase in temporal and spectral domains. This heterodyne detection technique is commonly used for the phase characterization of nonlinear signals. In Chapter 4, we will discuss the details of heterodyne detection of the FWM signal implemented for experiments of two-dimensional Fourier transform spectroscopy.

The exciton dynamics and coupling in semiconductor bulk and nanostructure materials have been extensively studied by nonlinear optical spectroscopic tools, primarily FWM experiments. It has been revealed that the interactions among elementary optical excitations (excitons and electron-hole pairs) have profound influences on the coherent nonlinear optical response. In the following section, we review the studies of exciton many-body interactions in semiconductors.

2.6   Many-body interactions in semiconductors

The many-body problem in condensed-matter systems is a fundamental topic with longstanding and continuing interest. Optically excited semiconductors provide

a convenient system for the study of many-body effects [26]. In the case of dilute atomic systems, the coherent phenomena are well understood since only independent atoms need to be considered. A simple picture such as a two-level scheme is usually adequate to describe the system. In materials such as semiconductors, many-body interactions make dramatic differences from the atomic limit and often dominate the carrier behaviors. It is essential to study these effects for a better understanding of the fundamental quantum mechanical processes and the influence on the performance of optoelectronic devices.

The manifestation of many-body interactions in the nonlinear response of semiconductors has been revealed by many experimental signatures. Exciton dephasing in quantum wells was studied by TI FWM experiments [37, 38] and interpreted on the basis of a two-level model developed by Yajima and Taira [39]. The appearance of a signal for "negative" delay in a two-pulse TI FWM experiment [40] is the first demon-
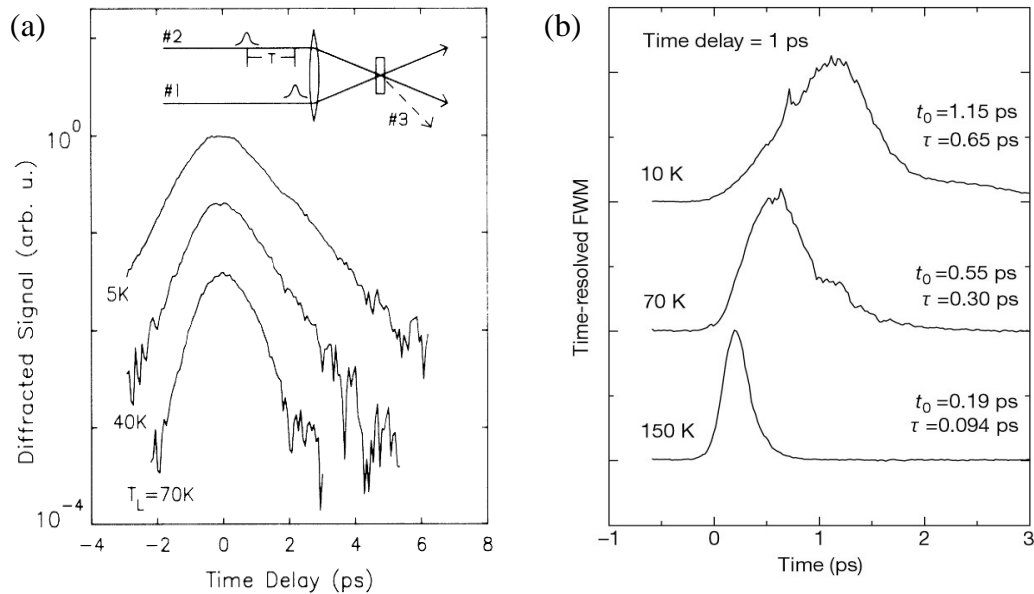
Figure 2.6: (a) A strong signal for negative time delay in two-pulse TI FWM. Reproduced from K. Leo et al., Phys. Rev. Lett. **65**, 1340-1343 (1990); (b) Delayed FWM peaks in two-pulse TR FWM. Reproduced from D.-S. Kim et al., Phys. Rev. Lett. **69**, 2725-2728 (1992).

stration that the nonlinear response of semiconductors is completely different from that of non-interacting two-level systems. As depicted in Fig. 2.6(a), TI FWM from a high quality GaAs quantum well sample was measured at different lattice temperatures. The TI FWM signal in the phase-matched direction $2\mathbf{k}_2 - \mathbf{k}_1$ was displayed as a function of pulse delay τ, which is considered positive (negative) when pulse $\mathbf{k}_1$ precedes (follows) pulse $\mathbf{k}_2$. A signal on a time scale much longer than the laser pulse width was observed for negative time delay ($\tau < 0$), with a time constant for the rise equal to half of that for the decay. This surprising result is in qualitative contrast to the expectation of no signal for negative delay from a non-interacting two-level system. Negative delay signals were also observed in experiments on dense systems including molecular iodine [41] and atomic potassium [42]. Further surprising results were found in TR FWM experiments [43, 44]. As shown in Fig. 2.6(b), the peak of a TR signal appears at a delayed time that is extremely long (as much as 10 times the pulse width). The delay decreases quickly with increasing temperature and shows no dependence on pulse delay τ, in dramatic contrast to the photon echo behavior of two-level atomic systems with inhomogeneous broadening. The asymmetric temporal evolution and the fact that the signal delay decreases with temperature indicate the signal is not a photon echo. Detailed analysis shows the delayed signal is from the diffraction of the polarization, rather than the diffraction of the field. The TI signal for negative time delay and the delayed peak in TR signal demonstrate that the nonlinear response of semiconductors differs completely from that of non-interacting two-level systems.

These behaviors were explained in terms of a local field effect resulted from Coulomb interactions in semiconductors [3]. Excitons can sense not only the electric field of the incident light, but also the field of all other excitons in the semiconductor, thus the effective field needs to be corrected to reflect the change by excitation. In a two-pulse experiment on a non-interacting two-level system, the FWM signal emitted in the $2\mathbf{k}_2 - \mathbf{k}_1$ direction is produced by an interaction between the polarization created

by the first pulse, $\mathbf{k}_1$, and the field of the second pulse, $\mathbf{k}_2$, thus resulting in no signal when they do not overlap at $\tau < 0$. In semiconductors, however, polarizations created by two pulses can interact with each other due to the interaction between incident field and excitons. Since polarizations persist for a duration of the dephasing time after the electric field, they can overlap at a negative τ to produce a FWM signal. In addition, the diffraction of polarization leads to a TR FWM signal that increases with time and peaks at a delay determined by the dephasing time. That is why the signal in TR FWM experiments presents a delayed peak that is not a photon echo.

The dephasing time of excitons measured by TI FWM experiments is influenced by many-body interactions. The homogeneous linewidth displays a linear dependence on exciton or free carrier densities created by pre-excitation [45]. The broadening by exciton-free carrier interaction is about eight times bigger than that by exciton-exciton interaction. Also the electron-exciton scattering is more efficient than hole-exciton scattering. Exciton interactions are stronger in quantum wells due to the reduced screening in two dimensions [45]. The differential transmission spectrum at a relatively low exciton density is characterized primarily by broadening of the exciton resonance resulting from exciton-exciton interaction [5]. The excitation-induced dephasing (EID), i.e., the density dependence of T_2, has a strong contribution to TI FWM signal excited by colinear-polarized light but no contribution in cross-linear-polarized excitation. The dephasing rate depends linearly on density at low densities and saturates at higher. EID allows the diffraction of polarization [46], therefore it is also a possible reason for the delayed signal in TR FWM.

A strong biexcitonic contribution to the TR FWM signal from GaAs quantum wells was observed [47]. Biexciton effects are closely related to problems such as polarization-dependent properties of FWM [4], quantum beat behaviors, and TI FWM signal at negative delay, in experiments including grating-induced biexcitonic FWM signals, biexcitonic quantum beats, and two-photon coherence. Excitation-induced shift

(EIS) was observed in SR FWM and confirmed with spectrally-resolved differential transmission [6]. EIS can result in a signal comparable to or stronger than that arising from saturation, local fields, or EID in semiconductors.

Coupling between optically induced excitations was also addressed. Beating in the FWM signal was observed as a result of the interference of excitons with slightly different quantum confinement energy due to well width fluctuations [48]. To distinguish whether the beats from disordered quantum wells were quantum beats or electromagnetic interference, TR FWM [7] and SR FWM [49] experiments were performed. Interference between the exciton resonance and unbound electron-hole pairs was also observed [50]. The coupling of excitons and continuum states by many-body interactions was discovered in partially-non-degenerate FWM [51] and three-pulse FWM measurements [52, 53]. These results explained the earlier observation that the FWM signal from excitons decays anomalously fast when the excitation spectrum overlapped continuum states [54].

These effects all resulted from the many-body interactions among excitons and carriers in semiconductors. The theoretical description of these phenomena requires a sophisticated model rather than an independent two-level scheme of atomic systems. Phenomenological terms for local field correction, EID, EIS, and biexciton formation are added in the optical Bloch equations of the two-level model to describe the experimental observations [6]. However, there is an intrinsic ambiguity regarding the microscopic mechanism of many-body interactions underlying the nonlinear response. The manifestations of local field, EID, EIS, and biexciton formation in FWM signal are similar, making it difficult to determine the microscopic origin of the interactions. The ambiguities come from the fact that TI or TR FWM experiments only measure the intensity of the signal, thereby discarding the essential information encoded in the phase. Furthermore, conventional FWM techniques have other limitations. Many electronic resonances could be excited simultaneously by broadband ultrafast pulses, leading to a

complicated oscillatory temporal evolution. It is difficult to distinguish whether such oscillations arise from polarization interference of uncoupled oscillators or quantum beats of coupled resonances. In addition, many quantum mechanical pathways with various relaxation times contribute to the FWM signal. It is hard to separate different dynamical information from these mixed contributions. Two-dimensional Fourier transform spectroscopy (2D FTS), a highly enhanced FWM technique that tracks coherent phase evolution, could resolve the aforementioned problems and provide microscopic information about the interactions [55].

Chapter 3

Principles of Optical Two-Dimensional Fourier Transform Spectroscopy

Optical two-dimensional (2D) Fourier transform spectroscopy (FTS) originates conceptually from the revolutionary development of multidimensional nuclear magnetic resonance (NMR) in the 1970s [8]. Compared to traditional one-dimensional or non-Fourier transform two-dimensional spectroscopic approaches, 2D FTS provides many advantageous features by coherently tracking phase evolution and correlating it in two frequency dimensions. Congested spectra are spread out into two dimensions to allow isolation of coherent pathways and identification of resonant couplings. Furthermore, the preservation of phase information in 2D FTS enables the separation of real and imaginary part spectra, making it possible to improve resolution of lineshapes and provide microscopic information unavailable in magnitude measurements. These powerful features make optical 2D FTS a very promising tool for probing the structure and dynamics of complex systems including liquids [9, 11, 15], chemical and biological molecules [10, 12, 13, 14], and semiconductors [24, 56, 55, 57]. The experimental and theoretical progress in 2D infrared (IR) and optical spectroscopy is presented in a recent perspective by Hochstrasser [58], along with the challenges that can be addressed by these advances.

In this chapter, the development of IR and optical 2D FTS from multidimensional NMR and the applications for vibrational and electronic dynamics of molecular

systems are first reviewed in Section 3.1. In the following section, the nonlinear response function for optical excitation and the third-order polarization are discussed. Double-sided Feynman diagrams are introduced in Section 3.3 as a diagrammatic description of quantum mechanical coherent pathways in Liouville space that contribute to the non-linear polarization. The principles of 2D FTS are presented in Section 3.4, followed by a discussion of the advantageous features that 2D technique offers in Section 3.5.

3.1   Development of IR and optical 2D FTS

The extension of Fourier transform spectroscopy into multidimensions revolution-ized nuclear magnetic resonance spectroscopy ultimately by producing fundamentally new types of spectra [8]. The first implementation of the Fourier transform approach to 2D magnetic resonance was demonstrated by the Ernst group in 1976 [59]. It was soon recognized that 2D NMR spectra contain valuable molecular phase information not available in double resonance experiments [60]. In a 2D NMR spectrum that measures the immediate response of excited spins, spin coupling between nuclei connected with chemical bonds provides information on bond lengths and bond angles, while spin flip transfer can be used to determine distances between nuclei without bond connections. In vibrational 2D NMR, cross peaks reveal the connectivity of adjacent bonds while the time dependence of vibrational relaxation could map out longer range structures.

The radio-frequency 2D NMR was rapidly extended to 2D FT microwave spec-troscopy [61, 62], 2D FT Raman spectra of magnetic sublevels in atomic vapors [63, 64], and 2D IR spectroscopy [65, 66, 67]. In early 2D IR spectra, an outer product was used to display correlation among a series of perturbed 1D optical spectra [66], without information on spectral relaxation. The second-harmonic phase-matching map of a non-linear crystal was measured in two dimensions of the sum and difference frequencies [68]. Tanimura and Mukamel proposed femtosecond vibrational 2D Raman spectroscopy [9],

which was followed by experimental implementations [11, 12, 69]. However, it was found that cascaded third-order processes were contributing to the the fifth-order response and masking the real fifth-order process when Raman excitation was used [12]. Doubly vibrationally enhanced FWM was also used to generate 2D vibrational spectra [70]. Direct excitation in IR was then utilized to obtain better results on vibrations [13, 14]. Similar to NMR, structural information about molecules can be obtained by studying the coupling between the IR active vibrational modes. The anharmonic nuclear potential and correlated fluctuations in the transition energies of two coupled molecular vibrations were studied by 2D IR spectroscopy [71, 72]. The absorptive correlation spectrum was obtained by summing complementary spectra of two vibrational coherences that oscillate with conjugate frequencies in the initial evolution time period [73].

2D electronic spectroscopy was introduced and investigated by Jonas and co-workers [10, 74, 75, 76, 77]. 2D electronic spectra of the dye IR144 in methanol were measured at shorter wavelengths. Separate real absorptive and imaginary dispersive spectra were obtained and compared to theoretical predictions [10, 76]. Electronic couplings in the molecular complex of photosynthetic protein were also studied by 2D FTS in the visible range [78, 79, 80]. The development of vibrational and electronic 2D FTS was reviewed by Mukamel et al. [81, 82, 83, 84] and Jonas [85].

Dynamic hole burning was used in early 2D spectroscopic studies of vibrational transitions [86, 87]. A narrowband mid-IR pulse was scanned across a protein absorption spectrum and the intensity change of the protein carbonyl stretch band (amide I band) showed up as cross peaks in a 2D representation, indicating coupled vibrational modes. Then femtosecond-pulse 2D IR spectroscopy was implemented with better time resolution using heterodyne detection of photon echoes [13]. Fourier transform spectral interferometry [68, 88, 89, 90], based on heterodyne detection, is utilized in most 2D FTS experiments to obtain full information including amplitude and phase of the non-linear signal. Time-domain heterodyne techniques for full signal characterization have

been discussed [91, 92, 93], however they are less widely used since both time dimensions have to be scanned.

The power of 2D FTS has not been extended to the studies of carrier dynamics and many-body effects in semiconductors until recently, although there were some attempts of two-dimensional spectroscopic approaches in primitive forms. To distinguish whether the beats from disordered quantum wells with a bimodal inhomogeneous distribution were quantum beats or electromagnetic interference, a technique based on time resolving the FWM was applied, in which the time-resolved signal was displayed as a function of the delay between excitation pulses to construct a two-dimensional plot [7, 94, 95]. A similar method based on spectrally resolving the FWM signal was also developed [49]. Based on a model that the temporal positions of beat peaks for quantum beats and electromagnetic interference have different dependence on the pulse delay, a conclusion was reached that the beats were truly quantum beats, meaning the spatially separated exciton transitions were coupled [96]. This result was interpreted by a calculation that includes both disorder and many-body effects [97]. Another form of non-Fourier transform two-dimensional technique is coherent excitation spectroscopy (CES) [98], an extension to partially-degenerate FWM [51, 99]. The FWM signal is generated with a first pulse of narrow bandwidth and a second pulse of broad bandwidth and spectrally resolved at different frequencies of the first pulse in two dimensions. CES suggested that spatially localized excitons in disordered quantum wells are not coupled to each other, in contradiction to the earlier conclusion. Two-dimensional luminescence excitation spectra were developed for single dot spectroscopy, which displayed coupling between resonances due to incoherent energy migration in naturally occurring quantum dots in thin quantum wells [100, 101, 102, 103, 104]. As in the context of multidimensional NMR, "two-dimensional Fourier transform spectroscopy" specifically means that coherent phase evolution is preserved in both dimensions so a 2D Fourier transformation is feasible. The spectroscopic techniques mentioned in this paragraph simply display a

stack of data in two dimensions, therefore they are not considered as 2D FTS.

Although optical 2D FTS shares many similarities with 2D NMR in concepts, there are fundamental differences between them [85]. First, the ultrafast pulses used in optical 2D FTS contain far fewer cycles as compared to the radio-frequency pulses in NMR, meaning molecules are frozen in place in the femtosecond pulse duration rather than motionally averaged in NMR. Therefore ultrafast 2D FTS provides multidimensional snapshots of the fast chemical dynamics on extremely short timescale. In addition, the wavelength of optical pulses is significantly smaller than the sample dimensions (the size of coherent area in a sample is typically $\sim 100\lambda$ for near-IR excitations). In this case, the nonlinear electric field is emitted in specific phase-matched directions if the excitation pulses have a non-collinear geometry (see Section 3.2). Time-gating is commonly used in collinearly excited NMR to separate the signal from strong excitation pulses. In femtosecond experiments, however, the signal is often emitted temporally together with excitation pulses, thus it cannot be separated by time-gating. If non-collinear excitation geometry is used, the signal can be detected background-free in phase-matched directions with no need for time-gating.

Furthermore, non-collinear excitation enables the spatial isolation of coherent pathways. For a particular phase-matched direction, only the corresponding parts of the nonlinear response are in resonance with excitation, thus the contributions of coherent pathways can be isolated in different directions. In NMR, phase cycling is used to obtain the signal from desired coherent pathways. The phase of excitation pulses needs to be systematically varied to generate a nonlinear signal corresponding to a specific coherence pathway from a collection of measured signals [8]. A 2D absorption spectrum can be obtained by superposing equally weighted signals excited by two pulse sequences with oppositely signed coherence orders during the evolution period. An optical 2D experiment with a collinear geometry, in which signals from all coherence pathways are emitted in the same direction, was performed as analog of the simplest 2D NMR to ex-

amine the possible extension of 2D NMR into the optical regime [20]. In non-collinear optical 2D FTS experiments, a specific phase-matched direction and temporal ordering of excitation pulses can be selected to isolate the coherent pathways of interest. The isolation of coherent pathways in 2D FTS is to be discussed in Section 3.5. A combination of non-collinear pulse geometry for coherence pathway selection with the phase control ability in current pulse-shaping technologies would allow optical 2D spectroscopy to highlight more specific properties of the sample being excited.

3.2 Nonlinear response function

Microscopic information about electronic couplings and dynamics in a system is represented by the multidimensional nonlinear response function, when a sequence of n excitation pulses is applied to the system to generate and maintain coherences and populations of the electronic states [81]. In a three-pulse experiment, excitation pulses arrive at times τ_1, τ_2, and τ_3 respectively, separated by a time delay of $t_1 = \tau_2 - \tau_1$ between the first two pulses, and delay $t_2 = \tau_3 - \tau_2$ between the second and third pulses, as shown in Fig. 3.1. The nonlinear third-order signal generated by the interaction with all three pulses is measured at time t, after a delay t_3 from the last excitation pulse.[1]

The electric field of each pulse in a three-pulse sequence has the form:

$$\mathbf{E}_j(\mathbf{r}, t) = [\, \varepsilon_j^+(t) e^{i(\mathbf{k}_j \cdot \mathbf{r} - \omega_j t)} + \varepsilon_j^-(t) e^{-i(\mathbf{k}_j \cdot \mathbf{r} - \omega_j t)} \,] \hat{\mathbf{e}}_j \; , \tag{3.1}$$

for the j-th pulse (j=1, 2, or 3) with wavevector $\mathbf{k}_j$, carrier frequency ω_j, and unit polarization vector $\hat{\mathbf{e}}_j$. $\varepsilon_j^+(t)$ ($\varepsilon_j^- = (\varepsilon_j^+)^*$) is the positive (negative) frequency component of the slow-varying pulse envelope. The pulse sequence can be expressed as the sum of three electric fields:

$$\mathbf{E}(\mathbf{r}, t) = \sum_{j=1}^{3} \mathbf{E}_j(\mathbf{r}, t - \tau_j) \; . \tag{3.2}$$

---

[1] For convenience, interpulse time delays are denoted as t_1, t_2, and t_3 in Section 3.2 and 3.3, rather than τ, T, and t elsewhere in this thesis.
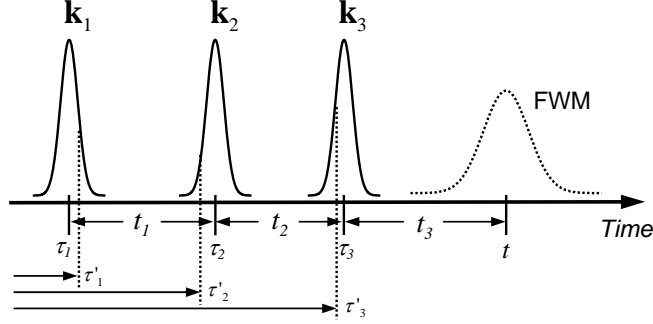
Figure 3.1: Excitation pulse sequence in a three-pulse nonlinear experiment. Pulses arrive at times τ_1, τ_2, and τ_3 respectively, separated by a time delay of $t_1 = \tau_2 - \tau_1$ between the first two pulses, and delay $t_2 = \tau_3 - \tau_2$ between the second and third pulses. Nonlinear third-order signal is measured at time t, after a delay t_3 from the last excitation pulse.

The polarization induced by three excitation pulses occurs at third-order in the applied fields [82]:

$$P^{(3)}(\mathbf{r}, \tau_1, \tau_2, \tau_3) = \int_0^\infty \int_0^\infty \int_0^\infty \mathcal{R}^{(3)}(\tau_1', \tau_2', \tau_3') E_1(\mathbf{r}, \tau_1' - \tau_1) E_2(\mathbf{r}, \tau_2' - \tau_2)$$

$$\times E_3(\mathbf{r}, \tau_3' - \tau_3) \, d\tau_1' \, d\tau_2' \, d\tau_3' , \qquad (3.3)$$

where $\mathcal{R}^{(3)}$ is the third-order time-dependent response function of the system, and τ_i' ($i = 1, 2, \text{or } 3$) is the integration variable associated with pulse i. The n-th order response function $\mathcal{R}^{(n)}$ can be expressed as a combination of $n + 1$ order correlation functions of the dipole moment operator [82]:

$$\mathcal{R}^{(1)}(t_1) = \frac{i}{\hbar} \langle [\, \mu(t_1), \mu(0)\,] \rangle , \qquad (3.4)$$

$$\mathcal{R}^{(2)}(t_1, t_2) = (\frac{i}{\hbar})^2 \langle [\, \mu(t_1 + t_2), [\, \mu(t_1), \mu(0)\,]\,] \rangle , \qquad (3.5)$$

$$\mathcal{R}^{(3)}(t_1, t_2, t_3) = (\frac{i}{\hbar})^3 \langle [\, \mu(t_1 + t_2 + t_3), [\, \mu(t_1 + t_2), [\, \mu(t_1), \mu(0)\,]\,]\,] \rangle , \qquad (3.6)$$

and so forth. The time evolution of the dipole moment operator $\mu(t)$ is given by the system Hamiltonian in the absence of applied fields. In general, a sum-over-states expression of $\mathcal{R}^{(n)}$ can be derived for an arbitrary multilevel system [81].

In the limit of impulsive excitation, where the pulse envelope is much shorter than both the dynamic time scale and the delays between pulses, the time integrations in Eqn. (3.3) can be evaluated by approximating the pulses as delta functions. After each electric field is plugged in, the third-order polarization has the following form [33]:

$$P^{(3)}(\mathbf{r}, t, t_1, t_2, t_3) = \mathcal{R}^{(3)}(t_1, t_2, t_3)\ \varepsilon_1^\pm \varepsilon_2^\pm \varepsilon_3^\pm e^{i(\pm\mathbf{k}_1\pm\mathbf{k}_2\pm\mathbf{k}_3)\cdot\mathbf{r}} e^{-i(\pm\omega_1\pm\omega_2\pm\omega_3)t}$$

$$\times\ e^{i(\pm\omega_1\pm\omega_2\pm\omega_3)t_3} e^{i(\pm\omega_1\pm\omega_2)t_2} e^{\pm i\omega_1 t_1}\ , \qquad (3.7)$$

where t_1, t_2, and t_3 are pulse time delays. There are several possible contributions to the polarization associated with different wavevectors $\mathbf{k}_s = \pm\mathbf{k}_1\pm\mathbf{k}_2\pm\mathbf{k}_3$. Each contribution produces a distinct signal field in the corresponding $\mathbf{k}_s$ direction after the polarization is plugged into the Maxwell's equations, provided the sample size is larger than the signal wavelength. This requirement is usually satisfied in optical experiments, thus the emission of optical fields produced by the polarization has directionality. Phase-matching conditions together with the frequency dependence of the refraction index of the system may favor some of these directions and suppress others. For a particular direction of signal wavevector or combination of wavevectors, only the corresponding parts of the nonlinear response function are in resonance with the fields and contribute significantly to the polarization, resulting in a resonant signal dominated by these contributions.

Among the eight possible signal wavevectors in a three-pulse excitation, only four of them are independent as $\mathbf{k}_s$ and $-\mathbf{k}_s$ correspond to complex conjugated contributions. The possible wavevector of the polarization is one of the following: $\mathbf{k}_\mathrm{I} = -\mathbf{k}_1 + \mathbf{k}_2 + \mathbf{k}_3$, $\mathbf{k}_\mathrm{II} = \mathbf{k}_1 - \mathbf{k}_2 + \mathbf{k}_3$, $\mathbf{k}_\mathrm{III} = \mathbf{k}_1 + \mathbf{k}_2 - \mathbf{k}_3$, and $\mathbf{k}_\mathrm{IV} = \mathbf{k}_1 + \mathbf{k}_2 + \mathbf{k}_3$, labeled with subscript I, II, III, or IV. Each wavevector also corresponds to an emission frequency $\omega_\mathrm{I} = -\omega_1 + \omega_2 + \omega_3$, $\omega_\mathrm{II} = \omega_1 - \omega_2 + \omega_3$, $\omega_\mathrm{III} = \omega_1 + \omega_2 - \omega_3$, and $\omega_\mathrm{IV} = \omega_1 + \omega_2 + \omega_3$, respectively. Consequently, Eqn. (3.7) can be recast to show the polarization as a sum

of the four contributions with wavevectors $\mathbf{k}_I$, $\mathbf{k}_{II}$, $\mathbf{k}_{III}$, and $\mathbf{k}_{IV}$:

$$P^{(3)}(\mathbf{r},t,t_1,t_2,t_3) = \sum_{s=I}^{IV} \mathcal{P}_s(t_1,t_2,t_3)e^{i(\mathbf{k}_s \cdot \mathbf{r} - \omega_s t)} + c.c. \ , \tag{3.8}$$

where the polarization term $\mathcal{P}_s(t_1,t_2,t_3)$ has the following expression for s=I, II, III, or IV:

$$\mathcal{P}_I(t_1,t_2,t_3) = \mathcal{R}_I^{(3)}(t_1,t_2,t_3)\,\varepsilon_1^- \varepsilon_2^+ \varepsilon_3^+ e^{i(-\omega_1+\omega_2+\omega_3)t_3} e^{i(-\omega_1+\omega_2)t_2} e^{-i\omega_1 t_1} \ , \tag{3.9}$$

$$\mathcal{P}_{II}(t_1,t_2,t_3) = \mathcal{R}_{II}^{(3)}(t_1,t_2,t_3)\,\varepsilon_1^+ \varepsilon_2^- \varepsilon_3^+ e^{i(\omega_1-\omega_2+\omega_3)t_3} e^{i(\omega_1-\omega_2)t_2} e^{i\omega_1 t_1} \ , \tag{3.10}$$

$$\mathcal{P}_{III}(t_1,t_2,t_3) = \mathcal{R}_{III}^{(3)}(t_1,t_2,t_3)\,\varepsilon_1^+ \varepsilon_2^+ \varepsilon_3^- e^{i(\omega_1+\omega_2-\omega_3)t_3} e^{i(\omega_1+\omega_2)t_2} e^{i\omega_1 t_1} \ , \tag{3.11}$$

$$\mathcal{P}_{IV}(t_1,t_2,t_3) = \mathcal{R}_{IV}^{(3)}(t_1,t_2,t_3)\,\varepsilon_1^+ \varepsilon_2^+ \varepsilon_3^+ e^{i(\omega_1+\omega_2+\omega_3)t_3} e^{i(\omega_1+\omega_2)t_2} e^{i\omega_1 t_1} \ . \tag{3.12}$$

The last term, $\mathcal{P}_{IV}$, corresponds to a highly oscillatory polarization at approximately the third harmonic of the incident field, thus it is neglected within the rotating-wave approximation (RWA) [33]. The third-order polarization associated with each direction can be obtained in the form of a sum-over-states expression with the help of double-sided Feynman diagrams.

3.3   Double-sided Feynman diagrams

In perturbation theory, the evolution of density matrix elements can be conveniently tracked by double-sided Feynman diagrams. With the capability of carrying the complete information including the time ordering and the choice of frequencies and their signs, the double-sided Feynman diagram is a tool for diagrammatically describing nonlinear interactions of light with matter. Each diagram corresponds to a coherent pathway in the Liouville space.

There are some basic rules for double-sided Feynman diagrams [81]. The density matrix operator is represented by two vertical lines, where the left line stands for the ket and the right line for the bra, with time increasing vertically upward. Each incident light

field is represented by a wiggly line with an arrow and the interaction of a field with the system is indicated by a vertex of the wiggly line and the left or right vertical line. The density matrix state is changed by the interaction and a label below (above) the vertex gives the state before (after) the interaction. A wiggly line pointing to the right means a contribution of $E_j \exp(i\mathbf{k}_j \cdot \mathbf{r} - i\omega_j t)$ to the polarization, while a line pointing to the left means the conjugate contribution of $E_j^* \exp(-i\mathbf{k}_j \cdot \mathbf{r} + i\omega_j t)$. A wiggly line coming towards the vertical lines means absorption, thus taking the system to or from a coherent superposition. Conversely, a line going away represents photon emission, sending the system from higher energy back to lower energy state. The overall wavevector of a diagram is the sum of those of the individual fields with appropriate signs. The sign of a diagram is $(-1)^n$ where n is the number of vertexes on the right vertical line (bra), since each interaction acting from the right in a commutator introduces a minus sign. Each order in the perturbation of interaction is described by a basic diagram containing one vertex on the left or the right vertical line, and n such diagrams are concatenated vertically in time order to produce a diagram for the n-th order perturbation theory. The n-th order perturbation usually consists of many double-sided Feynman diagrams with different wavevectors, frequencies and time ordering of the incident fields. From the double-sided diagrams one can directly write down the mathematical form of the nonlinear response function with a few rules.

To illustrate how double-sided Feynman diagrams track the density matrix elements, we discuss a system containing a ground state $|g\rangle$, singly-excited states $|e\rangle$ and $|e'\rangle$, and doubly-excited states $|f\rangle$, just as a simplified model for the semiconductor quantum well system with excited HH excitons, LH excitons and biexcitons in Chapter 2. As shown in Fig. 3.2, the double-sided Feynman diagrams representing the third-order perturbation in a three-pulse excitation of such a level scheme (depicted in Fig. 3.2(d)) can be grouped by the phase-matched directions [82]. The diagrams for direction $\mathbf{k}_\mathrm{I}$, $\mathbf{k}_\mathrm{II}$, and $\mathbf{k}_\mathrm{III}$ are listed in box (a), (b), and (c), respectively. The diagrams for the direction
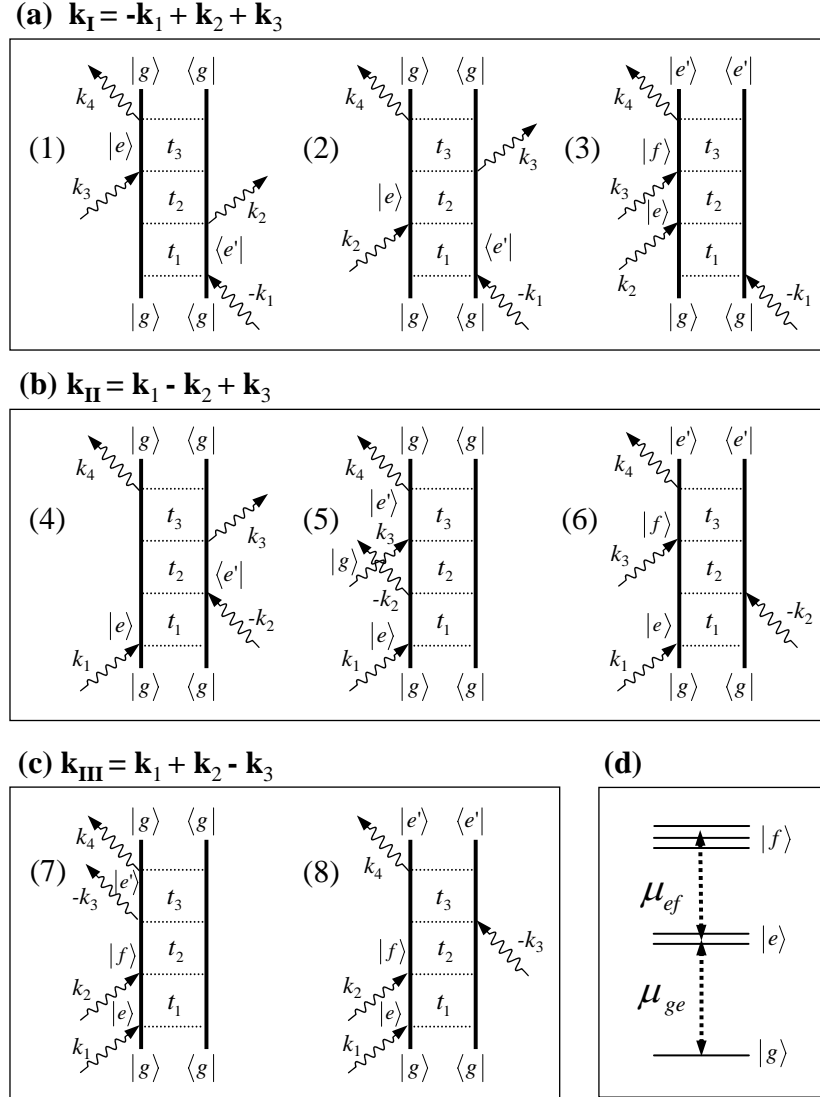
Figure 3.2: Double-sided Feynman diagrams representing contributions to the phase-matched directions $\mathbf{k}_I = -\mathbf{k}_1+\mathbf{k}_2+\mathbf{k}_3$ (a), $\mathbf{k}_{II} = \mathbf{k}_1-\mathbf{k}_2+\mathbf{k}_3$ (b), and $\mathbf{k}_{III} = \mathbf{k}_1+\mathbf{k}_2-\mathbf{k}_3$ (c) for a system containing a ground state, excited states $|e\rangle$, and doubly-excited states $|f\rangle$ (d).

$\mathbf{k}_{IV}$ are not presented since the third-order polarization corresponding to $\mathbf{k}_{IV}$ vanishes within RWA.

For phase-matched direction $\mathbf{k}_I$, the three double-sided Feynman diagrams contributing to the polarization are listed in box (a) of Fig. 3.2. Labeled as (1), (2), and

(3), these diagrams describe the respective process of ground-state bleaching (GSB), excited-state emission (ESE), and excited-state absorption (ESA) [82]. In diagram (1), for example, the conjugated field $\mathbf{k}_1$ comes first and excites the system to state $|e'\rangle$. The wiggly line of $\mathbf{k}_1$ is pointing up to the vertical line from the right hand side since it makes a conjugate contribution of $E_1^* \exp(-i\mathbf{k}_1 \cdot \mathbf{r} + i\omega_1 t)$ to the polarization. After a delay t_1, the second field $\mathbf{k}_2$ brings the system back to state $|g\rangle$, as the $\mathbf{k}_2$ line is going away from the vertical line. The third field $\mathbf{k}_3$ arrives with a delay t_2 after the second field and excites the system again to state $|e\rangle$. In the end, the system returns to ground state by emitting a signal along $\mathbf{k}_\mathrm{I}$ at delay t_3 after the third pulse. Similarly, diagram (2) and (3) describe other possible transitions with the same pulse time ordering for the emission in direction $\mathbf{k}_\mathrm{I}$. For emission along direction $\mathbf{k}_\mathrm{II}$, there are also three contributions represented by diagram (4), (5), and (6) in box (b) of Fig. 3.2, where pulse $\mathbf{k}_2$ has the conjugated field. Furthermore, two diagrams (7) and (8) in box (c) are the contributions to the emission in direction $\mathbf{k}_\mathrm{III}$. Note that in the case of $\mathbf{k}_\mathrm{I}$ or $\mathbf{k}_\mathrm{II}$, there is only one diagram involving doubly-excited stated $|f\rangle$, while in the case of $\mathbf{k}_\mathrm{III}$, both diagrams include $|f\rangle$.

Once all the possible Feynman diagrams for a particular phase-matched direction are presented, it is straightforward to obtain the sum-over-states expression of the non-linear response function from all the diagrams with an appropriate set of translation rules. The third-order response function $\mathcal{R}_I^{(3)}$, $\mathcal{R}_\mathrm{II}^{(3)}$, and $\mathcal{R}_\mathrm{III}^{(3)}$ can be written as a sum of all contributions presented in Fig. 3.2(a), (b), and (c), respectively [33]:

$$\mathcal{R}_{\mathrm{I}}^{(3)}(t_1, t_2, t_3) = (\frac{i}{\hbar})^3[$$

$$\sum_{e,e'}(\boldsymbol{\mu}_{ge'} \cdot \hat{\mathbf{e}}_1)(\boldsymbol{\mu}_{e'g} \cdot \hat{\mathbf{e}}_2)(\boldsymbol{\mu}_{eg} \cdot \hat{\mathbf{e}}_3)(\boldsymbol{\mu}_{ge} \cdot \hat{\mathbf{e}}_4)e^{(i\omega_{e'g}-\Gamma_{e'g})t_1}e^{-\Gamma_{gg}t_2}e^{-(i\omega_{eg}+\Gamma_{eg})t_3}$$

$$+\sum_{e,e'}(\boldsymbol{\mu}_{ge'} \cdot \hat{\mathbf{e}}_1)(\boldsymbol{\mu}_{eg} \cdot \hat{\mathbf{e}}_2)(\boldsymbol{\mu}_{e'g} \cdot \hat{\mathbf{e}}_3)(\boldsymbol{\mu}_{ge} \cdot \hat{\mathbf{e}}_4)e^{(i\omega_{e'g}-\Gamma_{e'g})t_1}e^{-(i\omega_{ee'}+\Gamma_{ee'})t_2}e^{-(i\omega_{eg}+\Gamma_{eg})t_3}$$

$$-\sum_{e,e',f}(\boldsymbol{\mu}_{ge'} \cdot \hat{\mathbf{e}}_1)(\boldsymbol{\mu}_{eg} \cdot \hat{\mathbf{e}}_2)(\boldsymbol{\mu}_{ef} \cdot \hat{\mathbf{e}}_3)(\boldsymbol{\mu}_{e'f} \cdot \hat{\mathbf{e}}_4)e^{(i\omega_{e'g}-\Gamma_{e'g})t_1}e^{-(i\omega_{ee'}+\Gamma_{ee'})t_2}e^{-(i\omega_{fe'}+\Gamma_{fe'})t_3} \ ] \ ,$$

$$(3.13)$$

$$\mathcal{R}_{\mathrm{II}}^{(3)}(t_1, t_2, t_3) = (\frac{i}{\hbar})^3[$$

$$\sum_{e,e'}(\boldsymbol{\mu}_{eg} \cdot \hat{\mathbf{e}}_1)(\boldsymbol{\mu}_{ge} \cdot \hat{\mathbf{e}}_2)(\boldsymbol{\mu}_{e'g} \cdot \hat{\mathbf{e}}_3)(\boldsymbol{\mu}_{ge'} \cdot \hat{\mathbf{e}}_4)e^{-(i\omega_{eg}+\Gamma_{eg})t_1}e^{-\Gamma_{gg}t_2}e^{-(i\omega_{e'g}+\Gamma_{e'g})t_3}$$

$$+\sum_{e,e'}(\boldsymbol{\mu}_{eg} \cdot \hat{\mathbf{e}}_1)(\boldsymbol{\mu}_{ge'} \cdot \hat{\mathbf{e}}_2)(\boldsymbol{\mu}_{e'g} \cdot \hat{\mathbf{e}}_3)(\boldsymbol{\mu}_{ge} \cdot \hat{\mathbf{e}}_4)e^{-(i\omega_{eg}+\Gamma_{eg})t_1}e^{-(i\omega_{ee'}+\Gamma_{ee'})t_2}e^{-(i\omega_{eg}+\Gamma_{eg})t_3}$$

$$-\sum_{e,e',f}(\boldsymbol{\mu}_{eg} \cdot \hat{\mathbf{e}}_1)(\boldsymbol{\mu}_{ge'} \cdot \hat{\mathbf{e}}_2)(\boldsymbol{\mu}_{fe} \cdot \hat{\mathbf{e}}_3)(\boldsymbol{\mu}_{e'f} \cdot \hat{\mathbf{e}}_4)e^{-(i\omega_{eg}+\Gamma_{eg})t_1}e^{-(i\omega_{ee'}+\Gamma_{ee'})t_2}e^{-(i\omega_{fe'}+\Gamma_{fe'})t_3} \ ] \ ,$$

$$(3.14)$$

$$\mathcal{R}_{\mathrm{III}}^{(3)}(t_1, t_2, t_3) = (\frac{i}{\hbar})^3[$$

$$\sum_{e,e',f}(\boldsymbol{\mu}_{eg} \cdot \hat{\mathbf{e}}_1)(\boldsymbol{\mu}_{fe} \cdot \hat{\mathbf{e}}_2)(\boldsymbol{\mu}_{e'f} \cdot \hat{\mathbf{e}}_3)(\boldsymbol{\mu}_{ge'} \cdot \hat{\mathbf{e}}_4)e^{-(i\omega_{eg}+\Gamma_{eg})t_1}e^{-(i\omega_{fg}+\Gamma_{fg})t_2}e^{-(i\omega_{e'g}+\Gamma_{e'g})t_3}$$

$$-\sum_{e,e',f}(\boldsymbol{\mu}_{eg} \cdot \hat{\mathbf{e}}_1)(\boldsymbol{\mu}_{fe} \cdot \hat{\mathbf{e}}_2)(\boldsymbol{\mu}_{ge'} \cdot \hat{\mathbf{e}}_3)(\boldsymbol{\mu}_{e'f} \cdot \hat{\mathbf{e}}_4)e^{-(i\omega_{eg}+\Gamma_{eg})t_1}e^{-(i\omega_{fg}+\Gamma_{fg})t_2}e^{-(i\omega_{fe'}+\Gamma_{fe'})t_3} \ ] \ ,$$

$$(3.15)$$

where $\boldsymbol{\mu}_{ij}$, ω_{ij}, and Γ_{ij} are the dipole moment, transition frequency and dephasing rate of the $i \rightarrow j$ $(i, j = g, e, e', \mathrm{or}\ f)$ transition respectively. In Eqns. (3.13), (3.13), and (3.15), each line on the right-hand side of the equation corresponds to a double-sided Feynman diagram in Fig. 3.2(a), (b), and (c) respectively.

3.4 Two-dimensional Fourier transform spectroscopy

The 2D FTS technique is based on a highly enhanced version of degenerate FWM experiments, in which the coherent phase evolution of the emitted signal is tracked with the delay of excitation pulses in sub-optical-cycle precision and the signal phase is obtained with heterodyne detection. The challenges of implementing 2D FTS are discussed in detail in the next chapter. A typical box geometry used in 2D FTS experiments is shown in Fig. 3.3(a), where pulses are labeled by their geometric positions rather than time ordering. Three excitation beams of same frequency propagate with wavevector $\mathbf{k}_a$, $\mathbf{k}_b$, and $\mathbf{k}_c$ arranged on three corners of a square before they are focused on a sample. The FWM electric field induced by the third-order polarization is emitted in the phase-matched direction $\mathbf{k}_s = -\mathbf{k}_a + \mathbf{k}_b + \mathbf{k}_c$. Fig. 3.3(c) shows the FWM and excitation beam spots on the output lens viewed from the sample side. In this square box geometry configuration, the length of the polarization wavevector matches that of the
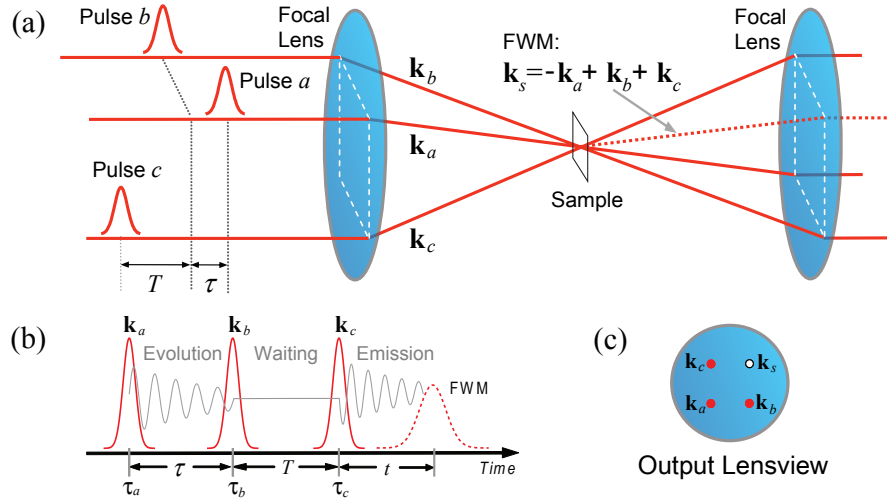
Figure 3.3: (a) The box geometry of excitation beams $\mathbf{k}_a$, $\mathbf{k}_b$, and $\mathbf{k}_c$. FWM is emitted in the phase-matched direction $\mathbf{k}_s = -\mathbf{k}_a + \mathbf{k}_b + \mathbf{k}_c$; (b) Time ordering of excitation pulses, where the evolution time, waiting time, and emission time are labeled as τ, T, and t, respectively; (c) FWM and excitation beam spots on the output lens, viewed from the sample side.

incident fields, thus phase mismatch in the sample is minimized [76]. The time ordering of pulses is depicted in Fig. 3.3(b), where the delay t_1 between the first and second pulses is the evolution time τ, and the delay t_2 between the second and third pulse is the waiting time T (or waiting time in NMR). The delay between signal and the third pulse corresponds to the signal emission time t, provided the origin of time is set to the center of the third pulse.

The FWM signal is measured with frequency-domain heterodyne detection to obtain both spectral amplitude and phase. The electric field of the emitted signal is determined by the third-order polarization (in Gaussian units) [76]:

$$E(\tau, T, \omega_t) = \frac{2\pi \, l}{n(\omega_t) \, c} \, i \, \omega_t \, P^{(3)}(\tau, T, \omega_t) \; , \tag{3.16}$$

which is a function of the evolution time τ, waiting time T, and emission frequency ω_t. Here l is the sample thickness, $n(\omega_t)$ is the refraction index of the sample, and c is the speed of light in vacuum. Eqn. (3.16) is valid only when absorption and propagation effects in the sample can be neglected. The pulse propagation effects in thick samples can be treated with a suitable multidimensional frequency filter function [85].

In the standard technique of 2D FTS, the electric field of the emitted FWM signal is presented in two frequency dimensions after Fourier transforms with respect to two time variables: the evolution time τ and emission time t. Since the transform with respect to t is implicit in frequency-domain heterodyne detection, a Fourier transform with respect to τ produces the 2D spectrum:

$$\mathcal{S}(\omega_\tau, T, \omega_t) = \int_{-\infty}^{+\infty} E(\tau, T, \omega_t) \, e^{i\omega_\tau \tau} \, d\tau \; , \tag{3.17}$$

at a fixed value of T. The new dimension ω_τ is called the absorption frequency as it corresponds to the absorption process in excitation. The optical 2D FTS defined in this manner is closest to the Correlated Spectroscopy (COSY) and Nuclear Overhauser Effects Spectroscopy (NOESY) among many variations of multidimensional NMR spectroscopy [8]. In both COSY and NOESY, the "direct" frequency is produced in the

measurement of the emitted field and the "indirect" frequency is obtained from the Fourier transform with respect to the scanning delay between the first two pulses. In NOESY, the waiting time T between the second and third pulses is nonzero, allowing population dynamics to occur. In contrast, there is no delay between the last two pulses (or a single pulse functions as two pulses) in COSY. Despite its frequency-domain appearance, 2D FTS is still considered as a time domain technique, as it relies completely on the temporal control of the excitation pulse sequence [82].

A 2D Fourier transform spectrum $\mathcal{S}_\mathrm{I}(\omega_\tau, T, \omega_t)$ correlates the absorption frequency ω_τ and the emission frequency ω_t in a two-dimensional map by monitoring the coherent phase evolution of the third-order polarization during the evolution period τ and emission period t, separated by a waiting time T. By extending the FWM signal traditionally measured in one-dimension to two dimensions with independent frequency variables, congested spectra are disentangled and couplings between resonances are identified. In addition, contributions from various quantum mechanical coherent pathways can be isolated and associated with peaks in 2D spectra. The power of 2D FTS comes from the fact that the phase evolution of the third-order polarization is coherently tracked and correlated in the evolution and emission time periods, rather than from the use of Fourier transformation, which just facilitates the presentation of data in frequency domain. In some early experiments on semiconductors, the complete FWM electric field including phase was measured to obtain phase dynamics of the emitted signal [92, 105]. However, the crucial aspect of tracking signal phase as a function of excitation pulse delay was not included. A closer analogy to 2D FTS is the coherent excitation spectroscopy (CES), which was developed and applied to the study of coupling between disorder localized excitons [98].

To understand why coherent tracking of the signal phase is critical, we consider the FWM signal that is emitted from a transition with frequency ω_{ik} due to excitation of a transition with frequency ω_{ij} by the first pulse. If the first pulse is the conjugated

field, as in the case of $\mathbf{k}_\mathrm{I}$ experiments, the electric field of the signal can be written as [56]:

$$S(\tau,t) = D(\tau,T,t)\,\mu_{ij}^2\,\mu_{ik}^2\,e^{i(\omega_{ij}\tau-\omega_{ik}t)}\;,\tag{3.18}$$

where μ_{ij} and μ_{ik} are the dipole moments of the respective excitation and emission transitions. All the decay dynamics and any process between the second and third pulses are lumped into the term $D(\tau,T,t)$. Eqn. (3.18) shows that phase evolution between the first two pulses results in a constant overall phase in the emitted field. Thus, by coherently tracking the phase of the signal as the delay between the excitation pulses is varied with sub-cycle precision, one can determine the frequency of the excitation transition simultaneously with that of the emission transition. The correlation between these two frequencies can be conveniently displayed in a 2D map with a two-dimensional Fourier transform that converts the time domain data into frequency domain. Coherently tracking signal phase with the time delay between excitation pulses and maintaining sub-cycle precision of the delay is experimentally challenging. We achieved interferometric accuracy in delay scanning and stabilization in our 2D FTS experimental apparatus, which will be discussed in detail in the next chapter.

The coherent phase evolution is directly related to the time ordering of excita-

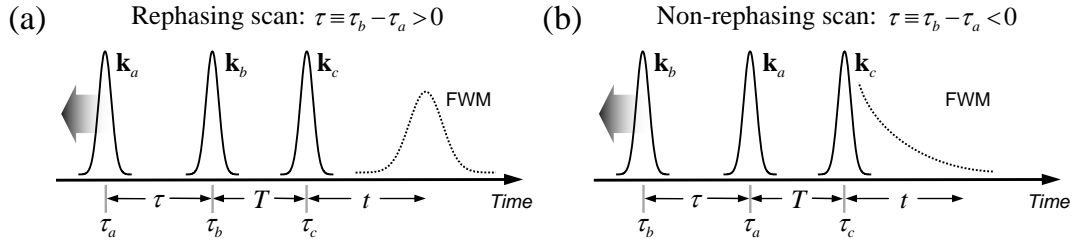Figure 3.4: (a) Excitation pulse sequence for a rephasing experiment, in which the conjugated pulse a is scanned to earlier times while pulse b and c are fixed and separated by waiting time T. τ is positive by definition; (b) Pulse sequence for a non-rephasing experiment, in which pulse b is scanned to earlier times while pulse a and c are fixed and separated by waiting time T. τ is negative.

tion pulses. The phase evolution described by Eqn. (3.18) is actually produced by a "rephasing" pulse sequence in the $\mathbf{k}_I$ pulse geometry. As shown in Fig. 3.4(a), the conjugated pulse a arrives first and creates a coherent superposition between the ground and excited state in the ensemble. Then the oscillators in the ensemble dephase with different resonant frequencies in the evolution time period τ, provided the system is inhomogeneously broadened. The third pulse introduces a conjugated phase evolution in the emission time period t and causes the oscillators to reverse their phases, resulting in a photon echo signal with a delay τ from the third pulse [106].[2] Therefore we refer to this time ordering as a "rephasing" excitation sequence. One advantage of the three-pulse excitation is that the time ordering of the first two pulses can be interchanged. If the pulse b comes earlier than the conjugated pulse a in the case of "non-rephasing" pulse sequence shown in Fig. 3.4(b), the phase evolution in the evolution and emission periods has the form of $S(\tau, t) = D(\tau, T, t)\, \mu_{ij}^2\, \mu_{ik}^2\, e^{-i(\omega_{ij}\tau + \omega_{ik}t)}$. There is no conjugation in phase evolution and thus a free polarization decay, instead of photon echo signal, is produced in a system with inhomogeneous broadening. Delay τ is defined as the difference between the arriving times of pulse b and pulse a: $\tau = t_b - t_a$, so τ is positive for the rephasing pathway and negative for the non-rephasing pathway. As depicted in Fig. 3.4, the conjugated pulse a is scanned in a rephasing experiment whereas pulse b and c are fixed in time and separated by a waiting time T. The emitted FWM is measured while pulse a is being scanned away from t_b, the time-overlapping position with pulses b, to earlier times t_a for a series of data with increasing τ. In a non-rephasing experiment, however, the conjugated pulse a and pulse c are stationary as pulse b is scanned with negatively increasing τ from t_a to earlier times t_b [24].

The sign of the absorption frequency ω_τ is different for the rephasing and non-rephasing pathways. The emission frequency ω_t is usually chosen to be positive, then ω_τ

---

[2] An enlightening illustration of spin echo can be found on the front cover of the November 1953 edition of *Physics Today*.

is negative in a rephasing experiment as a result of the conjugated phase evolutions in the evolution and emission time periods. The 2D spectra of the rephasing pathway appear in the lower-right quadrant of the (ω_τ, ω_t) plane, i.e., $\omega_t > 0$ and $\omega_\tau < 0$. In a non-rephasing experiment, ω_τ and ω_t have the same sign and the 2D spectra show up in the upper-right quadrant. Comparison of spectra in rephasing and non-rephasing pathways gives insight into the presence of inhomogeneity and allows isolation of different contributions in the Liouville space [55, 73].

As discussed earlier in Section 3.1 of this chapter, one advantage of optical 2D FTS over 2D NMR is that non-collinear excitation geometry can be used in optical 2D experiments to allow the selection of coherent pathways from different phase-matched directions. Most 2D FTS experiments are performed in the photon echo geometry where the FWM signal is emitted in direction $\mathbf{k}_{\mathrm{I}}$, as shown in Fig. 3.3. The measured 2D spectrum is correspondingly denoted as $\mathcal{S}_{\mathrm{I}}(\omega_\tau, T, \omega_t)$. Other spatial arrangements can also be utilized to implement 2D spectroscopies that probe different coherent pathways for additional information. For example, the $\mathcal{S}_{\mathrm{III}}$ 2D spectra produced from FWM signal emitted in the $\mathbf{k}_{\mathrm{III}}$ direction are intrinsically sensitive to two-exciton correlations [107]. Two-exciton contributions are demonstrated in both frequency dimensions of the $\mathcal{S}_{\mathrm{III}}$ spectra, while they manifest themselves only along one frequency axis in other third-order nonlinear spectroscopies. Consequently, high two-exciton resolution unavailable in conventional 1D FWM and other 2D FTS experiments is achieved and the two-exciton binding energy can be revealed even when it is smaller than the line broadening.

3.5   Advantages of 2D FTS

Being a new spectroscopic method that tracks coherent phase evolution and displays correlation in two frequency dimensions, 2D FTS presents many advantageous features, such as identifying coupling of resonances with the appearance of cross peaks

and isolating quantum mechanical coherent pathways in Liouville space. These features are discussed in the following subsections.

3.5.1 Identification of resonant coupling

In 2D spectra, resonances result in diagonal peaks and the coupling of resonances is indicated by the appearance of off-diagonal peaks, allowing an intuitive way for the identification of couplings. For a system with two independent transitions of frequency ω_1 and ω_2 (two two-level systems) depicted in Fig. 3.5(a), there are two diagonal peaks at $(\omega_1, -\omega_1)$ and $(\omega_2, -\omega_2)$ in the corresponding 2D spectrum. A peak in the 2D spectrum is specified by the coordinates of emission frequency ω_t and absorption frequency ω_τ in the form of (ω_t, ω_τ). The rephasing pathway is shown here, therefore ω_τ is negative and ω_t is positive. If the two transitions share the same ground state, as the "V" system shown in Fig. 3.5(b), they are not independent any more. The coupling between the two transitions is revealed directly in the 2D spectrum: two additional off-diagonal
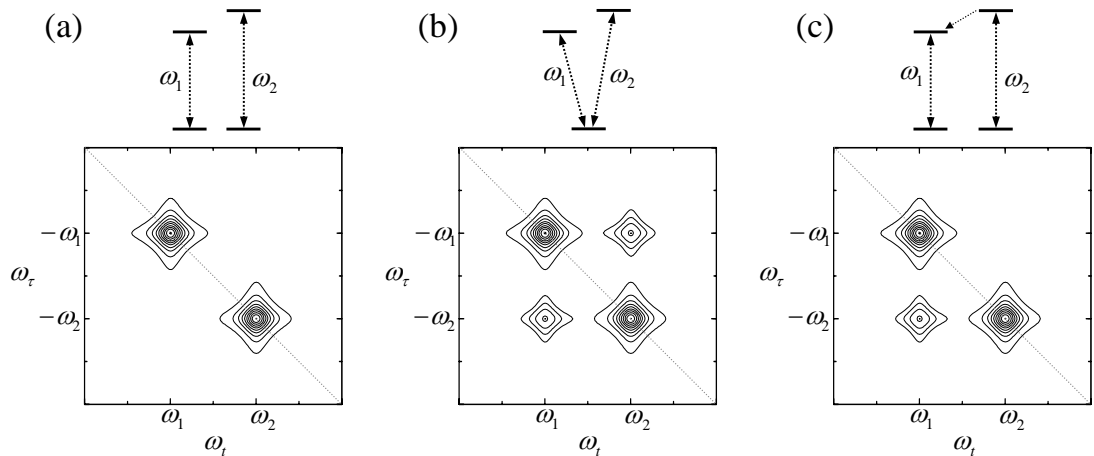

Figure 3.5: (a) A system of two independent two-level transitions and the corresponding 2D spectrum; (b) A 3-level system with shared ground state and the corresponding 2D spectrum; (c) A system of two independent two-level transitions with incoherent population relaxation from higher exited state to lower state and the corresponding 2D spectrum.

peaks appear at $(\omega_1, -\omega_2)$ and $(\omega_2, -\omega_1)$, besides two resonance peaks at $(\omega_1, -\omega_1)$ and $(\omega_2, -\omega_2)$ on the diagonal. Therefore, a 2D spectrum can identify whether two resonances are from two independent transitions (two two-level systems) or from two coupled transitions (a three-level "V" system), while a one-dimensional spectrum such as linear absorption or luminescence gives identical results for these two situations. It is also possible to determine the coupling mechanism in 2D FTS. For example, the two transitions in a two two-level system will not be independent if there is an incoherent non-radiation relaxation happening from the higher excited state to the lower state, as shown in Fig. 3.5(c). This coupling mechanism results in a 2D spectrum with only one cross peak instead of two symmetric ones on both sides of the diagonal. The cross peak appears at the lower-left corner with an absorption frequency (absolute value) greater than the emission frequency, indicating an incoherent population relaxation occurring from the higher excited state to the lower one. This incoherent process generally requires a finite value of the waiting time T.

Furthermore, the interactions of two transitions in a two-two-level system or a three-level "V" system can be studied with 2D FTS, too. A realistic example is the interactions between HH and LH excitons in quantum wells (as discussed in Chapter 2), where a biexciton can form as the bound state of two interacting excitons, with a typical binding energy of $2\sim 4\,\mathrm{meV}$. For the case of scattering between two excitons, it can be treated as an unbound state. This system can be described equivalently as a four-level system consisting of one ground state, two singly-excited states and one doubly-excited state, where the doubly-excited state has an energy level equal to the sum of the transition energy of the two singly-excited states with a shift [4]. The doubly-excited state is shifted lower energetically by an amount equal to the biexciton binding energy for bound two-exciton states or higher by the amount of the scattering energy for unbound two-excitons. The interactions of transitions in such a system can be revealed by 2D spectra in a similar way as couplings. Only two diagonal peaks appear if the

two transitions are independent as in a two-two-level system; however, both peaks are shifted along emission frequency axis, corresponding to the shift of the doubly-excited state. In the case of a three-level "V" system, two off-diagonal peaks also appear as the result of coupling, and all four peaks are shifted along emission frequency axis in the same way as in the case of a two-two-level system. We will find such a behavior in the 2D spectrum excited with cross-linear-polarized light in Chapter 6. Moreover, the interactions of HH and LH excitons with exciton continuum states (electron-hole pairs) can also be reflected in 2D FTS. We will see examples of such spectra in experiments and study the exciton interactions with the continuum numerically in Chapter 5.

Identifying resonance coupling is not a capability unique to 2D FTS. As discussed in Section 3.1 of this chapter, some primitive two-dimensional non-Fourier-transform techniques [7, 49] are also able to make this identification. However, only 2D spectra can provide the complete information needed in an intuitive but general way. Besides, 2D spectra also give further insight into more complicated cases of coupling, such as exciton-exciton correlations and exciton-continuum interactions, which cannot be described in simple level schemes.

3.5.2   Isolation of coherent pathways

Another essential feature of 2D FTS is the ability to isolate contributions of various coherent pathways in Liouville space. As an example, we consider a three-level "V" excitonic system consisting of the ground state, excited HH exciton state $|e_H\rangle$ and LH exciton state $|e_L\rangle$, with respective transition frequency ω_H and ω_L. This is a simplified picture of the exciton energy level scheme shown in Fig. 2.4, without considering the two-exciton states. The double-sided Feynman diagrams representing the coherent pathways for the $\mathcal{S}_I$ 2D spectra can be derived from Fig. 3.2(a), where the singly-excited state $|e\rangle$ and $|e'\rangle$ in Fig. 3.2(d) can be either $|e_H\rangle$ or $|e_L\rangle$. Therefore we obtain four diagrams of type (1) and four of type (2). There is no type (3) diagram

since the doubly-excited level $|f\rangle$ is neglected. The difference between type (1) and type (2) is that during the waiting time period the system in pathways of type (2) is in the excitonic state rather than the ground state as is the case for type (1).
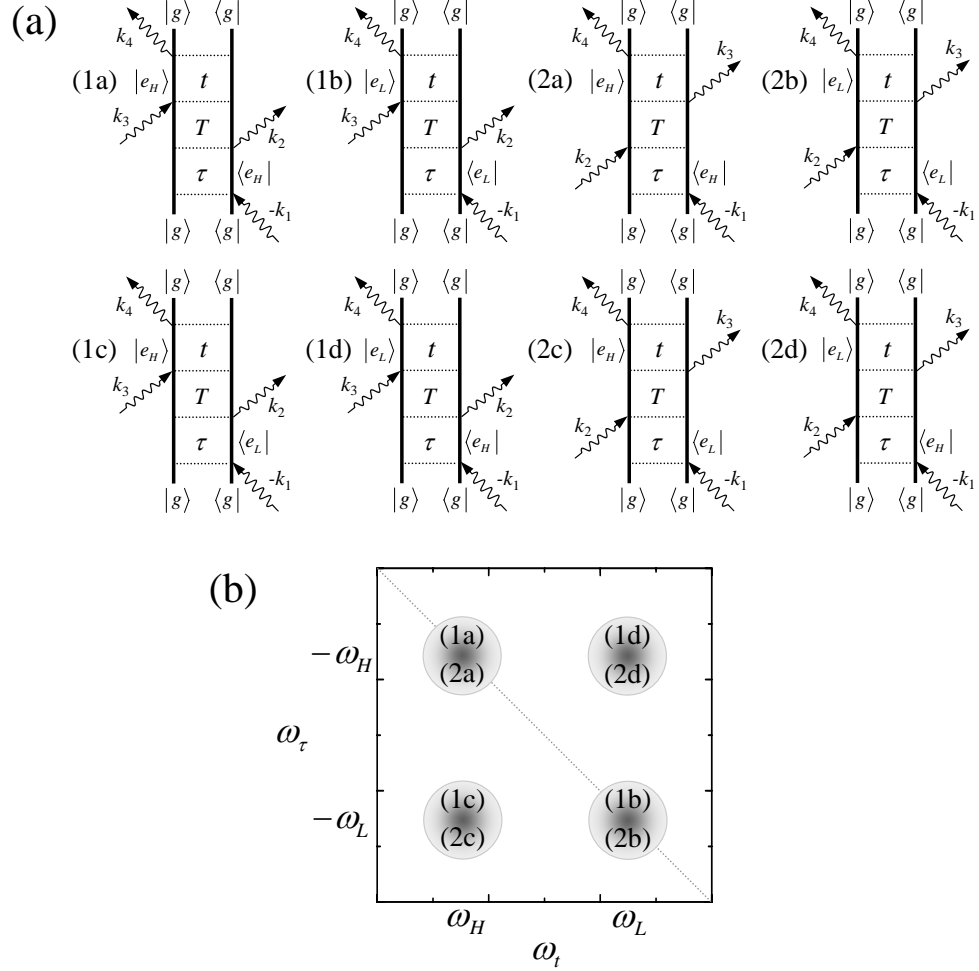
Figure 3.6: (a) Double-sided Feynman diagrams for heavy-hole and light-hole exciton transitions; (b) Isolated contributions of coherent pathways to peaks in 2D spectra.

All eight possible coherent pathways are listed in Fig. 3.6(a), where (1a), (1b), (1c), and (1d) are type (1) diagrams, and (2a), (2b), (2c), and (2d) are type (2) [33]. Pathways (1a) and (2a) occur at the same absorption and emission frequency of ω_H, while (1b) and (2b) occur at both frequencies equal to ω_L. For the other four pathways, the absorption and emission frequencies are not equal: (1c) and (2c) have an absorption

frequency of ω_L and an emission frequency of ω_H, while (1d) and (2d) have an absorption frequency of ω_H and an emission frequency of ω_L. In the corresponding (rephasing) 2D spectrum in Fig. 3.6(b), the diagonal peak at $(\omega_H, -\omega_H)$ is from the contributions of pathways (1a) and (2a), and the other diagonal peak at $(\omega_L, -\omega_L)$ is from pathways (1b) and (2b). The cross peak at $(\omega_H, -\omega_L)$ arises from pathways (1c) and (2c), whereas the other cross peak at $(\omega_L, -\omega_H)$ is from (1d) and (2d). The pathways (1c) and (2c) are well isolated from (1a) and (2a) at emission frequency of ω_H, and (1d) and (2d) are separated from (1b) and (2b) at ω_L. In an one-dimensional spectrally resolved FWM curve, which is the vertical projection of the 2D spectrum, pathways (1c), (2c), (1a), and (2a) ((1d), (2d), (1b), and (2b)) are all mixed together and contribute to the HH exciton (LH exciton) peak. Here, the advantage of spreading out a spectrum along the second dimension by the 2D technique is apparent.

In the following, we examine the contributions of two-exciton states to 2D spectra. The six diagrams with all possible combinations of states $|e\rangle$, $|e'\rangle$, and $|f\rangle$ derived from diagram (3) in Fig. 3.2(a) are listed in Fig. 3.7(a), where $|f_H\rangle$, $|f_L\rangle$, and $|f_M\rangle$ stand for the state of two HH excitons, two LH excitons, and mixed HH and LH excitons, respectively. There are four pathways leading to $|f_M\rangle$, one to $|f_H\rangle$, and one to $|f_L\rangle$. Every diagram contains the contributions from both bound and unbound two-exciton states. The corresponding (rephasing) 2D spectrum is depicted in Fig. 3.7(b), where all peaks are elongated along ω_t axis to demonstrate the effects of red-shift by bound two-excitons (indicated by a suffix "-" to the labels of diagrams) and blue-shift by unbound two-excitons (indicated by a suffix "+"). Determined by the absorption and emission frequencies, each coherent pathway can be associated with either a diagonal peak or an off-diagonal peak. The absorption and emission frequency of pathway (3a) are approximately equal to ω_H, thus it shows up as diagonal peak at $(\omega_H, -\omega_H)$, and the pathway (3b) appears as the other diagonal peak at $(\omega_L, -\omega_L)$. The off-diagonal peak at $(\omega_H, -\omega_L)$ arises as a mixture of pathway (3b') and (3c), while the other off-diagonal
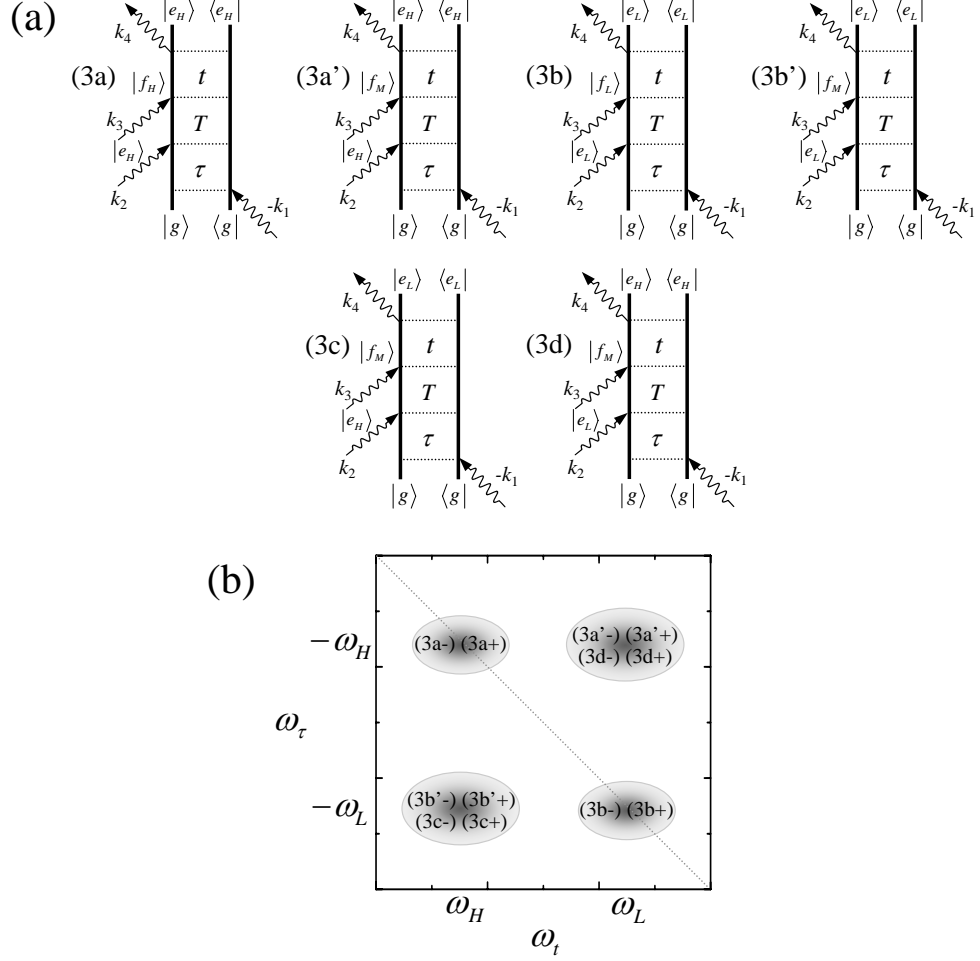
Figure 3.7: (a) Double-sided Feynman diagrams involving bound and unbound two-excitons; (b) Isolated contributions of coherent pathways to peaks in 2D spectra.

peak at $(\omega_L, -\omega_H)$ is due to pathway (3a$'$) and (3d). Similar to Fig. 3.6(b), different coherent pathways are isolated along ω_τ axis as diagonal and off-diagonal peaks at ω_t equal to ω_H and ω_L.

Contributions from HH and LH excitons as well as two-excitons are all presented in the total 2D spectrum in Fig. 3.8(a), which is a combination of Fig. 3.6(b) and Fig. 3.7(b). We compare the total 2D spectrum with a 1D spectrally-resolved FWM in Fig. 3.8(b). Besides contributions of single-exciton pathways (1a), (2a), (1c), and (2c) to the HH exciton peak (labeled as X$_{\text{HH}}$), and (1b), (2b), (1d), and (2d) to the
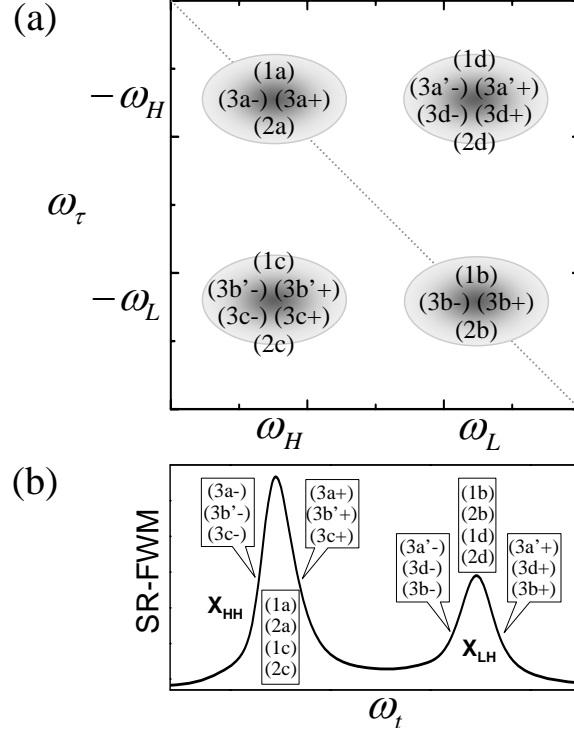
Figure 3.8: Contributions of all coherent pathways including biexciton transitions in 2D spectra (a) and 1D spectrally-resolved FWM (b).

LH exciton peak (X_{LH}), two-exciton pathways also contribute to the wings of peaks. As indicated in Fig. 3.8(b), the bound two-exciton pathways (3a-), (3b′−), and (3c-) and unbound two-exciton pathways (3a+), (3b′+), and (3c+) contribute to the left-hand side and right-hand side of the HH exciton peak (X_{HH}) respectively, whereas pathway (3a′−), (3d-), and (3b-) of bound two-exciton states and (3a′+), (3d+), and (3b+) of unbound two-exciton states show up on the two sides of LH exciton peak (X_{LH}). The typical two-exciton binding energy in GaAs semiconductor quantum wells is $\sim 2\,\mathrm{meV}$, while the energy separation between X_{HH} and X_{LH} is $7 \sim 9\,\mathrm{meV}$. In a small spectral range about $10\,\mathrm{meV}$, there are eight single-exciton contributions and twelve two-exciton contributions, resulting in a very congested 1D FWM spectrum. The presence of exciton homogeneous and inhomogeneous broadening makes the case even worse. 2D

FTS demonstrates its power by spreading out the spectrum along the new ω_τ dimension and attributing peaks to different pathways.

The isolation of coherent pathways can be performed in different schemes by choosing the pair of time periods to be correlated, the pulse sequence, and the spatial arrangement of excitation pulses, thus providing a great flexibility for selecting the contributions of interest. For example, an alternative 2D spectroscopy based on the same $\mathbf{k}_I$ geometry but with a different pair of time variables, T and t instead of τ and t, for Fourier transformations could separate the pathways contributing to the Raman coherence between HH and LH excitons. The implementation of this new 2D spectroscopy will be discussed in Chapter 7.

As another example, we inspect how coherent pathways can be isolated differently by selecting the excitation pulse sequence. To illustrate this, the double-sided Feynman diagrams for pathways contributing to the nonlinear signal from a 3-level "V" system are depicted in Fig. 3.6(a) and Fig. 3.9(a), for rephasing and non-rephasing pulse sequences, respectively. In the rephasing case, there are eight pathways, where pathways (1a) and (2a), (1b) and (2b), (1c) and (2c), and (1d) and (2d) contribute to peaks $(\omega_H, -\omega_H)$, $(\omega_L, -\omega_L)$, $(\omega_H, -\omega_L)$, and $(\omega_L, -\omega_H)$, respectively, in the rephasing 2D spectrum in Fig. 3.6(b). There are also eight pathways in the non-rephasing case. Pathways (n1a), (n2a), and (n1c) contribute to peak (ω_H, ω_H), (n1b), (n2b), and (n1d) to peak (ω_L, ω_L), (n2c) to peak (ω_L, ω_H), and (n2d) to peak (ω_H, ω_L) in the non-rephasing 2D spectrum in Fig. 3.9(b). In this case pathways (n2c) and (n2d) are separated as cross peaks. The pathways isolated in a different scheme for the non-rephasing pulse sequence can provide supplemental information to rephasing pathways.
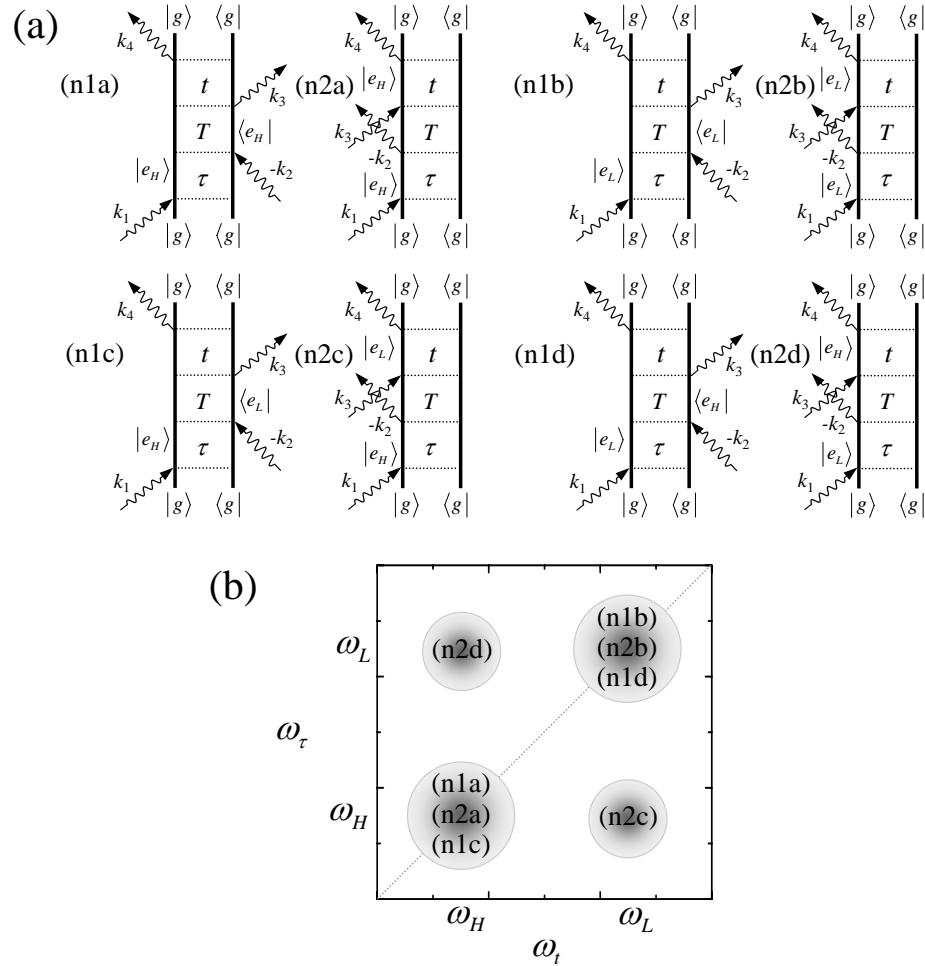
Figure 3.9: (a) Double-sided Feynman diagrams for the non-rephasing pulse sequence; (b) Isolated contributions of coherent pathways to peaks in non-rephasing 2D spectra.

3.5.3 Other capabilities of 2D FTS

Besides the capabilities of identifying resonance coupling and isolating coherent pathways, there are some more advantageous features in 2D FTS. One that is of particular importance for complicated spectra is the ability to represent inhomogeneous broadening as an elongation along the diagonal, therefore inhomogeneous broadening can be separated from homogeneous broadening to provide valuable information about the fluctuations of oscillators in the ensemble. With inhomogeneous broadening represented on the diagonal, identification of coupling of resonances and isolation of pathways

are possible even in the presence of strong inhomogeneity.

Furthermore, the time resolution of 2D spectra is determined by excitation pulse width and the frequency resolution is limited by pulse separation, therefore overcoming the compromise between time and frequency resolutions imposed by the time-bandwidth product [76]. Consequently, 2D FTS technique can capture the fast dynamics with femtosecond time resolution in a broad spectral range covering all resonances of interest, while every individual resonance is well characterized spectrally.

Another advantage of 2D spectra is the preservation of phase information. With full signal information preserved, many conventional spectroscopic results can be produced as various projections of 2D spectra. For example, a vertical projection along ω_τ axis provides the spectrally-resolved FWM field, from which the time-resolved signal can also be retrieved by an inverse Fourier transform with respect to ω_t. The absorption spectra can be obtained from the projection along ω_t axis. Moreover, the spectrally-resolved differential transmission from a pump-probe measurement is equal to the product of the real part 2D projection along ω_τ axis and the probe electric field. In general, a complex 2D spectrum with a correct global phase can be presented in separate real and imaginary parts that are linked by the Kramers-Kronig relation. The lineshape resolution is improved in the absorptive spectra by removing the dispersive lineshape with long wings that tends to blur peaks. In addition, the phase information is of great value in distinguishing microscopic mechanisms for many-body interactions, where ambiguity arises due to the lack of information in conventional time or frequency domain FWM experiments.

With all these advantageous features, 2D FTS technique is being adopted as a promising tool in the studies of exciton dynamics, many-body interactions, and disorders in semiconductors. We will discuss the development of 2D FTS experiments in near-IR wavelength for semiconductors in the next chapter.

Chapter 4

2D FTS Experiments with Active Interferometric Stabilization

Optical 2D FTS experiments are commonly implemented with impulsive time-domain techniques. The excitation pulses are scanned with sub-optical-cycle step size and the corresponding change of signal phase is tracked coherently. Due to the nature of sensitive phase measurement, it is of critical importance to have high phase stability and pulse positioning accuracy in 2D FTS experiments. The mechanical instability of the optical mounts and the positioning inaccuracy of the delay stages can introduce significant fluctuations in beam direction and optical path length, resulting in degraded 2D spectra with artifacts such as ghost peaks. Compared to 2D IR experiments, the requirement for phase accuracy is more demanding in near-IR or visible wavelength range, as the relative phase fluctuation increases at shorter wavelengths. Therefore, the implementation of 2D FTS is experimentally challenging, and a delicate apparatus with special designs to improve phase stability is generally essential.

4.1   Implementations of 2D FTS with phase stability

Various approaches have been developed to implement 2D FTS experiment with high phase stability and pulse positioning accuracy. One method is to maximize the stability of the apparatus passively and measure the phase delays [10, 76]. The measured data are resampled to correct phase errors, however, it must be done with great care.

Passive phase stability for 2D experiments was accomplished with diffractive optics [16, 17, 18, 19]. Three excitation pulses and a local oscillator are generated as the first-order diffraction from a diffractive optic and thus inherently phase stable. 2D IR spectra were obtained [108] and the ultrafast hydrogen bond network dynamics in liquid water was studied [15]. Electronic couplings in the molecular complex of photonsynthetic protein were studied with 2D spectra in the visible range [78, 80]. However, the diffractive optics method suffers from limited delay range provided by movable glass wedges in IR spectroscopy, where the slow dephasing of vibrational states requires quite long time scan. Adding delay with a translation stage destroys the inherent phase stability. Although phase stability can be maintained when a delay stage is added in a way that does not affect the difference in the relative delay between the first two pulses and between the third pulse and the local oscillator [108], the delays cannot be scanned independently. Besides, the local oscillator passes through the excited spot on the sample in this geometry, resulting in undesirable dynamical modifications to systems with strong excitation-induced effects, such as semiconductors.

Femtosecond pulse shaping techniques are applied to generate an inherently phase-stable excitation pulse sequence for 2D FTS experiments [20, 22]. Pulse timing, phase, and waveform shape are well specified, with optical coherence among all pulses. A collinear three-pulse train created by an acousto-optic pulse shaper with well controlled and scannable interpulse delays and phases was used to excite 2D spectra of atomic Rubidium vapor [21]. In this collinear geometry, the desired nonlinear coherent pathways are selected by phase cycling schemes [20] that are routinely performed in 2D NMR, as discussed in Section 3.1. Diffraction based two-dimensional pulse shaping is developed to produce multiple non-collinear phase-stable femtosecond pulses in a phase-matched FWM geometry [22]. Combining the waveform generation capability of multidimensional NMR with the wavevector specification and phase-matching feature of non-collinear optical spectroscopy, this technique accomplishes a new level of

spatial and temporal control over excitation pulses and selectivity of coherence pathways. 2D spectra of prototype systems including Rubidium vapor and semiconductor quantum well structures were produced [109, 110]. There are certain limitations in pulse-shaping techniques. For example, spurious pulses often overlap with main peaks from an acousto-optic pulse shaper in time-domain and cause harmful amplitude modulation. Furthermore, the range of interpulse delays is constrained by the frequency resolution to about tens of picoseconds. This restriction causes difficulties to experiments of longer time scan, such as population relaxation studies of semiconductors. Similar to the approach of diffractive optics, unwanted dynamical modifications by the local oscillator can also be a problem in pulse shaping techniques.

Active phase stabilization has been developed for conventional non-collinear coherent optical spectroscopy [23, 24]. The incorporated phase stability does not compromise the non-collinear configuration for phase-matching and the flexibility of control over excitation pulses. We have implemented 2D FTS for the studies of semiconductors at near-visible wavelengths around 800 nm [24]. Two separate interferometers and feedback loops are used to maintain superior stability of relative phase between the first two excitation pulses and between the third pulse and a reference pulse (local oscillator). The delay between the first two pulses is scanned with interferometric accuracy. The measurement of the optical phase is accomplished by heterodyne detection of the nonlinear signal with the reference. The 2D FTS experimental setup is depicted in Fig. 4.1, where the FWM signal generation and heterodyne detection, the excitation pulse stabilization interferometer, and the reference stabilization interferometer are shown. Detailed technical aspects of the experiments are presented in the following sections of this chapter.
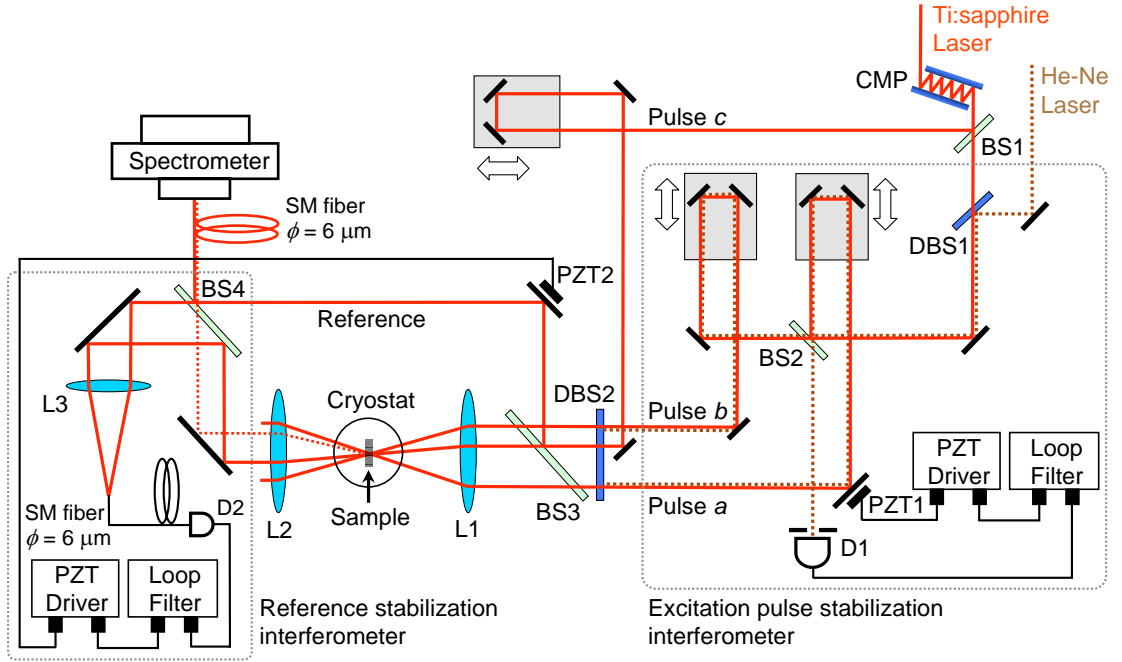
Figure 4.1: The experimental setup for 2D Fourier transform spectroscopy with active interferometric stabilization. FWM is generated in a standard box geometry. The delay between the first two excitation pulses is stabilized and scanned by a stabilization interferometer (enclosed in the right box). The phase of the reference is locked to that of the third pulse by another stabilization interferometer (enclosed in the left box). CMP: chirped mirror pair; BS1-4: beam splitters; DBS1-2: dichroic beam splitters; L1-3: focal lens; D1-2: photodiode detectors; PZT1-2: piezoelectric transducers.

4.2   Four-wave mixing generation

The standard box geometry depicted in Fig. 3.3 is used for FWM generation in 2D FTS experiments. Three excitation beams are produced from a Kerr-lens mode-locked Ti:sapphire laser with a pulse duration of 100 fs and a repetition rate of 76 MHz. The wavelength of all three beams is identical and tunable around 800 nm. The beams are arranged on the three corners of a square on a singlet lens (L1 in Fig. 4.1) of 20 cm focal length to propagate with wavevectors $\mathbf{k}_a$, $\mathbf{k}_b$, and $\mathbf{k}_c$ before focused on a sample. The FWM signal generated by all three beams is emitted in the phase-matched direction $-\mathbf{k}_a + \mathbf{k}_b + \mathbf{k}_c$. With such a non-collinear three-pulse geometry, the nonlinear coherence

pathway can be selected with the phase-matched direction, temporal pulse ordering, and Fourier transform variables. The polarization orientations of all beams are aligned by polarizers and manipulated by half-wave plates or quarter-wave plates (not shown in Fig. 4.1) in front of the focusing lens L1, thus different polarization configuration of excitation beams can be applied.
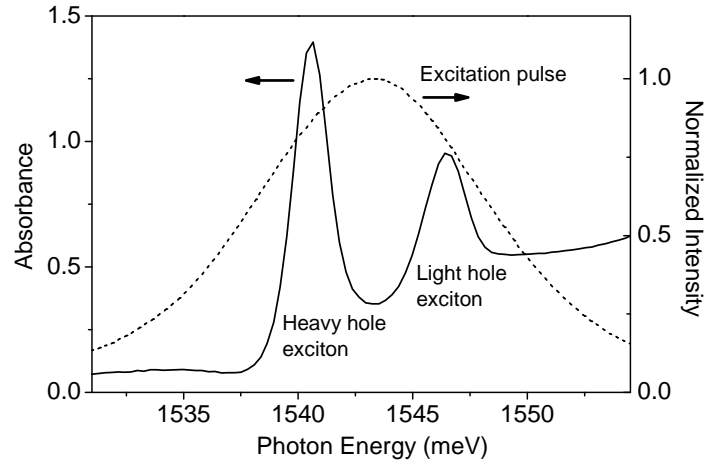
Figure 4.2: Linear absorption of the $GaAs/Al_{0.3}Ga_{0.7}As$ multiple-quantum well sample (solid line) and the excitation pulse spectrum (dash line).

A typical sample is a $GaAs/Al_{0.3}Ga_{0.7}As$ multiple quantum well structure consisting of 10 periods 10 nm well and 10 nm barrier grown by molecular beam epitaxy. The heterostructure is affixed to a wedged sapphire plate and the substrate is removed by lapping and chemical etching. The sample is held below 10 K in a cold-finger cryostat with continuous liquid-Helium flow. As depicted in Fig. 4.2, linear absorption spectrum of the sample displays prominent resonance peaks of HH and LH excitons with an energy separation of about 6 meV. The excitation pulses have sufficient bandwidth to excite both excitonic resonances and create unbound electron-hole pairs. The HH exciton has a linewidth of ~ 1.5 meV, due in part to inhomogeneous broadening from well-width fluctuations. At the excitation densities of $\sim 10^{10}$ excitons/well/cm^2, the homogeneous linewidth is ~ 0.8 meV from a TI FWM measurement. The spectral positions of the

resonances are sensitive to strain arising from the difference in thermal coefficient of expansion between the sample and sapphire plate and the mechanical strain imposed by mounting the plate to cold-finger. Consequently, the excitonic peak positions vary slightly in spectra of samples from the same wafer.

As depicted in Fig. 4.1, the emitted FWM signal is collimated by a lens (L2) identical to the focal lens before the sample. The signal is then combined on a beam splitter (BS4) with a reference beam, which is split from the third beam before the sample and routed around the cryostat. With such a design, the reference does not pass through the sample, thus undesired dynamical modification to the excitation is avoided. The combined signal and reference are coupled into a single-mode fiber and transmitted to a grating spectrograph, and the resulting spectral interferogram is recorded with a CCD camera. The complex FWM spectrum, i.e. amplitude and phase, is retrieved from the interferogram [36].

4.3   Interferometric phase stabilization

The delay τ between excitation pulses a and b is stabilized and scanned by an interferometer formed with a separate Helium-Neon (He-Ne) CW laser, as shown in the right box in Fig. 4.1. The He-Ne laser follows the same optical path of the Ti:sapphire beam between two dichroic beam splitters, DBS1 and DBS2, to form a folded Michelson interferometer with the beam paths of pulse a and b as the two arms. The second dichroic beam splitter (DBS2) is common to both arms of the interferometer. This design relies on the fact that rotational motion of the dichroic is minimal. The recombined He-Ne beam exiting the interferometer is detected with a silicon photodiode (D1). The error signal monitoring the relative arm length is sent to a loop filter and fed back to a piezoelectric actuator (PZT1) mounted on the back of a mirror in one arm, which corrects for any fluctuation. The servo loop is enabled by computer control to stabilize τ

during data acquisition of the FWM signal and disabled to allow scanning τ. Fig. 4.3(a) presents the phase errors with unlocked and locked τ from the He-Ne interferometer in a scan. Fluctuations in the error signal drops to below 1% when the servo loop is enabled. Taking into account the fact that the He-Ne beam passes the interferometer twice, the phase error between pulses a and b is reduced to less than 0.5% of one optical-cycle. Thus the phase fluctuation is suppressed to below $0.01\,\pi$ (peak-to-peak deviation) by active stabilization.
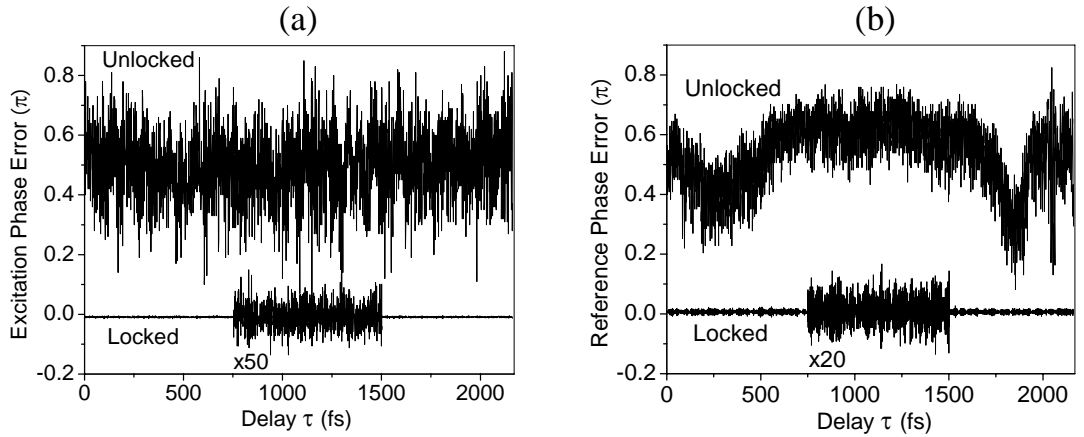
Figure 4.3: (a) Error signal from the excitation phase stabilization interferometer with unlocked and locked delay τ; (b) Error signal from the reference stabilization interferometer while reference phase is unlocked and locked. Each locked error signal is shown in smaller scale in inset.

After acquiring the nonlinear signal at a delay τ, the feedback loop is disabled and τ is increased by stepping a picomotor actuator with step size of $\sim 30\,\mathrm{nm}$. The fringes of He-Ne interferometer cycle through one period when the beam path length changes by one-half of the He-Ne laser wavelength, $316.4\,\mathrm{nm}$, or $1.06\,\mathrm{fs}$ in delay change of τ. The He-Ne interference signal is monitored during the stepping of picomotor, and an overall offset is removed to make the fringes oscillate symmetrically around zero. Once the signal crosses the zero level, the servo loop is enabled to lock delay τ at the steepest slope of the fringe. The change of path length from one locking point to another is exactly $316.4\,\mathrm{nm}$, as the small error due to overshooting zero by a partial

step is eliminated by the servo loop after locking is established. Fig. 4.4(a) shows the tracked intensity of He-Ne fringes during stepping, where the circled dots are the locking positions of τ. The length of picomotor step is not uniform, thus the number of steps between two signal acquisitions presents a distribution. As shown in Fig. 4.4(b), the distribution indicates a scan of one-half He-Ne wavelength is completed in 10 steps most of the time. The same process of locking, acquiring, and stepping is repeated for every delay τ until all signal measurements are completed, as illustrated by the flowchart in Fig. 4.4(c).
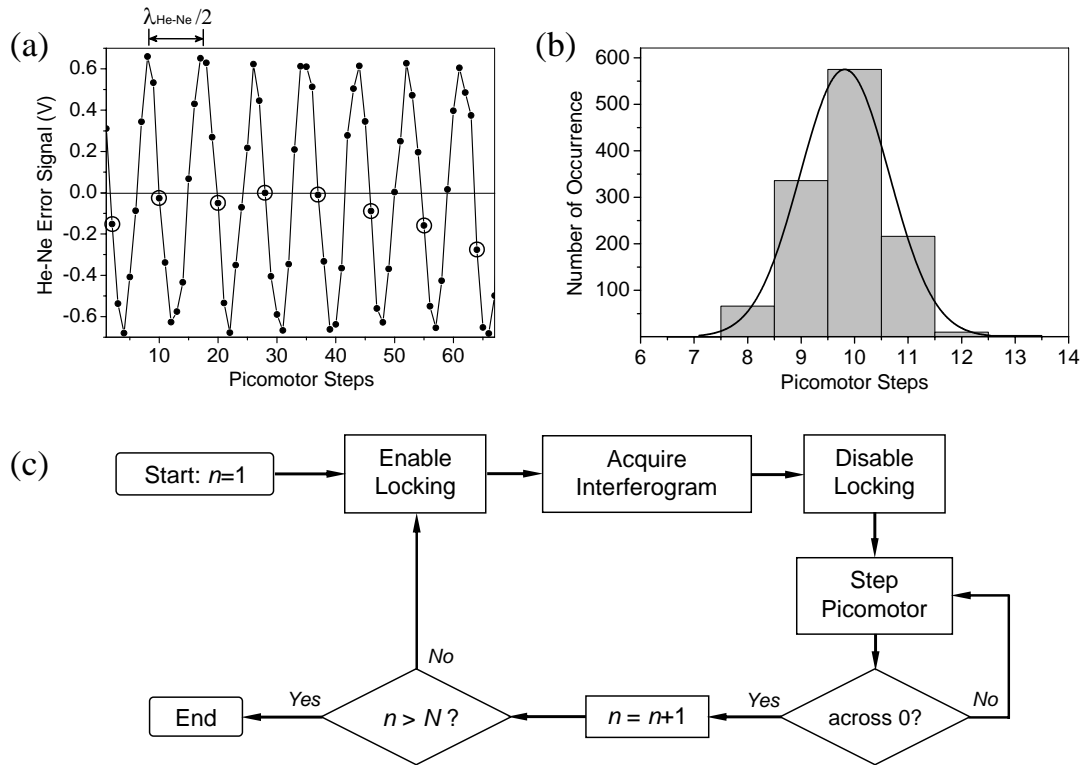
Figure 4.4: (a) The error signal from the He-Ne interferometer during locking and stepping (the circled dots are where delay τ is locked); (b) A histogram that presents the distribution of the number of picomotor steps per measurement in a 2D experiment of 1200 measurements; (c) The whole process of phase locking, spectrum acquiring, and τ stepping in a 2D FTS experiment. N is the total number of measurements.

The reference derived from the third excitation beam is combined with the FWM signal at a beam splitter (BS4) of 10% reflectivity. Glass wedges and a pair of singlet

lens identical to L1 and L2 are inserted into the reference path (not shown in Fig. 4.1) to compensate for the delay and chirp introduced by the sample, cryostat windows and lenses. Fluctuation in the relative path length between reference and the third pulse are significant due to the turbulent air flow around the cold cryostat used to hold and cool the sample. Therefore it is necessary to actively stabilize the phase relative to that of the third beam. As depicted in the left box in Fig. 4.1, a Mach-Zehnder interferometer is formed with the transmitted reference and the third beam. The two beams are focused with a 20 cm singlet focal lens (L3) onto to one end of a single-mode fiber (mode field diameter 5.6 μm), where a spatial fringe pattern is formed with fringe spacing much larger than the fiber core. The resulting interferometric error signal is detected with a high gain photo detector (D2). The error signal is fed back to drive a piezoelectric actuator (PZT2), which moves a mirror in the reference beam to compensate the path length fluctuation. Fig. 4.3(b) shows the error signal from the reference stabilization interferometer, where the fluctuation of relative path length is reduced to less than 5% of one wavelength when the servo loop is enabled. The reference phase is locked to a fixed value with peak-to-peak deviation below 0.1π in the whole 2D data-taking time (several hours). In a long period of time, the drift of relative path length can be quite significant, as exacerbated by the presence of the cryostat. The phase drift is monitored with the PZT driving voltage and canceled by moving the glass wedge in the reference used for delay compensation.

During long data acquisition time, the laser beam direction usually also needs to be actively stabilized. The drift in horizontal and vertical directions are monitored by a pair of quadrant detectors and stabilized by a turning mirror with piezoelectric actuators in a feedback loop. The experimental setup is enclosed in a sturdy acrylic box to minimize the influences of air flow, environmental noise and temperature variations.

4.4   Fourier transform spectral interferometry

The FWM signal is measured by heterodyne detection with the reference to obtain full information of amplitude and phase [36, 111]. The spectral interferogram of the FWM and reference is recorded by a $0.75\,\mathrm{m}$ imaging spectrograph and a CCD camera. The thermo-electric cooled CCD has a 1024×256 array of $26\,\mu\mathrm{m}$ pixels and a dynamic range of 16 bits. The collinear signal and reference beams are focused with a $10\times$ microscope objective into a single-mode fiber to ensure complete spatial mode-matching for interference. The fiber has a numeric aperture of 0.12 and a mode field diameter of $5.6\,\mu\mathrm{m}$. A linear polarizer is placed in front of the fiber to ensure accurate polarization alignment. The light exiting the fiber is coupled directly into the spectrograph entrance slit and a spectral resolution of $0.1\,\mathrm{nm}$ is achieved. The FWM signal arrives after the reference with a delay adjustable by the glass wedge in the reference. The delay, denoted as τ_0, is set to a large enough value so that a spectral interferogram with dense fringes is resulted. The maximal density of fringes is limited by the spectral resolution. The intensity ratio of FWM signal to reference is set to 1/10 initially at $\tau = 0$ and the interferogram intensity is adjusted to utilize the full dynamic range of the CCD in spectral measurements.

The intensity of the spectral interferogram between FWM and reference can be expressed as [36]:

$$|E(\omega_t) + E_0(\omega_t)|^2 = |E(\omega_t)|^2 + |E_0(\omega_t)|^2 + 2\mathcal{R}e[\,E(\omega_t)E_0^*(\omega_t)\,e^{i\omega_t\tau_0}\,]\,, \qquad (4.1)$$

where $E(\omega_t)$ and $E_0(\omega_t)$ are the respective electric field of the signal and reference, and τ_0 is the delay between the two fields. In Fig. 4.5(a), the power spectra of the FWM and reference, $|E(\omega_t)|^2$ and $|E_0(\omega_t)|^2$, and their interferogram in a measurement are plotted, where the reference bandwidth is broad enough to cover the whole signal spectrum. There are about 40 interference fringes in the signal range, with a delay τ_0 equal to $7.0\,\mathrm{ps}$. The third term in the right-hand side of Eqn.(4.1) is the interferometric term

with rapid oscillatory fringes, which can be separated by subtracting the power spectra of signal and reference from the interferogram. The net interferometric term is shown in Fig. 4.5(b).
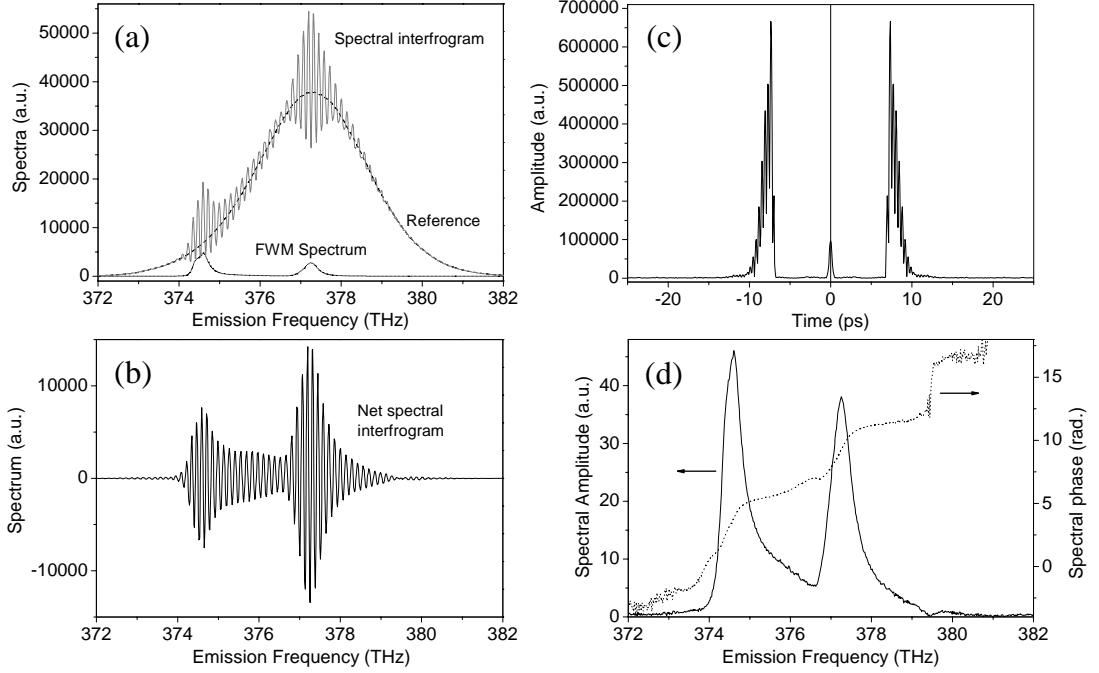
Figure 4.5: Full information of FWM signal including amplitude and phase is retrieved by Fourier transform spectral interferometry. (a) The power spectra of the FWM and reference, and their spectral interferogram; (b) The net interferometric term obtained by subtracting the power spectra of FWM and reference from the interferogram; (c) The inverse Fourier transform of the interferometric part contains two terms that are time-reversed from each other in time-domain; (d) The retrieved spectral amplitude (solid line) and phase (dot line) of the FWM signal.

Since the net interferometric term, $S(\omega_t) = 2\mathcal{R}e\,[\,E(\omega_t)E_0^*(\omega_t)\,e^{\,i\omega_t\tau_0}]$, is real, its inverse Fourier transform contains two terms that are time-reversed from each other and separated by $2\,\tau_0$ in time-domain:

$$s(t) = \mathcal{F}^{-1}[\,S(\omega_t)\,] = f(t-\tau_0) + f(-t-\tau_0)\;, \qquad\qquad (4.2)$$

where $\mathcal{F}^{-1}$ stands for the inverse Fourier transform, and the term $f(t-\tau_0)$ and $f(-t-\tau_0)$ correspond to the peak of positive time and negative time in Fig. 4.5(c), respectively. In

general, the transient FWM signal has a fast leading edge followed by a long decay tail in time-domain, and its time-domain interferogram with the reference should present a similar shape with the addition of fringes. Only the term $f(t - \tau_0)$ has the appropriate behavior that satisfies the causality principle. In Fig. 4.5(c), the small feature around time zero corresponds to the slow-varying and DC components in an imperfect spectral interferogram. The delay of the interferogram from time zero, is equal to that between the FWM and reference in spectral interferogram. With large enough τ_0, the term $f(t - \tau_0)$ can be well isolated from $f(-t - \tau_0)$ and the component around time zero. A Fourier transform of $f(t - \tau)$ recovers the complex spectral amplitude and phase of the FWM, which can be expressed in the following [36]:

$$E(\omega_t) = \frac{\mathcal{F}[\,\Theta(t - t_0)\,\mathcal{F}^{-1}[S(\omega_t)]\,]\,e^{-i\omega_t\tau_0}}{E_0^*(\omega_t)} \quad , \tag{4.3}$$

where $\Theta(t - t_0)$ is the Heaviside step function rising from t_0 to isolate $f(t - \tau_0)$ out of the inverse Fourier transform of $S(\omega_t)$, and $\mathcal{F}$ stands for the forward Fourier transform. The complex exponential term $e^{-i\omega_t\tau_0}$ is multiplied to remove the linear phase associated with delay τ_0. Fig. 4.5(d) shows the retrieved FWM amplitude and phase in frequency-domain.

Strictly speaking, the phase measured is the difference between the signal phase, $\phi(\omega_t)$, and reference phase, $\phi_0(\omega_t)$. The reference has a flat phase as a transform-limited pulse, which is accomplished with a chirped mirror pair (CMP in Fig. 4.1) to compensate the material dispersion gained from the optics in the setup. However, the constant phase of the reference is unknown in heterodyne detection, resulting in an unknown offset in the signal phase. This offset can be determined by a separate pump-probe experiment, as discussed in the next section.

4.5   Generating 2D Fourier transform spectra

The process of Fourier transform spectral interferometry is applied to every interferogram acquired while scanning delay τ. In general, τ is scanned with a step size equal to one half of a He-Ne wavelength, or 1.06 fs in delay change. A few thousand steps are usually needed to reach a delay of several picoseconds until the FWM signal decays completely to the background level. For example, a scan of 8192 steps covers a delay range of 8.68 ps, providing a spectral limit of 473.61 THz (Nyquist frequency) with a resolution of 0.12 THz for the absorption frequency ω_τ after Fourier transform.

The 2D FTS experiment can be quite time consuming with a slow dephasing signal, such as that from a high-quality quantum well with a narrow excitonic linewidth. In this case, undersampling with larger step size is favorable to speed up the measurement. A sampling frequency below that required by the Nyquist sampling theorem would result in an aliasing problem [112]. However, if the spectral bandwidth of signal is sufficiently narrow, the aliasing can be exploited with an appropriate undersampling rate. For the FWM signal from excited HH and LH excitons in quantum wells, the bandwidth is within 10 THz (see Fig. 4.5). If τ is scanned in such a way that two full He-Ne fringes are cycled in the error signal before each acquisition, undersampling is resulted as the Nyquist frequency of 236.81 THz is far below the upper-limit of the signal oscillation frequency, 380 THz. An image spectral peak appears around 98.5 THz, within a bandwidth of 10 THz. The real signal spectrum is recovered from the image peak by folding it around the Nyquist frequency. Similarly, higher undersampling ratio such as 4 or 8 can be used in experiments to significantly shorten the measurement duration and reduce the long-term stabilization issues.

Before the Fourier transform along τ axis, we can verify the performance of phase stabilization and stepping in an experiment by analyzing the phase evolution with τ. In addition to testing the entire apparatus, it also serves as an out-of-loop characterization

of the data in a 2D measurement, whereas the error signals presented in Fig. 4.3(a) and (b) are in-loop. According to Eqn. (3.18), the change of signal phase at a certain emission frequency ω_t is $\Delta\phi = \omega_t \Delta\tau = 2\pi\nu_t\Delta\tau$, where the delay change between two acquisitions of spectral interferograms is $\Delta\tau = 1.06\,\text{fs}$. At the HH exciton resonant frequency $\nu_t = 372.12\,\text{THz}$, the phase change is $\Delta\phi = 0.79\,\pi$. This constant value is subtracted from the phase change of the retrieved FWM signal at 372.12 THz, leaving a residual fluctuation shown in Fig. 4.6. Only the first half portion of a whole 2D FTS measurement with adequate signal strength is shown. The experimental result of phase change agrees with the expected value quite well, with a mean error of $0.02\,\pi$ and a standard deviation of $0.06\,\pi$. These results are consistent with the phase stability of the excitation and reference, $0.01\,\pi$ and $0.10\,\pi$ (peak-to-peak deviation), respectively. Note that this analysis is only valid if the signal is dominated by a diagonal peak. The presence of a cross peak with the LH exciton resonance adds a systematic variation to the phase, worsening the apparent fluctuations.

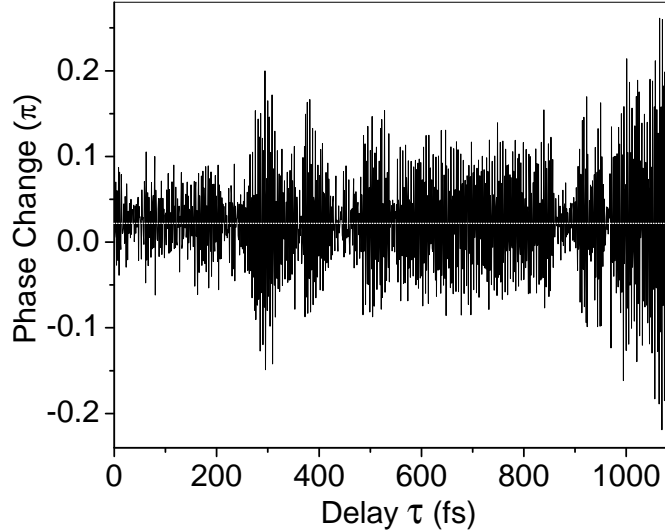Figure 4.6: The fluctuation of signal phase change as a function of delay τ at the HH resonant frequency 372.12 THz. The nominal value of $0.79\,\pi$ has been subtracted, leaving a mean error of $0.02\,\pi$ and a standard deviation of $0.06\,\pi$.

All retrieved spectra form a 2D map of complex FWM electric field as a function of the emission frequency ω_t and delay τ. A Fourier transform with respect to τ produces the 2D spectrum with emission frequency ω_t and absorption frequency ω_τ. The complex 2D spectrum can be represented in plots of real and imaginary parts if the global constant phase is known. However, there is an ambiguity in the global 2D phase resulting from the aforementioned offset in retrieved FWM phase that is not determined in Fourier transform spectral interferometry. The global 2D phase can be determined with the spectrally-resolved differential transmission (SRDT) measured in an independent pump-probe measurement. A tracer beam that comes from the fourth corner of the square on lens L1 in Fig. 4.1 and travels along the signal path is used as the probe, whereas the third beam is treated as the pump. The beam power is carefully chosen to reproduce the excitation conditions in 2D FTS experiments since excitation-induced effects dominate the optical nonlinear response of semiconductors. Therefore the pump is set to a power equal to the sum of the first two beams and the probe power is half of that. The delay between pump and probe is identical to the waiting time T used in FWM generation. The SRDT signal is obtained as the change in transmitted probe spectrum induced by the pump. With identical transform-limited excitation pulses, the SRDT signal is given by the real-part product of the 2D projection to ω_t axis and the probe electric field [75]:

$$\Delta \mathcal{T}_{\mathrm{pp}}(\omega_t, T) \propto \mathcal{R}e \left[E_{\mathrm{pr}}(\omega_t) \int_{-\infty}^{\infty} \mathcal{S}_{2D}(\omega_\tau, T, \omega_t) \, d\omega_\tau \right] , \qquad (4.4)$$

where $E_{\mathrm{pr}}(\omega_t)$ is the probe electric field, and $\Delta \mathcal{T}_{\mathrm{pp}}(\omega_t, T)$ is the SRDT spectrum, with a delay T between the pump and probe pulses. Equivalently, the integral in Eqn. (4.4) can be substituted by $E(0, T, \omega_t)$, the electric field of FWM at $\tau = 0$. In data processing, a constant phase rotation is applied to the retrieved FWM field at $\tau = 0$ and its product with the probe electric field is least-squared fit to the SRDT spectrum. The optimized constant phase in the fit is the global phase of the 2D spectrum. In Fig. 4.7, a typical pump-probe measurement of SRDT (dotted line) is shown with the optimized

fit by correcting the spectral phase of FWM at $\tau = 0$ (solid line), where the maximal mismatch is below 10%.
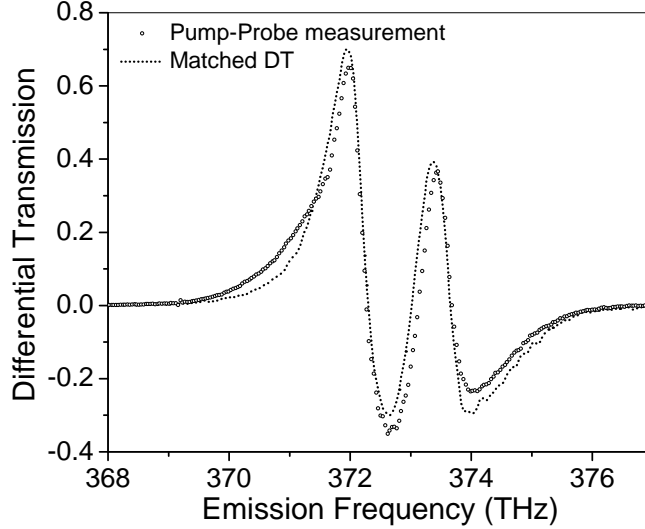
Figure 4.7: A typical pump-probe measurement of SRDT (open circle) and its least-squared fit by correcting the spectral phase of FWM at $\tau = 0$ (dot line). The maximal mismatch is below 10%.

4.6   Primary experimental results

Using the 2D FTS apparatus with active interferometric stabilization, we have performed experiments to study the optical excitations in GaAs multiple quantum wells. The dependence of TI FWM intensity on the power of excitation beams is measured first to determine the excitation density for 2D FTS experiments. The TI FWM is taken by lock-in detection at τ corresponding to the peak of the signal and T matching that used in 2D measures. As depicted in Fig. 4.8, the TI intensity increases from the weak excitation limit as the cube of the excitation power, until saturation starts at about $1\,\text{mW}$. Usually experiments are performed in the cubic range in order to compare with theory in the $\chi^{(3)}$ limit. An excitation power of $1.6\,\text{mW}$ per beam is used to obtain 2D spectra with good signal-to-noise ratio, with an excitation dependence close to cubic.

Figure 4.8: The dependence of TI FWM intensity on the power of excitation beams. 2D experiments were performed with an excitation power of 1.6 mW per beam.
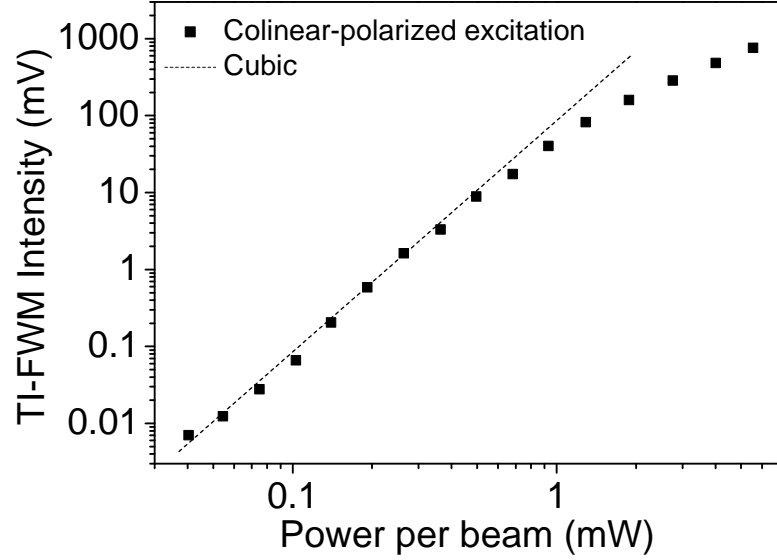
The corresponding excitation density is on the order of 10^{10} excitons/well/cm^2.

The linear absorption of the sample described in Section 4.2 is shown in Fig. 4.9(a), along with the excitation pulse spectrum. The laser is tuned a few meV above the LH exciton resonance in order to compensate the oscillator strength and excite HH and LH excitons, and exciton continuum (unbound electron-hole pairs) simultaneously. With an energy separation of ~ 6 meV between HH and LH excitons, which is close to the exciton binding energy, the LH exciton is degenerate with the edge of the HH exciton continuum. All three excitation beams have the same linear polarization orientation.

An amplitude 2D Fourier transform spectrum of rephasing pathway is shown in Fig. 4.9(b). Diagonal peaks corresponding to HH and LH exciton resonances arise from oscillations at the same frequency during absorption and emission time periods, whereas off-diagonal peaks unveil that the oscillation frequency changes during or between the two periods as a result of coupling between the two resonances. With collinear-polarized excitation, the HH and LH exciton resonances are coupled through common conduction
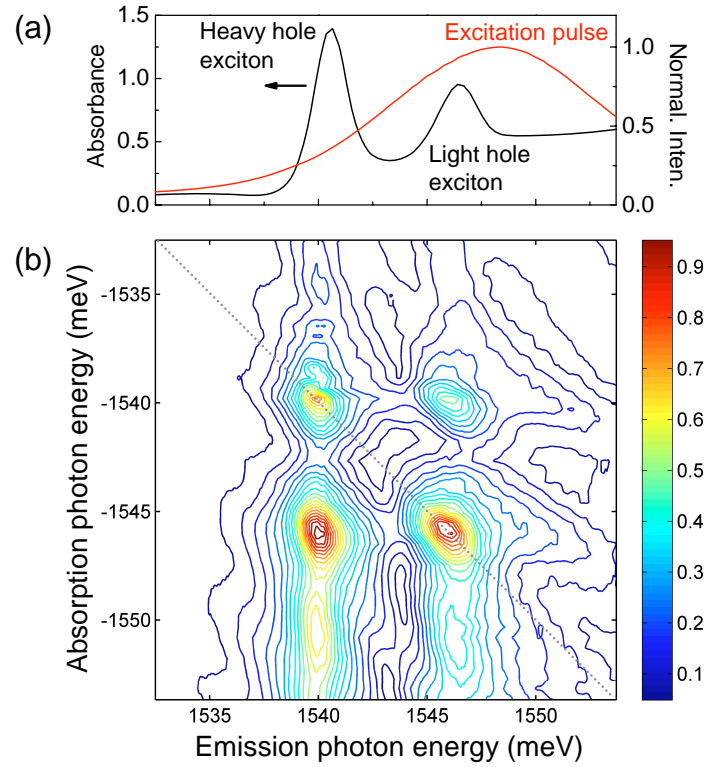
Figure 4.9: (a) Linear absorption of the GaAs/Al$_{0.3}$Ga$_{0.7}$As multiple quantum well sample (black) and the excitation pulse spectrum (red); (b) Amplitude 2D spectrum of rephasing pathway with colinear-polarized excitation. The normalized spectral strength is represented with 20 contour lines.

band states while different valence bands are involved. The dynamics of the coupled resonances can be modeled with the three-level "V" system discussed in Section 3.5, without considering the doubly-excited states and polarization selection rules [4]. The waiting time T is set to 100 fs to avoid other coherent orders when the excitation pulses overlap temporally. There is no qualitative difference in separate experiments with $T = 0$ (not shown).

In the amplitude 2D spectrum in Fig. 4.9(b), a distinct feature is that one cross peak is the strongest among all peaks and the cross peaks are asymmetric in strength. In addition, a vertical stripe shows up at the emission photon energy of either HH or LH exciton, as a result of the absorption by continuum states. For a three-level

system, the relative strengths of the diagonal and cross peaks can be estimated from Eqn. (3.18). The diagonal peaks should have amplitudes of μ_{ij}^4 and μ_{ik}^4, while the cross peaks should be equal in strength with amplitude $\mu_{ij}^2\mu_{ik}^2$. If $\mu_{ij} > \mu_{ik}$, then $\mu_{ij}^4 > \mu_{ij}^2\mu_{ik}^2 > \mu_{ik}^4$. Therefore, the cross peaks should never be stronger than the diagonal peaks. This analysis ignores weighting due the finite bandwidth and tuning of the excitation pulses, which can be taken into account by weighting the dipole moments, and does not change the conclusion. Apparently, the asymmetry of cross peaks in experimental data can not be interpreted with a simple approximation of three-level "V" system. Incoherent population relaxation from the upper excited state to the lower one observed in molecular systems [78] can result in unequal cross peaks, however only for a finite waiting time T. This relaxation process is not the case in our experiments, as the asymmetry feature still remains at $T = 0$. The influences of many-body interactions of excitons need to be considered. In the next chapter, a theoretical approach based on the optical Bloch equations is introduced, with phenomenological modifications for semiconductor systems. The manifestations of many-body effects in 2D spectra are then studied numerically and compared to experimental results.

Chapter 5

2D FTS Interpreted with Optical Bloch Equations

The optical Bloch equations (OBE) are commonly employed to interpret the coherent optical response of atomic systems, where the energy structure is well characterized by a few-level model [113]. However, this approach encounters difficulties when it is applied to interacting materials, such as semiconductors, as the dominant many-body interactions alters the coherent dynamics dramatically [26]. To account for that, optical Bloch equations are modified phenomenologically to incorporate many-body terms, including excitation-induced dephasing (EID), excitation-induced shift (EIS), and local field correction (LFC) [6].

In this chapter, the manifestation of many-body effects in 2D spectra is studied with numerical calculations based on the modified optical Bloch equations (MOBE). The theoretical approach of the density matrix formalism and the OBE for a two-level system are first introduced in Section 5.1, followed by the modification with many-body terms. The amplitude 2D spectra are calculated in Section 5.2 and the dominance of many-body effects is demonstrated. The cross peak strength and the presence of continuum absorption in experimental data are represented qualitatively with the inclusion of EID. Full 2D spectra with phase information are calculated in Section 5.3. The lineshape of real part spectrum shows a strong dependence on different many-body mechanisms, making it possible to distinguish the microscopic origin of many-body interactions. In Section 5.4, the manifestation of inhomogeneous broadening as diagonal elongation in

2D spectra is demonstrated with calculations. The inhomogeneity and dephasing rate are determined from the diagonal and cross-diagonal linewidths of experimental spectra. The excitation dependence of broadening for both HH and LH excitons is studied.

5.1   Optical Bloch equations

The quantum physics of a material system can be described by a wavefunction in general, and the time evolution of the system and observable properties are determined by the Schrödinger equation. It is often convenient to employ the density matrix formalism to obtain a statistical description of the quantum system. The density matrix operator is defined as [81]:

$$\rho(t) \equiv |\psi(t)\rangle\langle\psi(t)| \, , \tag{5.1}$$

where $|\psi(t)\rangle$ is the wavefunction of the quantum system. Using the eigenkets $|n\rangle$ of the system as the basis, the wavefunction can be expanded as:

$$|\psi(t)\rangle = \sum_n c_n(t) |n\rangle \, , \tag{5.2}$$

where $c_n(t)$ is the time-dependent coefficient for state n. The density matrix elements $\rho_{nm} = c_n(t)c_m^*(t)$ describe the probability of the system in a certain physical status. The diagonal element $\rho_{nn} = |c_n(t)|^2$ gives the probability of the system in energy eigenstate n, thus it is usually referred as the population density. The off-diagonal element ρ_{nm} $(n \neq m)$ is the interstate coherence between states n and m, which means ρ_{nm} is nonzero only if the system is in a coherent superposition of the two states.

The expectation value of any observable variable in the system can be expressed with the density matrix operator. For example, the expectation value of the polarization operator P is:

$$\langle P \rangle = \langle\psi(t)| P |\psi(t)\rangle = \mathcal{T}r(P\rho(t)) \, , \tag{5.3}$$

where $\mathcal{T}r$ stands for the trace of an operator, i.e., the sum of all diagonal elements. The trace of the density matrix operator $\mathcal{T}r[\rho(t)] = 1$, which is the normalization condition for population density.

For a two-level system with ground state $|1\rangle$ and excited state $|2\rangle$, the wavefunction has the form: $|\psi(t)\rangle = c_1(t)|1\rangle + c_2(t)|2\rangle$. Consequently the density matrix of the system is:

$$\rho = \begin{pmatrix} \rho_{11} & \rho_{12} \\ \rho_{21} & \rho_{22} \end{pmatrix} = \begin{pmatrix} c_1 c_1^* & c_1 c_2^* \\ c_2 c_1^* & c_2 c_2^* \end{pmatrix} , \tag{5.4}$$

where the diagonal element $\rho_{11} = |c_1|^2$ ($\rho_{22} = |c_2|^2$) is the population density in ground (excited) state, whereas ρ_{12} ($\rho_{21} = \rho_{21}^*$) describes the coherence of the system and is proportional to the dipole moment μ_{12} of ground to excited state transition. An ensemble of independent quantum systems can be described by the mixed density matrix, which is formed as a summation of the pure case density matrices weighted by the probability of each individual system.

From the Schrödinger equation of the wavefunction, one can derive the equation of motion for the density matrix in the following form:

$$\dot{\rho} = \frac{1}{i\hbar} [H, \rho] . \tag{5.5}$$

The Hamiltonian of a simple two-level system can be written as:

$$H = H_0 + V = \begin{pmatrix} \hbar\omega_1 & V_{12} \\ V_{21} & \hbar\omega_2 \end{pmatrix} , \tag{5.6}$$

where H_0 is the Hamiltonian of free particles, with eigenenergy $\hbar\omega_1$ and $\hbar\omega_2$ for the two levels. Potential V characterizes the interaction between the applied electric field $E(t)$ and the system. In the dipole approximation of optical excitation, the field is coupled to the system via the dipole transition moment, resulting in a potential with elements $V_{12} = V_{21} = -\mu_{12} E(t)$. In general form, the equation of motion for density matrix reads:

$$\dot{\rho} = \frac{1}{i\hbar} [H_0 + V, \rho] - \text{decays} , \tag{5.7}$$

where "decays" terms are added by hand in this simplistic two-level theory. The relevant decays for the system include spontaneous emission from the excited state to ground (with decay rate γ^{sp}), or to a "reservoir" level (with decay rate γ^{res}) if there is one, and the decay of coherence (with decay rate γ^{ph}). In the quantum theory with second quantization of the applied field, the decay term of spontaneous emission appears intrinsically.

For a closed system, i.e. $\gamma_1^{res} = \gamma_2^{res} = 0$, the conservation of population gives the relation $\rho_{11} + \rho_{22} = 1$, or $\dot{\rho}_{11} = -\dot{\rho}_{22}$. Along with the property $\rho_{21} = \rho_{12}^*$, the density matrix is completely determined by two equations following Eqn. (5.7):

$$\dot{\rho}_{22} = -\gamma^{sp}\rho_{22} + \frac{i}{\hbar}\mu_{12}E\left(\rho_{12} - \rho_{21}\right) , \tag{5.8}$$

$$\dot{\rho}_{12} = -\gamma^{ph}\rho_{12} + i\,\omega_0\,\rho_{12} + \frac{i}{\hbar}\mu_{12}E\left(\rho_{22} - \rho_{11}\right) , \tag{5.9}$$

where the population relaxation with rate γ^{sp} due to decay of spontaneous emission to ground state and the decay of coherence with rate γ^{ph} have been added. μ_{12} is the dipole moment of the transition between the ground and excited states, which has an oscillation frequency $\omega_0 = \omega_2 - \omega_1$. Commonly referred as Bloch equations, Eqn. (5.8) and (5.9) were originally developed by F. Bloch for the description of nuclear magnetic resonance [114] and later extended to problems in coherent optical excitation. In order to account for the strong many-body effects in semiconductors, optical Bloch equations are modified to include phenomenological terms, such as EID, EIS, and LFC [6]:

$$\dot{\rho}_{22} = -\gamma^{sp}\rho_{22} + \frac{i}{\hbar}\mu_{12}\left(E + LP\right)(\rho_{12} - \rho_{21}) , \tag{5.10}$$

$$\dot{\rho}_{12} = -\left(\gamma^{ph} + \gamma'N\rho_{22}\right)\rho_{12} + i(\omega_0 + \omega'N\rho_{22})\rho_{12}$$
$$+ \frac{i}{\hbar}\mu_{12}\left(E + LP\right)(\rho_{22} - \rho_{11}) , \tag{5.11}$$

where N is the number density of oscillators and $P = N\mathcal{T}r(\mu\rho)$ is the polarization. EID is included through the term $\gamma'N\rho_{22}$, which causes the dephasing rate to increase with excitation if $\gamma' > 0$. Excitation-induced narrowing has been discovered in atomic

vapors [115], corresponding to a negative γ'. Similarly, EIS is added through $\omega' N \rho_{22}$, which indicates the resonant frequency increasing with excitation for positive ω'. The local field correction is linear to the polarization, with strength controlled by parameter L. Eqn. (5.10) and (5.11) are called modified optical Bloch equations (MOBE). The linear dependence of the dephasing rate, resonance frequency, and local field on excitation density is a good approximation at the weak power limit. Note that the EID ($\gamma' N \rho_{22} \rho_{12}$) and EIS ($i\omega' N \rho_{22} \rho_{12}$) terms modify the interstate coherence differently with a phase shift introduced by the constant i in Eqn. (5.11). Therefore, phase-sensitive measurements can directly address the distinction between different many-body effects that intensity measurements can not [5, 116].

It is not practical to derive an analytical solution in a general form for the MOBE. Perturbation calculation is usually employed to produce a solution to a certain order in the incident field. For the common initial conditions of $\rho_{22}(0) = 0$ and $\rho_{12}(0) = 0$, the odd powers of population ρ_{22} and the even powers of polarization (interstate coherence) ρ_{12} vanish. Typically, the polarization is calculated to the third-order to represent the nonlinear response of the system in experiments such as FWM. However, it is difficult to characterize excitation-dependent effects with the perturbation calculation, since it is only valid in the weak field limit. Neither the dephasing rate nor the oscillation frequency shows a dependence on the excitation population, even when the polarization is calculated to the fifth-order [117]. There is an essential breakdown of the perturbation theory when excitation-induced effects need to be considered. In order to model these phenomena correctly, MOBE can be numerically solved with the spatial Fourier expansion of the incident fields in a paraxial approximation [117]. This numerical approach is not perturbative, but an approximation in that the spatial expansion of the density matrix elements is truncated to a desired order.

5.2   Amplitude 2D spectra

Numerical calculations of 2D spectra based on MOBE were performed to study the influences of many-body interactions [56, 55]. In this section, the effort is focused on features in the experimental amplitude 2D spectrum in Fig. 4.9(b). As depicted in Fig. 5.1(a), a three-level scheme is used to represent the ground state, excited HH exciton state and LH exciton state in semiconductor quantum wells. The MOBE for the three-level system can be derived in a way similar to that discussed in Section 5.1. The nonlinear polarization is calculated to give a FWM signal as a function of evolution time τ and emission time t. The FWM electric field is displayed as a map on two frequency axes after Fourier transforms with respect to τ and t. The calculated linear absorption spectrum is shown in Fig. 5.1(b), along with an excitation spectrum chosen to match that in Fig. 4.9(a).

The simulated amplitude 2D spectrum is shown in Fig. 5.1(c), where both frequency axes are normalized to the dephasing rate γ^{ph} and in a rotating frame chosen such that the HH exciton resonance has a frequency of 1. The diagonal peaks for the two exciton resonances are reproduced, with cross peaks indicating the coupling through the shared ground state. The two cross peaks have the same strength, which is in between those of the two diagonal peaks, confirming the simple analysis based on a three-level system in Section 4.6. However, this result is quite different from the experimental spectrum in Fig. 4.9(b). The distinct feature of asymmetric cross peak strength and one cross peak being the strongest could be reproduced with the inclusion of many-body effects. Specifically, this feature presents if EID or EIS dominates and there is a difference in how each resonance is affected. To verify this, we include EID that only affects the HH exciton resonance in the calculation and obtain a spectrum in Fig. 5.1(d). Apparently this calculation matches the experimental spectrum better. The diagonal and off-diagonal peaks at the emission frequency of HH exciton are enhanced, leading
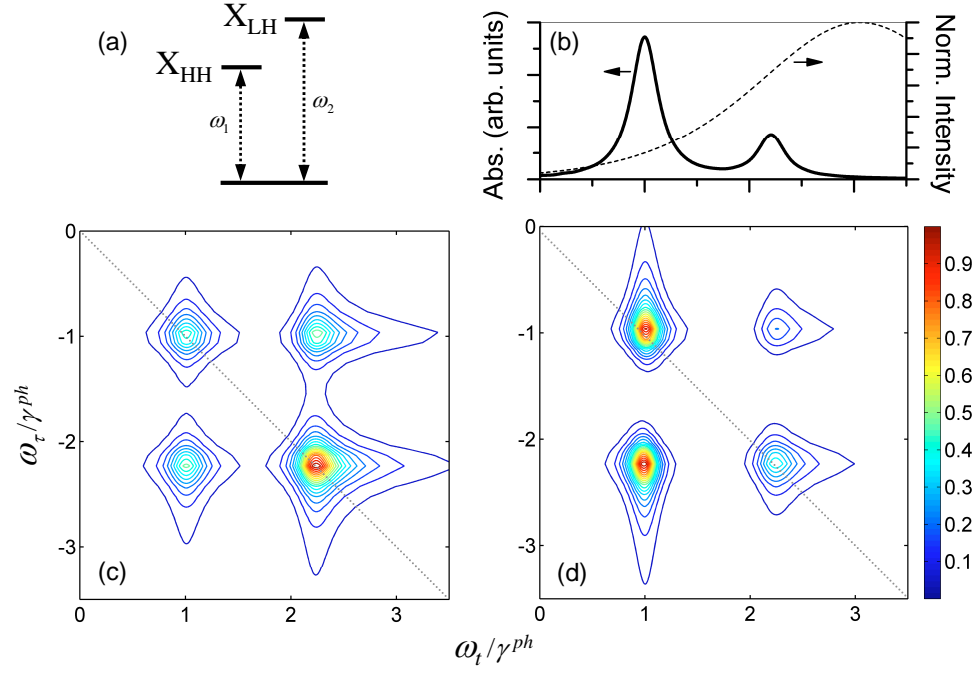
Figure 5.1: Numerical calculations for cross peak strength in amplitude 2D spectrum. (a) The three-level system representing HH and LH excitonic states and ground state; (b) Calculated linear absorption (solid line) and excitation pulse spectrum (dash line); Amplitude 2D spectrum is calculated without any many-body interactions (c), or with EID only affecting HH exciton resonance (d), which results in asymmetric cross peak strength and one cross peak being the strongest. Amplitudes of two spectra are normalized individually and each is represented with 20 contour lines.

to asymmetric cross peaks and a cross peak with the strongest strength.

Another striking feature in Fig. 4.9(b) is the vertical "ridge" at the emission frequency of HH or LH exciton. These ridges are due to the absorption of continuum states. A simple model of the continuum states treats them as a set of inhomogeneously broadened two-level systems. We employ a single strong resonance to model the HH exciton state and a set of 20 weaker resonances with higher dephasing rates for the continuum states, as depicted in Fig. 5.2(a). The calculated linear absorption and excitation spectrum used are shown in Fig. 5.2(b). A diagonal elongation feature, instead of a vertical ridge, presents in the calculation without any many-body effect, as shown in

Fig. 5.2(c). If EID is included to affect the strong resonance only, a 2D spectrum that is qualitatively similar to the experiment is obtained, as shown in Fig. 5.2(d). Since this calculation only models the HH exciton and continuum states, only a single vertical ridge appears, whereas in the experiment two vertical ridges show up, in association with the HH exciton and LH exciton.
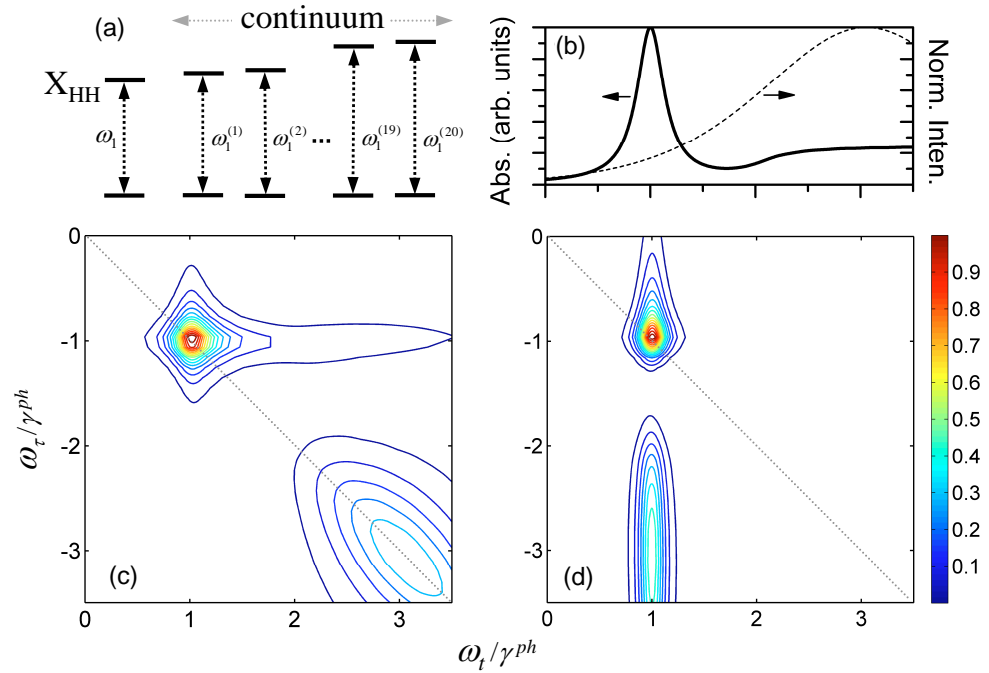

Figure 5.2: Numerical calculations for the amplitude 2D spectrum of HH exciton and continuum states. (a) The system is modeled by a single strong resonance for the HH exciton state and a set of 20 weaker resonances for the continuum states; (b) Calculated linear absorption (solid line) and excitation pulse spectrum (dash line); Amplitude 2D spectrum is calculated without any many-body interactions (c), or with EID included to affect the strong resonance only (d), which results in a vertical ridge feature. Each amplitude spectrum is represented with 20 contour lines.

The goal of the phenomenological calculations is to qualitatively demonstrate the influence of many-body effects on 2D spectra, rather than reproducing experimental data with full details. EID is selected as an instance of many-body effects and the calculation is done without special parameter refinement.

5.3   Full 2D spectra

The dominant influences of many-body interactions on the amplitude 2D spectra of semiconductors have been demonstrated in the previous section. In general, however, different mechanisms of interactions have quite similar manifestations in the amplitude spectrum, thus it is difficult to distinguish these mechanisms. With coherent phase information available, full 2D spectra could give insight into the microscopic nature of many-body interactions.

In simple terms, the imaginary part of a 2D spectrum measures the transient change in the refractive index, whereas the real part gives the resonant absorption of a probe field at emission frequency ω_t, induced at excitation frequency ω_τ [55]. Proper decomposition of a complex 2D spectrum into real and imaginary parts relies on the determination of the global phase, which is made possible by comparing to the spectrally-resolved differential transmission signal from an independent pump-probe measurement, as described in Section 4.5. In Fig. 5.3, the amplitude and real part 2D spectra of a rephasing experiment with colinear-polarized excitation are shown as (c) and (d), respectively, along with the amplitude (a) and real part (b) spectra of the non-rephasing pathway. The excitation spectrum is tuned to the middle of the HH and LH exciton resonances to reduce continuum density. Other experimental conditions are same as those for the spectrum in Fig. 4.9. The non-rephasing experiment was performed by scanning pulse b, instead of scanning pulse a in rephasing measurements. Non-rephasing spectra can provide complementary information to rephasing spectra, such as resolving inhomogeneity and the degree of correlation of inhomogeneity between coupled resonances [72]. In the rephasing amplitude spectrum of Fig. 5.3(c), the strength of cross peaks is still asymmetric, but the lower-left cross peak is no longer the strongest due to the change of tuning. The relative strength of cross peaks to that of diagonal peaks in non-rephasing spectra is weaker than that in rephasing spectra. This difference can be explained with
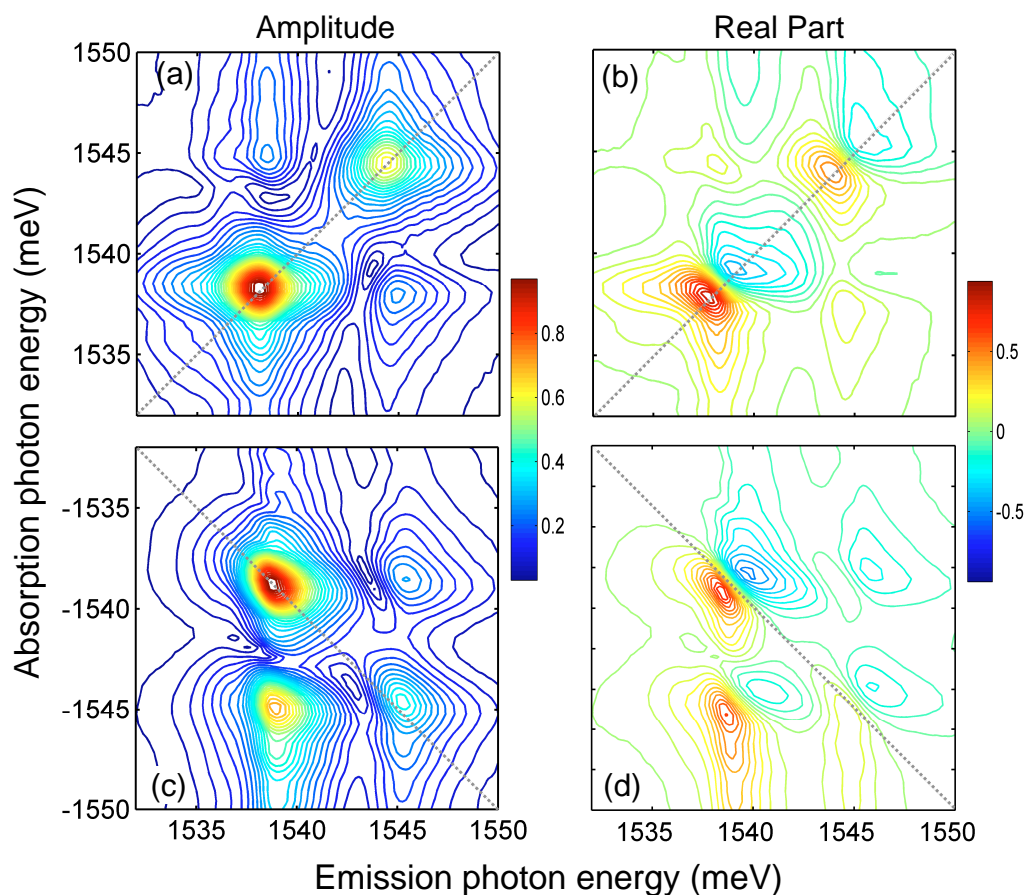
Figure 5.3: Experimental amplitude (a) and real part (b) 2D spectra of non-rephasing pathway, along with the amplitude (c) and real part (d) 2D spectra of rephasing pathway. Both rephasing and non-rephasing spectra are normalized to the respective amplitude and represented with 32 contour lines.

the coherent pathway analysis in Section 3.5. As shown in Fig. 3.9, each diagonal peak corresponds to the contributions from three coherent pathways, whereas each cross peak is due to one pathway in non-rephasing spectra. In contrast, every diagonal or cross peak in rephasing spectra arises from the contributions of two pathways.

Each peak in a real part spectrum presents a strong dispersive (derivative of a peak) feature, either perpendicular to the diagonal in rephasing spectra (Fig. 5.3(d)), or along the diagonal in non-rephasing spectra (Fig. 5.3(b)). The dominance of dispersive
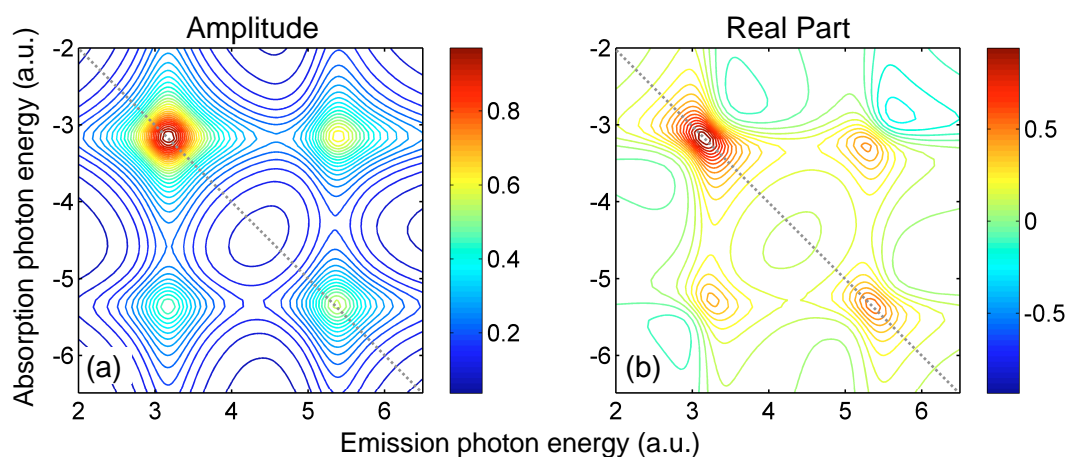
Figure 5.4: Calculated amplitude (a) and real part (b) 2D spectra based on a three-level system, without any many-body effects. Spectra are normalized to the amplitude and represented with 32 contour lines.
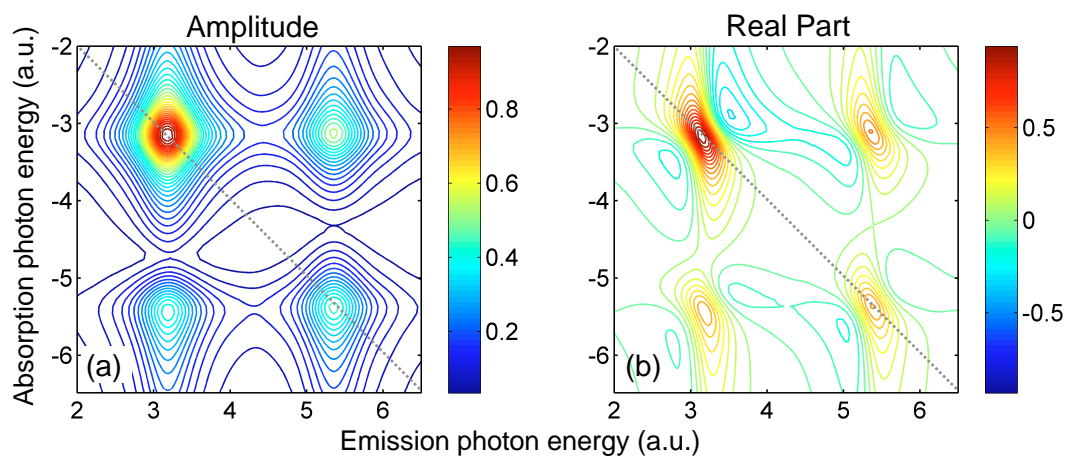
Figure 5.5: Calculated amplitude (a) and real part (b) 2D spectra based on a three-level system, with EID included. Spectra are normalized to the amplitude and represented with 32 contour lines.

lineshapes qualitatively contradicts the prediction of simple optical Bloch equations. As shown in Fig. 5.4, the amplitude (a) and real part (b) 2D spectra are the calculated result of rephasing pathway for the three-level model depicted in Fig. 5.1(a). No many-body effects are included in the calculation. The diagonal peaks display strong absorptive

lineshapes in the real part spectrum. The slightly unequal strength of cross peaks is due to the different dephasing times used for HH and LH exciton resonances in the calculation. With EID included, the calculation produces a real part spectrum shown in Fig. 5.5(b), where both diagonal and off-diagonal peaks are all absorptive. These results are quite different from the measurements. However, the inclusion of EIS in the calculation results in dominant dispersive lineshapes in the real part spectrum, as shown in Fig. 5.6(d). For further comparison, amplitude and real part spectra of non-rephasing pathway are also calculated, which are displayed in Fig. 5.6(a) and (b), respectively. The calculation with EIS qualitatively matches the experimental spectra in both rephasing and non-rephasing pathways. Although the calculation is not aimed to quantitatively determine the phenomenological parameters, they are in reasonable agreement with previous studies [6].

While the real part 2D spectrum presents a distinct change with different many-body effects, the amplitude with EID (Fig. 5.5(a)), or with EIS (Fig. 5.6(c)) has line-shape features similar to that without many-body effects (Fig. 5.4(a)). The phase, rather than the amplitude of 2D spectra, is sensitive to the mechanism of many-body effects. With full signal information presented, 2D FTS approach is a powerful tool for revealing the microscopic origin of many-body interactions in semiconductors. The experimental spectra in Fig. 5.3 were taken at a relative high excitation power, thus the peaks are primarily homogeneously broadened. Consequently no inhomogeneous broadening was considered in all the numerical calculations. It is also possible to make a distinction between EID and EIS in the presence of inhomogeneous broadening, which manifests itself as the diagonal elongation of peaks and does not alter the dispersive or absorptive lineshape.

Although the calculation with EID results in a real part spectrum that does not match the experiment, its contribution can not be simply ruled out. In fact, as a direct manifestation of the EID effect, the peak broadening in 2D spectra has a
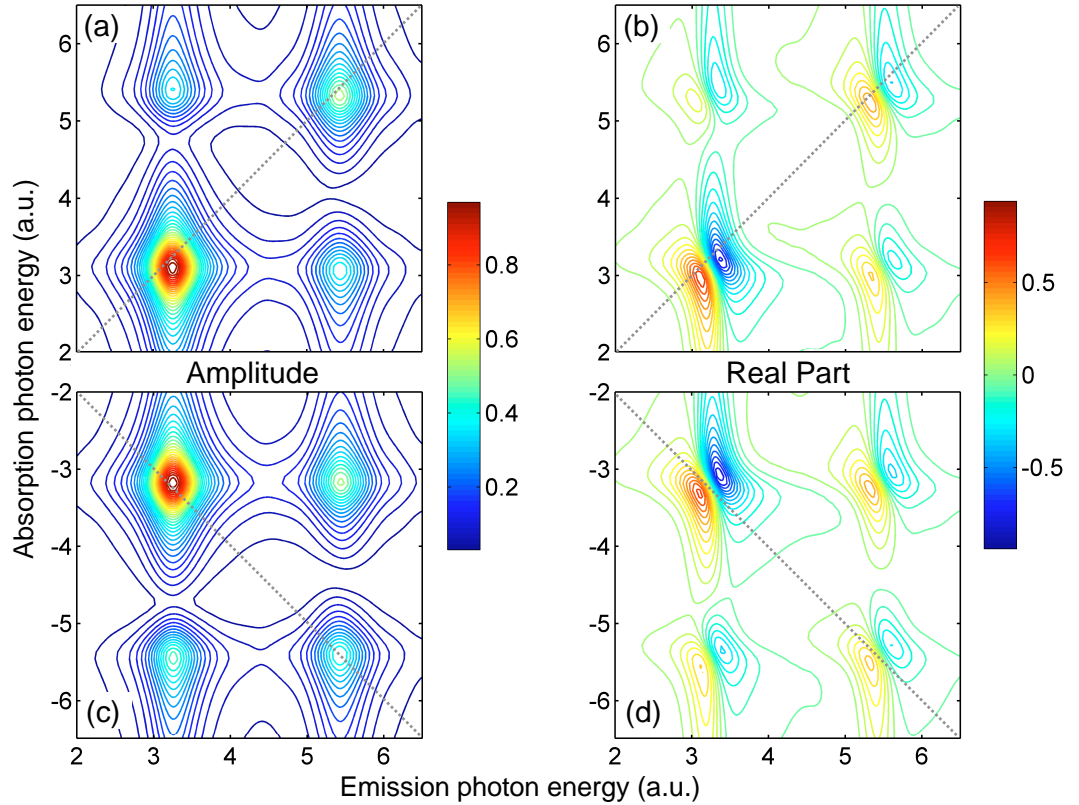
Figure 5.6: Calculated amplitude (a) and real part (b) 2D spectra of non-rephasing pathway, and amplitude (c) and real part (d) 2D spectra of rephasing pathway based on a three-level system, with EIS included. Both rephasing and non-rephasing spectra are normalized to the respective amplitude and represented with 32 contour lines.

distinct dependence on excitation power. The power dependence of homogeneous and inhomogeneous linewidths will be discussed in the following section. In the Green's function approach of microscopic semiconductor theory [118], EID and EIS correspond to the renormalization of the imaginary and real parts of exciton self-energy, respectively, thus they are both present and can not be treated as independent parameters. Possible contributions of the renormalization include band-gap renormalization, screening and correlation terms beyond the Hartree–Fock approximation.

5.4   Determination of homogeneous and inhomogeneous broadening

The linewidth of optical transitions in semiconductors and other materials provides rich information on the structure of electronic states and light-matter interactions. In semiconductor quantum nanostructures at low temperatures, disorder spatially localizes excitons and leads to inhomogeneous broadening [1], whereas phonon induced homogeneous broadening dominates at elevated temperatures. Various nonlinear optical approaches have been utilized to study the broadening in nanostructures, including TI and TR FWM spectroscopies [1, 25]. TI FWM provides the homogeneous width in a simple two-level system, but this is often not true in semiconductors with strong many-body coupling [51]. The temporal width of the photon echo in TR FWM spectroscopy characterizes inhomogeneous broadening. However, echo peak is not well defined due to the interplay between disorder and many-body interactions when disorder-induced broadening is small. In addition, the echo peak can be distorted by beating when more than one resonance is excited [119]. The retrieval of homogeneous width from TI FWM signal with beating requires careful fits to a sophisticated model in general.

2D FTS can be used as a robust tool to determine exciton homogeneous and inhomogeneous linewidths directly, despite the presence of multiple resonances. To demonstrate the manifestation of broadening in 2D spectra, numerical simulations were performed based on the perturbation calculation for a simple two-level system [39]. Inhomogeneous broadening is introduced to the ensemble as a Gaussian distribution [39]:

$$g(\omega) = \frac{1}{\sqrt{2\pi}\,\delta\omega} \exp\big[-\frac{(\omega-\omega_0)^2}{2(\delta\omega)^2}\big]\,, \tag{5.12}$$

where ω_0 is the center of the resonance and $\delta\omega$ is the inhomogeneous width in angular frequency. The homogeneous width is proportional to the dephasing rate γ, as discussed in Section 2.4. 2D spectra are calculated with different $\delta\omega$ and γ. In Fig. 5.7, an amplitude 2D spectrum with γ of $0.3\,\mathrm{ps}^{-1}$ and no inhomogeneous broadening (a) is compared to one with the same γ but an inhomogeneous width δE of $0.7\,\mathrm{meV}$ (b). Here
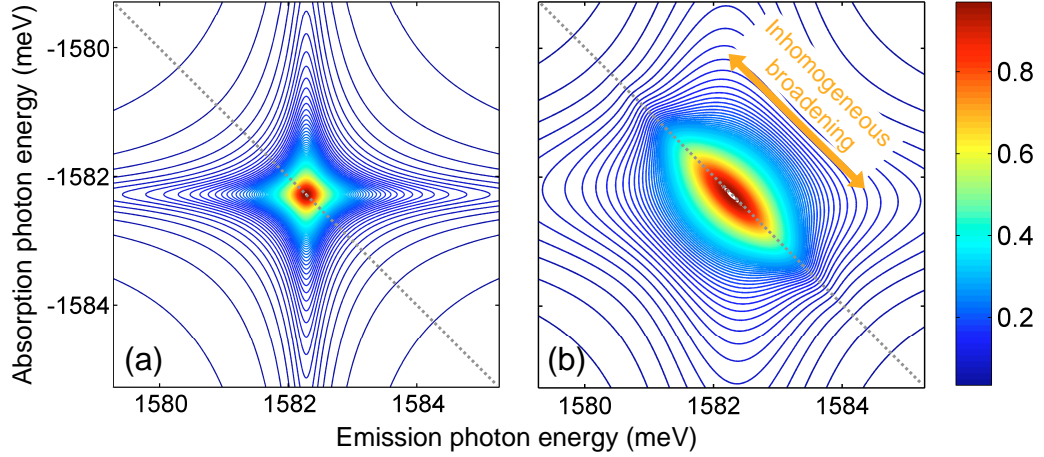
Figure 5.7: Simulated broadening in 2D spectra for a two-level system. (a) Amplitude 2D spectrum with homogeneous width γ of $0.3\,\mathrm{ps}^{-1}$ and no inhomogeneous broadening; (b) Amplitude spectrum with homogeneous width γ of $0.3\,\mathrm{ps}^{-1}$ and inhomogeneous width δE of $0.7\,\mathrm{meV}$.

δE is the full-width at half-maximum (FWHM) in energy defined as $\delta E = 2\sqrt{2\ln 2}\,\hbar\delta\omega$ for convenience. Clearly the inhomogeneous broadening elongates the peak along the diagonal. The diagonal linewidth has a Voigt profile, which corresponds to the convolution of the Gaussian function and the Lorentzian distribution representing homogeneous broadening. The inhomogeneous broadening can be deduced from the Voigt profile by empirical fit [120]. The cross-diagonal width Γ_C (FWHM) and the deduced inhomogeneous width Γ_I (FWHM) in 2D spectra are shown as functions of the dephasing rate γ and inhomogeneous width δE in Fig. 5.8 [121]. From the linewidths along and across diagonal direction, one can retrieve γ and δE directly.

We determine the dephasing rate and inhomogeneous broadening of HH and LH excitons from experimental 2D spectra. The sample under study is a multiple quantum well structure containing four periods of $10\,\mathrm{nm}$ GaAs well and $10\,\mathrm{nm}$ $\mathrm{Al}_{0.3}\mathrm{Ga}_{0.7}\mathrm{As}$ barrier cooled below $10\,\mathrm{K}$. The amplitude 2D spectrum of rephasing pathway is used to obtain δE and γ. Real or imaginary part spectrum can also be employed for linewidth
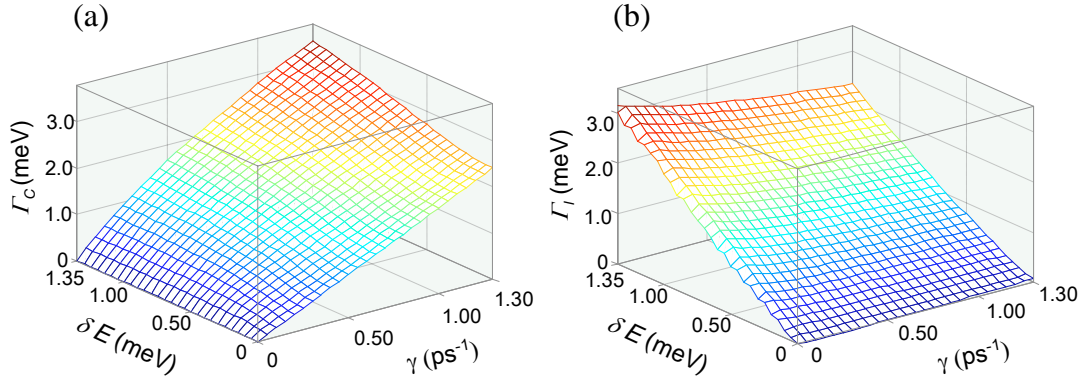
(a)

(b)

Figure 5.8: Simulation result of the cross-diagonal width Γ_C (FWHM) (a) and the deduced inhomogeneous width Γ_I (FWHM) (b) in 2D spectra as functions of dephasing rate γ and inhomogeneous width δE.

analysis, with the advantage of resolution improvement when congested spectra are present. Fig. 5.9 shows the linewidths of HH and LH excitons from experiments of different excitation power within the weak excitation regime [121]. From the homogeneous widths we find the dephasing time is $4.5\,\mathrm{ps}$ for HH exciton and $3.8\,\mathrm{ps}$ for LH exciton at $200\,\mu\mathrm{W}$. The homogeneous width of HH or LH exciton increases with power, in good agreement with early TI FWM experiments [45]. The inhomogeneous broadening of HH and LH excitons at $200\,\mu\mathrm{W}$ are $0.54\,\mathrm{meV}$ and $0.40\,\mathrm{meV}$, respectively. The larger inhomogeneous width of the HH exciton is possibly due to the localization by disorder, since the HH exciton is more likely localized with a lower mobility compared to LH exciton. If the disorder is of short range compared to the exciton diameter, the smaller inhomogeneous width of LH exciton can be the result of a more effective averaging of inhomogeneity over LH excitons [122], as the Bohr radius of LH exciton is bigger than that of the HH exciton. The inhomogeneous broadening also shows an excitation dependence, which demands an understanding of the interplay between disorder and many-body interactions. Interactions between HH exciton continuum and LH excitons should be considered due to the spectral overlap, thus the broadening of LH exciton
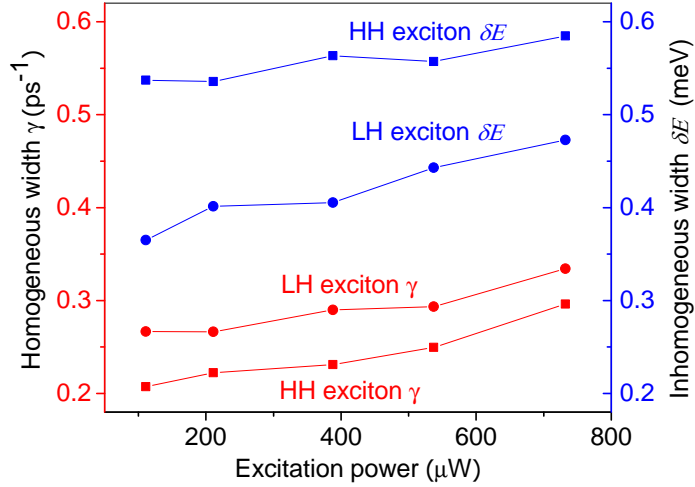
Figure 5.9: Excitation power dependence of homogeneous and inhomogeneous linewidths for HH and LH excitons obtained from experimental 2D spectra.

is more complicated. The coupling of HH and LH excitons also affects the linewidth of both resonances. Such problems can be avoided by reducing the bandwidth of laser pulses and exciting the HH exciton resonance only. It is possible to observe the difference in homogeneous broadening between bound and unbound excitons in 2D spectra. Compared to bound excitons, the decoherence of unbound excitons is faster due to stronger scattering processes, thus results in a broader homogeneous linewidth. Consequently, the cross-diagonal width on the higher energy side of the resonance peak is larger than that on the lower energy side, leading to an asymmetric elongation along the diagonal.

In addition to the linewidth study with 2D spectra in rephasing pathway, the non-rephasing spectra can also be employed for complementary information on broadening. In microscopic calculations of 2D spectra with the inclusion of many-body interactions of HH and LH excitons as well as biexcitons [119], inhomogeneous broadening demonstrates different behaviors in non-rephasing and rephasing pathways, making it possible to separate disorder-induced broadening. Experimental studies towards this goal are still on the way.

Chapter 6

2D FTS Interpreted with Microscopic Semiconductor Theory

In the previous chapter, we reproduced the qualitative features of 2D spectra in numerical calculations based on the modified optical Bloch equations with the inclusion of phenomenological many-body effects. While phenomenological few-level models are widely employed due to the simple formalisms and thus the relatively easy implementation in practice, there has been significant progress in the development of fundamental microscopic theory for semiconductors [25, 118, 123, 124, 125, 126]. In microscopic theories, an optically-excited semiconductor is treated as a quantum many-body system of interacting electrons and holes. Usually only the electrons in the lowest conduction band and holes in the highest valence band are considered. The Coulomb interactions profoundly influencing the coherent nonlinear response are taken into account in this picture. Compared to a few-level model, the Coulomb interactions renormalize the electron and hole energies and produce excitons. The interaction strength between the radiation field and the semiconductor is also renormalized [2]. Different microscopic approaches in terms of density matrices as well as non-equilibrium Green's functions have been developed. Within the density matrix approach, the Coulomb interaction leads to an infinite hierarchy of higher order of density matrices, which can be truncated using either correlation expansion or dynamics-controlled truncation scheme [124]. Within the Green's function approach, the problem of an infinite hierarchy is deferred to constructing the self-energy. EID and EIS in the phenomenological model correspond to the

renormalization of the imaginary and real parts of the exciton self-energy, respectively, therefore they are not independent parameters in the microscopic theory. The relation between phenomenological few-level models and microscopic semiconductor theories has been discussed [127].

With the rich information of carrier dynamics and many-body interactions preserved, 2D FTS provides a stringent test of theoretical models and gives insight into the microscopic nature of exciton correlations in semiconductors. The 2D spectra of excitonic resonances are sensitive to excitation conditions, which include the spectrum, intensity, and polarization of the incident laser pulses. In the 2D FTS experiments discussed in the previous chapters, we have used colinear-polarized excitation pulses, which is experimentally the most straightforward method but not the simplest for interpretation. The earlier studies also only used a single tuning and power of the incident pulses, with the latter corresponding to a relatively high excitation density in the sample. In this chapter, we study the dependence of 2D spectra on the excitation conditions, particularly the polarization of excitation beams. Cocircular-polarized excitation provides the simplest case for isolating many-body effects as they are responsible for the coupling between the HH and LH exciton resonances. Cross-linear-polarized excitation suppresses the exciton resonances and reveals contributions from biexcitons. Experimental results show a strong dependence of 2D spectra on the polarization of excitation beams, and the dominant influence of many-body interactions in each case. These results are compared to calculations based on the microscopic theory, with qualitative agreement.

6.1   General formalism of the microscopic semiconductor theory

For the numerical studies of 2D spectra, we use a general formalism of the microscopic semiconductor theory, which has been employed to investigate the effects of carrier correlations on the excitonic optical response of semiconductors [125]. As a real-

space approach, this formalism is particularly suitable for semiconductor systems with disorders [25]. The Hamiltonian of the system can be written in the following form:

$$H = H_0 + H_C + H_I \, , \tag{6.1}$$

where H_0 is the free-particle Hamiltonian, H_C is due to the Coulomb interaction, and H_I is from the interaction of the system with the electric field of incident light.

The free-particle Hamiltonian reads:

$$H_0 = \sum_{ij\,c} T_{ij}^c \, a_i^{c+} a_j^c + \sum_{ij\,v} T_{ij}^v \, a_i^{v+} a_j^v \, , \tag{6.2}$$

where i and j are indices to real-space sites, and c (v) means the conduction (valence) band. a_i^{c+} (a_i^c) creates (destroys) an electron in conduction band at site i, and a_i^{v+} (a_i^v) creates (destroys) a hole in valence band at site i. The diagonal terms of the T matrices give the site electronic energies while the off-diagonal terms define the couplings between sites.

The Coulomb Hamiltonian H_C has the form:

$$H_C = \frac{1}{2} \sum_{ij\,cv\,c'v'} (a_i^{c'+}a_i^{c'} - a_i^{v'+}a_i^{v'})V_{ij}(a_j^{c+}a_j^c - a_j^{v+}a_j^v) \, , \tag{6.3}$$

where V_{ij} is the Coulomb potential between particles at site i and j. The dipole interaction of the system with a classical electric field $\mathbf{E}(t)$ is:

$$H_I = -\mathbf{E}(t) \cdot \mathbf{P} = -\mathbf{E}(t) \cdot \sum_{ijvc} (\boldsymbol{\mu}_{ij}^{vc} \, a_i^v \, a_j^c + (\boldsymbol{\mu}_{ij}^{vc})^* \, a_j^{c+} \, a_i^{v+}) \, , \tag{6.4}$$

where $\mathbf{P}$ is the optical interband polarization, and $\boldsymbol{\mu}$ is the dipole matrix for optical transition between valence and conduction bands.

The interband coherence, $p_{12}^{v_1 c_2} = \langle a_1^{v_1} a_2^{c_2} \rangle$, is characterized by the equation of

motion, with the total Hamiltonian plugged in, as follows:

$$
\begin{aligned}
-i\,\frac{\partial p_{12}^{v_1 c_2}}{\partial t} = \; & -\; \sum_j T_{2j}^c\, p_{1j}^{v_1 c_2} - \sum_i T_{i1}^v\, p_{i2}^{v_1 c_2} + V_{12}\, p_{12}^{v_1 c_2} \\
& -\; \mathbf{E}(t)\cdot[(\boldsymbol{\mu}_{12}^{v_1 c_2})^* - \sum_{jc}(\boldsymbol{\mu}_{1j}^{v_1 c})^*\, f_{j2}^{cc_2} - \sum_{iv}(\boldsymbol{\mu}_{i2}^{vc_2})^*\, f_{i1}^{vv_1}] \\
& +\; \sum_{kv_k}[V_{k1}\langle a_k^{v_k} a_1^{v_1} a_k^{v_k+} a_2^{c_2}\rangle - V_{2k}\langle a_1^{v_1} a_k^{v_k} a_2^{c_2} a_k^{v_k+}\rangle] \\
& +\; \sum_{kc_k}[V_{k1}\langle a_k^{c_k+} a_1^{v_1} a_k^{c_k} a_2^{c_2}\rangle - V_{2k}\langle a_1^{v_1} a_k^{c_k+} a_2^{c_2} a_k^{c_k}\rangle]\,. \qquad (6.5)
\end{aligned}
$$

Here the electron and hole populations and intraband coherences are defined as $f_{j2}^{cc_2} = \langle a_j^{c+} a_2^{c_2}\rangle$ and $f_{1i}^{v_1 v} = \langle a_1^{v_1+} a_i^{v}\rangle$, respectively. The four-point functions represent the first step of the infinite hierarchy of many-body correlations induced by Coulomb interaction.

For simplification, we consider the coherent limit in which dephasing processes due to scattering with other quasi-particles are neglected. Besides, relatively weak excitation is assumed and terms contributing to the optical response are only included to the third-order in the optical field. Within these assumptions the electron and hole populations and coherences are no longer independent but can be expressed by the interband coherence as:

$$
\sum_{av_a} p_{a2}^{v_a c_2}(p_{a1}^{v_a c_1})^* = f_{12}^{c_1 c_2}\,, \qquad (6.6)
$$

and

$$
\sum_{ac_a} p_{1a}^{v_1 c_a}(p_{2a}^{v_2 c_a})^* = f_{12}^{v_1 v_2}\,. \qquad (6.7)
$$

The optical response up to $\chi^{(3)}$ can be expressed with two transition-type quantities: the interband coherences $p_{12}^{v_1 c_2}$ related to single-exciton and $\sigma_{1234}^{v_1 v c c_2} = \langle a_1^{v_1} a_2^{v} a_3^{c} a_4^{c_2}\rangle$ describing two-exciton excitations. In order to study the pure correlation effects beyond the time-dependent Hartree–Fock approximation, the uncorrelated parts can be separated from the four-point quantities by defining: $\bar{\sigma}_{1234}^{v_1 v c c_2} = \sigma_{1234}^{v_1 v c c_2} - p_{14}^{v_1 c_2} p_{23}^{vc} + p_{13}^{v_1 c} p_{24}^{vc_2}$. This procedure results in closed equations of motion for the single-exciton amplitude p_{12}^{vc} and the two-exciton amplitude $B_{1324}^{v_1 c v c_2} \equiv -\bar{\sigma}_{1234}^{v_1 v c c_2}$ that completely determine the optical response within the coherent $\chi^{(3)}$-limit.

The equation of motion for p becomes:

$$-i\,\frac{\partial p_{12}^{vc}}{\partial t} = -\sum_j T_{2j}^c\, p_{1j}^{vc} - \sum_i T_{i1}^v\, p_{i2}^{vc} + V_{12}\, p_{12}^{vc}$$

$$+ \sum_{abv'c'} (V_{a2} - V_{a1} - V_{b2} + V_{b1})(p_{ba}^{v'c'})^* [\, p_{b2}^{v'c'} p_{1a}^{vc} - p_{ba}^{v'c'} p_{12}^{vc} - B_{ba12}^{v'c'vc} \,]$$

$$+ \; \mathbf{E}(t) \cdot [\, (\boldsymbol{\mu}_{12}^{vc})^* - \sum_{abv'c'} ((\boldsymbol{\mu}_{1b}^{vc'})^*(p_{ab}^{v'c'})^* p_{a2}^{v'c} + (\boldsymbol{\mu}_{b2}^{v'c})^*(p_{ba}^{v'c'})^* p_{1a}^{vc'}) \,] \;, \quad (6.8)$$

and the equation of motion for B is:

$$-i\,\frac{\partial B_{ba12}^{v'c'vc}}{\partial t} = -\sum_i (\, T_{2i}^c\, B_{ba1i}^{v'c'vc} + T_{i1}^v\, B_{bai2}^{v'c'vc} + T_{ai}^c\, B_{bi12}^{v'c'vc} + T_{ib}^v\, B_{ia12}^{v'c'vc} \,)$$

$$+ (V_{ba} + V_{b2} + V_{1a} + V_{12} - V_{b1} - V_{a2})\, B_{ba12}^{v'c'vc}$$

$$- (V_{ba} + V_{12} - V_{b1} - V_{a2})\, p_{1a}^{vc'} p_{b2}^{v'c} + (V_{1a} + V_{b2} - V_{b1} - V_{a2})\, p_{ba}^{v'c'} p_{12}^{vc} \;.$$

$$(6.9)$$

The total interband polarization $\mathbf{P}$ measured in an experiment is:

$$\mathbf{P} = \sum_{ijvc} \boldsymbol{\mu}_{ij}^{vc}\, p_{ij}^{vc} \;, \tag{6.10}$$

from which the electric field of the emitted FWM signal can be obtained with Eqn. (3.16).

6.2   One-dimensional tight-binding model

To keep the complexity of numerical computations within tractable limits, a one-dimensional tight-binding model is commonly used to simulate the semiconductor band structure [125]. Quantitative agreements between calculations and experiments are not expected with this model, however, it has qualitatively produced important signatures in different types of experiments in the $\chi^{(3)}$-limit, such as pump-probe, transient FWM, and coherent excitation spectroscopy [25, 34, 98, 125, 128, 129].

In the one-dimensional tight-binding model, it is assumed that N particles are spatially localized to form a one-dimensional chain. The site positions are labeled as ia,

where $i = 1, 2, \ldots, N$ is the index of sites, and a is the spatial separation between two neighbor sites, as depicted in Fig. 6.1 [130]. The energetic levels of the electron, HH, and LH at site i are denoted as ε_i^c, ε_i^h, and ε_i^l, respectively. The coupling between localized electrons in two close neighbor sites i and j is described by J_{ij}^c, and that between HHs (LHs) is J_{ij}^h (J_{ij}^l). The interband coherence between sites i and j is given by p_{ij}. $\boldsymbol{\mu}_i^h E$ ($\boldsymbol{\mu}_i^l E$) is the optical transition strength from the HH (LH) level to the electron level in site i, induced by an electric field E. The energy separation of the electron and HH levels, E_0, and the band width due to the coupling, determine the energy gap E_g at the Γ-point for the given semiconductor material. The quantum well system is modeled with the introduction of LH levels, which are below the HH levels with an energy splitting provided by the linear absorption spectrum.
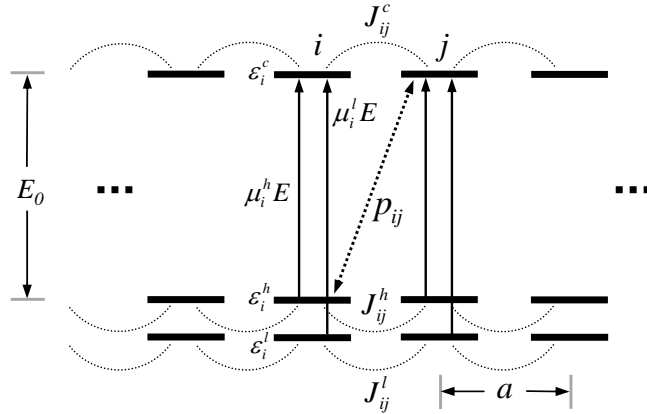

Figure 6.1: The one-dimensional tight-binding model for semiconductor quantum wells [130].

In the tight-binding approximation, the Hamiltonian matrices T^c and T^v in Eqn. (6.2) are defined with diagonal elements $T_{ii}^c = \varepsilon_i^c$ and $T_{ii}^v = \varepsilon_i^{h(l)}$, off-diagonal elements $T_{ij}^c = J_{ij}^c$ and $T_{ij}^v = J_{ij}^{h(l)}$ for $|i - j| = 1$, and zero for all other off-diagonal elements. The Coulomb potential has the form [125]:

$$V_{ij} = U_0 \frac{a}{|i - j|\, a + a_0} \, , \tag{6.11}$$

where a is the site spacing constant, a_0 regularizes the potential in order to have a finite exciton binding energy, and U_0 characterizes the strength of Coulomb interactions.

Based on the one-dimensional tight-binding model, 2D spectra of different excitation polarizations were calculated with 40 sites [57]. Realistic material parameters, such as effective masses, dipole matrix elements, resonance centers, and oscillator strengths come from the experimental linear absorption spectrum. The experimental conditions, including laser pulse width, tuning, excitation polarization and pulse ordering, are incorporated into the model. The dephasing times of excitons and biexcitons are taken as phenomenological parameters and adjusted to match the experimental spectra. Unlike the phenomenological few-level model discussed in Chapter 5, the many-body contributions are intrinsic in the microscopic theory, and their relative strengths cannot be adjusted. Details of the microscopic theory and numerical calculations have been discussed in reference [130].

6.3   Excitation dependence of 2D spectra

In this section, we demonstrate the dependence of 2D spectra on the tuning and power of the excitation pulses. First of all, the power dependence of FWM signal is studied to determine the excitation density for 2D experiments. The TI FWM intensity is measured as a function of the excitation pulse power, with τ corresponding to the peak of the signal, T equal to 100 fs, and the laser tuned to the LH exciton resonance. Similar to Fig. 4.8, the signal intensity is shown as a function of the pulse power for excitations of colinear, cocircular, and cross-linear polarization in Fig. 6.2. The FWM intensity in all cases increases approximately as the cube of the excitation power, until saturation starts at about 1 mW, which corresponds to an excitation density about 10^{10} excitons/well/cm^2.

In Fig. 6.3, real part 2D spectra of the rephasing pathway with colinear-polarized
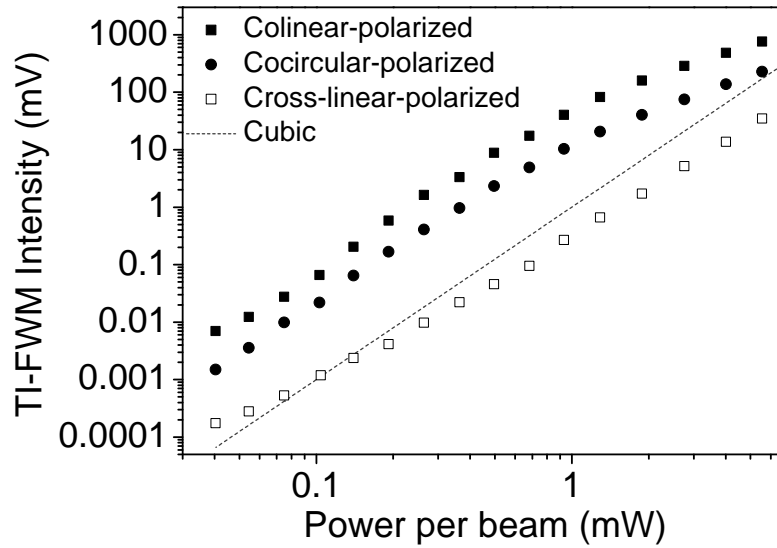
Figure 6.2: Excitation power dependence of TI FWM intensity for excitations of colinear (solid square), cocircular (solid circle), and cross-linear (hollow square) polarization.

excitation are depicted for four different laser tunings. For each tuning, the spectra at two excitation powers, $0.8\,\mathrm{mW}$ and $1.6\,\mathrm{mW}$, are shown. The linear absorption spectrum and respective excitation spectrum are displayed above each pair of spectra. The lowest tuning corresponds to the peak of the laser spectrum coinciding with that of the HH exciton resonance. From there it is increased to be halfway between the HH and LH excitons, coincident with the LH exciton, and finally several meV above the LH exciton, which puts it well into the continuum of unbound electron-hole pairs. The laser bandwidth is sufficient so that both exciton resonances and unbound electron-hole pairs are excited in all four cases. Clearly, the relative peak strengths vary with tuning, as a relatively straightforward effect caused by the changing excitation density due to spectral overlap.

All of the 2D spectra in Fig. 6.3 exhibit some common features. Similar to the amplitude 2D spectra discussed in Section 4.6, two diagonal peaks appear at the photon energies of the HH and LH excitons, with two off-diagonal peaks indicating
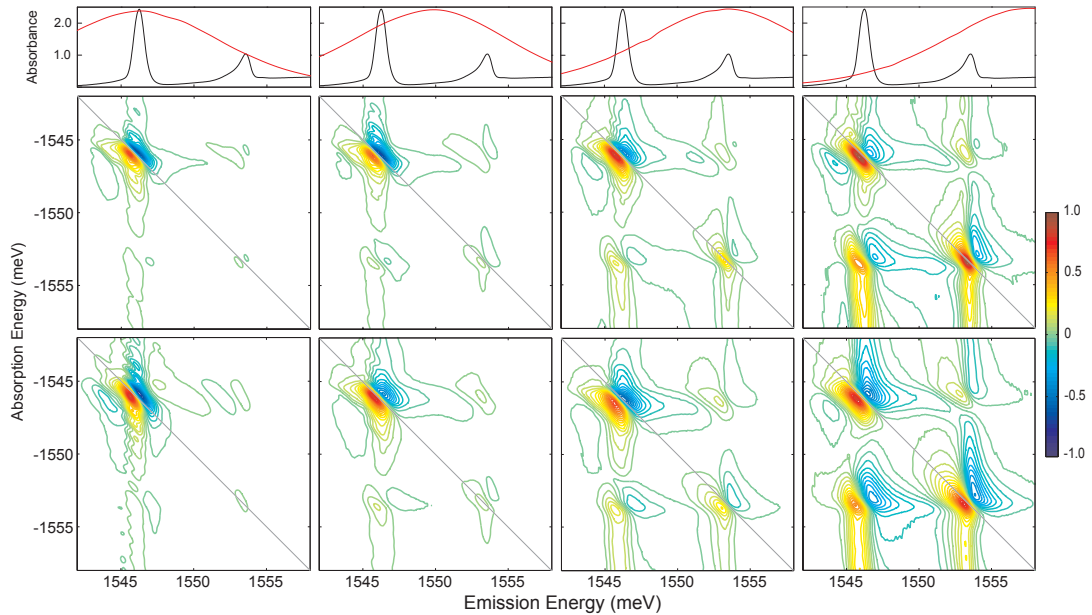
Figure 6.3: Experimental real part 2D spectra with colinear-polarized excitation, rephasing time ordering and $T = 200\,\text{fs}$. For each tuning, the lower spectrum is taken at twice the power of the upper one. The laser spectrum is overlaid on the linear absorption spectrum above the respective pair of spectra [57].

the resonant coupling. Cross peaks are expected for colinear-polarized excitation as the shared electronic state in the conduction band results in resonant coupling. For higher laser tunings, a vertical stripe also arises at the emission photon energies of both excitons, as a result of the excitation of unbound electron-hole pairs, or continuum. With the calculations based on the modified optical Bloch equations in Chapter 5, we have demonstrated that the continuum states manifest as a diagonal feature in 2D spectra, rather than a vertical stripe, if they act as a set of inhomogeneously broadened transitions. The vertical stripes occur because free pairs strongly couple to the excitonic resonances, resulting in a dominant signal at the excitons [51].

Microscopic calculations were performed by our collaborators in Philipps Universität, Marburg, for 2D spectra with colinear-polarized excitation at different tunings corresponding to those used in Fig. 6.3 [57]. As shown in Fig. 6.4, the experimental

real part spectra are qualitatively reproduced, including the spectral structures, the dispersive lineshapes, and the tuning dependence. The good agreement indicates that the theory well captures the many-body processes. Since the theory is only valid in the weak excitation limit, the dispersive feature in the experimental spectra for excitation at the HH exciton and for higher intensity must be the result of effects beyond third-order in the incident electric field. The relative strengths of peaks depend strongly on the dephasing rates of the excitonic resonances.
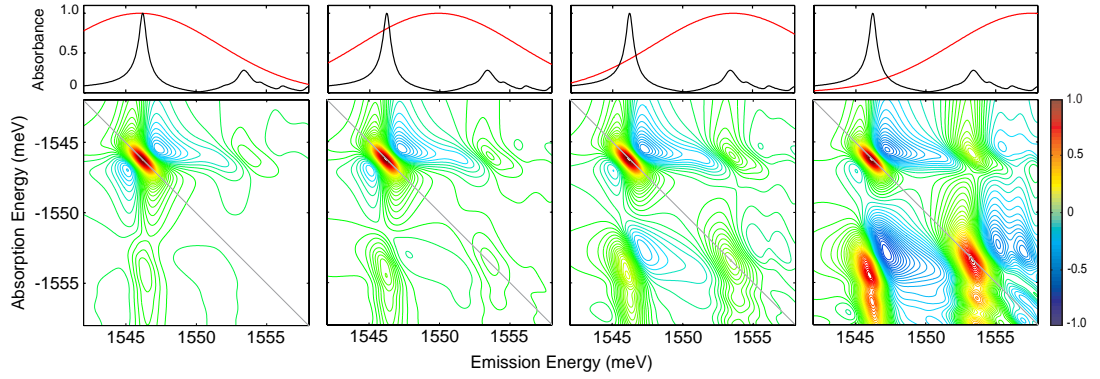

Figure 6.4: Real part 2D spectra of colinear-polarized excitation calculated with the microscopic semiconductor theory, at different tunings. $T = 200\,\text{fs}$, and an inhomogeneous broadening of $0.7\,\text{meV}$ is applied. The calculated linear absorption spectrum overlaid with the laser spectrum is shown at the top. Calculations were performed by collaborators [57].

6.4   2D spectra with cocircular-polarized excitation

Although colinear-polarized excitation is the most straightforward experimentally, it is not optimal for revealing many-body contributions. Cocircular-polarized excitation, on the other hand, provides an immediate and striking demonstration of the dominant role that many-body processes play in semiconductors. Based on the selection rule of optical transitions between the HH and LH valence bands and the conduction band, as depicted in Fig. 2.3(b), no coupling between HH and LH excitons would be
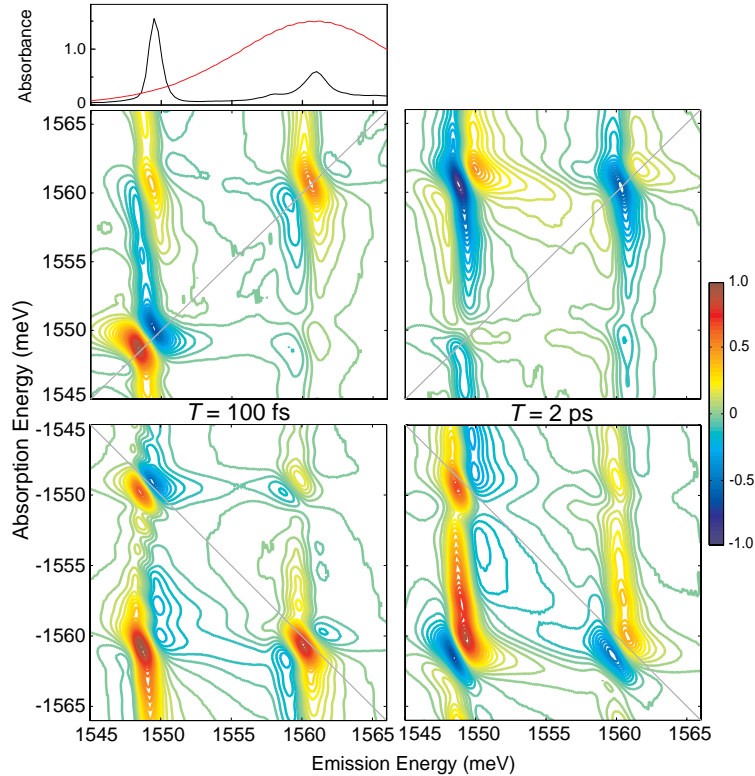
Figure 6.5: Experimental real part 2D spectra with cocircular-polarized excitation. Both rephasing (Bottom) and non-rephasing (Middle) are shown for $T = 100\,\mathrm{fs}$ (Left) and $T = 2\,\mathrm{ps}$ (Right). The linear absorption and laser spectrum are shown at the top [57].

expected for cocircular-polarized excitation. Previous FWM [131], spectrally-resolved differential transmission [132], and coherent excitation spectroscopy [129] studies have shown that indeed coupling does occur in cocircular-polarized excitation, attributing it to many-body correlations. Experimental 2D spectra of both rephasing and non-rephasing pathways with cocircular-polarized excitation are shown in Fig. 6.5. A laser tuning overlapping the LH exciton resonance is used, with $T = 100\,\mathrm{fs}$ and $2\,\mathrm{ps}$. The clear appearance of cross peaks between the HH and LH excitons in both pathways, as a strong evidence of the many-body coupling, confirms the conclusion of the earlier studies.

To check the manifestation of many-body effects in 2D spectra, microscopic cal-

culations were performed with different levels of Coulomb interactions. As shown in Fig. 6.6, the real part 2D spectra with cocircular-polarized excitation are calculated with contributions of Pauli blocking only, within the Hartree–Fock approximation, and with higher-order Coulomb correlations, respectively. Both rephasing and non-rephasing pathways are shown, with $T = 100\,\mathrm{fs}$. If only Pauli blocking terms are included, the Coulomb interaction is neglected except for the part that contributes to exciton formation, and the optical nonlinearity arises from the saturation of the resonances by
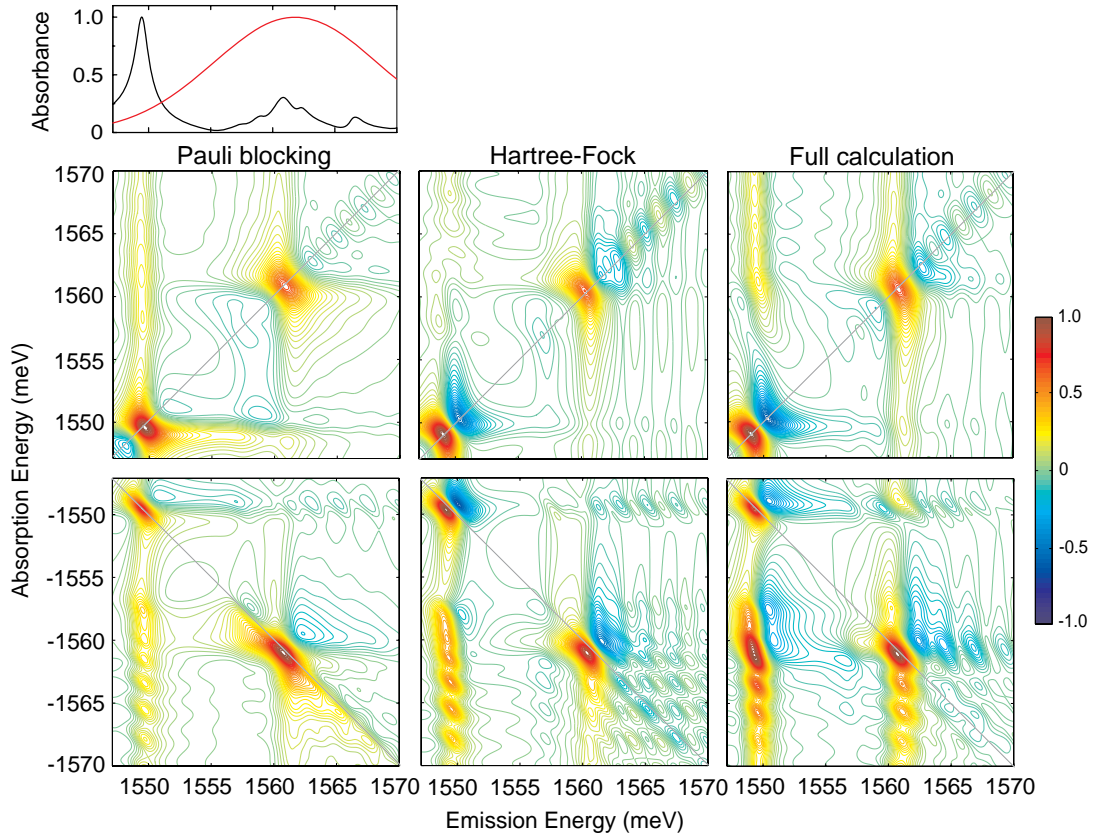
Figure 6.6: Real part 2D spectra of cocircular-polarized excitation calculated with the microscopic theory by collaborators [57]. Both rephasing (Bottom) and non-rephasing (Middle) cases are shown with only Pauli blocking included (Left), within the Hartree–Fock approximation (Center), and for the full calculation including all correlation terms (Right) for cocircular-polarized excitation with $T = 100\,\mathrm{fs}$. The calculated linear absorption and laser spectrum are shown at the top.

phase-space filling. In this case, no cross peaks occur, and the continuum states appear on the diagonal. The two diagonal peaks from HH and LH excitons present a strong absorptive feature in both rephasing and non-rephasing pathways. When the Coulomb interaction is included, but only in the Hartree–Fock approximation, weak cross peaks appear, but the relative strengths of the cross peaks and diagonal peaks do not agree with the experiment. In addition, the continuum states display cross peaks, but no vertical feature, as occurs in the experiment. Only the full calculation, including Coulomb correlations beyond the Hartree–Fock approximation, provides good agreement with the experiment. The relative strengths of peaks are reproduced, with the cross peak at the LH exciton absorption photon energy and HH exciton emission photon energy dominating. Furthermore, the continuum exhibits vertical stripes at the exciton emission photon energies. Therefore, we conclude that the higher-order exciton correlations beyond the Hartree–Fock limit play dominant roles in the nonlinear optical response of semiconductors.

Enhancement of low-energy resonances can also occur because of incoherent relaxation. The incoherent relaxation can be studied by varying T, as it occurs when the system is in a population state [78]. In the 2D spectra of $T = 100\,\mathrm{fs}$ and $2\,\mathrm{ps}$ shown Fig. 6.5, there is some limited strengthening of the emission at the HH exciton emission photon energy with T, thus the dominance of the HH exciton emission is not caused by incoherent relaxation. The microscopic theory is within the coherent limit, so incoherent relaxation is not considered. The good agreement provided by the coherent limit further supports the conclusion that incoherent relaxation is not significant for spectra taken with T of a few hundred femtoseconds.

6.5   2D spectra with cross-linear-polarized excitation

As the bound state of two interacting excitons, the biexciton has significant influences on the optical properties of semiconductor quantum wells at low temperatures. Prominent evidences include the presence of beats with a frequency corresponding to the biexciton binding energy for "negative" delays [4] or mediated by strong inhomogeneous broadening [133]. With a small binding energy of a few meV in quantum wells, biexcitons are often masked by inhomogeneous broadening due to the disorder in the system, making it difficult to isolate their contributions in FWM signal.
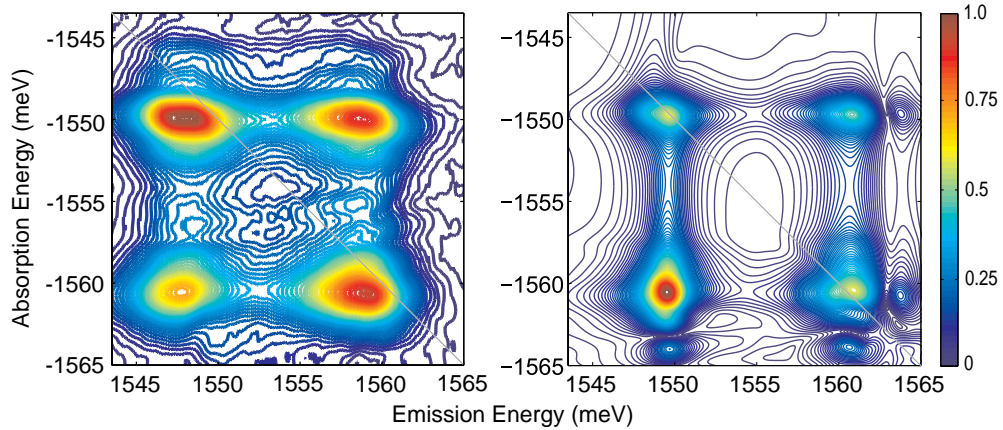

Figure 6.7: Experimental (left) and calculated (right) amplitude 2D spectra with cross-linear-polarized excitation, where the polarization of the first beam is perpendicular to that of the rest. $T = 100\,\mathrm{fs}$ and a higher excitation power is used [57].

Biexcitonic effects are more apparent in experiments with cross-linear-polarized excitation, where the polarization of the first beam is perpendicular to that of the rest, since many-body interactions arising from single exciton resonances are suppressed in this case. Fig. 6.7(a) shows an experimental amplitude 2D spectrum of cross-linear-polarized excitation, with $T = 100\,\mathrm{fs}$ and a higher excitation power because of the reduced signal strength in this polarization configuration. Currently only the amplitude spectrum is available, since the spectrally-resolved differential transmission mea-

surement for the determination of the global phase in 2D spectra is no longer valid for cross-linear excitation. Similar to the 2D spectrum of colinear-polarized excitation, there are two diagonal peaks and two cross peaks in Fig. 6.7(a), however, all these peaks are dominated by a horizontal elongation. This feature is due to the arising of biexciton peaks, which are red-shifted by about 2 meV compared to the single-exciton peaks. The manifestation of biexcitons is verified by the calculated 2D spectrum for cross-linear-polarized excitation, as depicted in Fig. 6.7(b), where the horizontal elongation is not as significant as that in the experimental spectrum without optimizing parameters in the calculation. The elongation of the peaks corresponds to the emission at the exciton-to-biexciton transition. This feature disappears in calculations that neglect two-exciton states [33]. Biexciton coherence is formed by either the transition from an exciton population or via a direct and coherent two-quantum transition from the ground state to the biexciton state. The two-quantum transition can be isolated with experiments where all three excitation pulses are phase-locked [33].
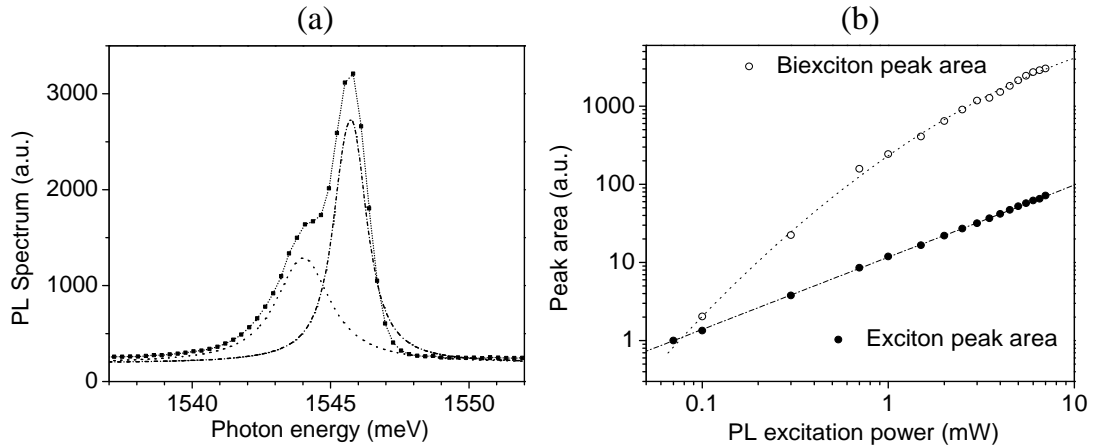

Figure 6.8: Exciton and biexciton peaks in power-dependent photoluminescence (PL) spectra. (a) A PL spectrum (square and dot line) measured at excitation power of 1 mW is fitted with an exciton peak (dash-dot line) and a biexciton peak (dot line) of the Lorentzian shape; (b) The peak areas of exciton (solid circle) and biexciton (open circle) from the fits in (a) versus PL excitation power.

The formation of biexciton can also be observed in photoluminescence (PL) spectra. In the PL spectrum shown in Fig. 6.8(a), the peak at HH exciton energy is revealed as the combination of an exciton peak and a biexciton peak by a double Lorentzian fit. The peak height, peak center and linewidth can be obtained from the fit, which gives a biexciton linewidth equal to about twice that of the exciton. The power-dependent PL measurement further confirms the biexciton formation. PL spectra were measured with varying excitation power and the relative peak areas of exciton and biexciton contributions were extracted by the fit. Fig. 6.8(b) shows the exciton peak area has a linear dependence on the excitation power, whereas the biexciton peak area increases quadratically before saturation. This power-dependence of the biexciton is in good agreement with an early work on the thermodynamic evaluation of exciton and biexciton populations [134].

Chapter 7

Raman Coherences Revealed by Alternative 2D FTS

In general, a heterodyne-detected transient FWM signal is three-dimensional, i.e. it is determined by time variables τ, T, and t in time-domain, thus its spectral representation is a function of ω_τ, ω_T, and ω_t generated by a three-dimensional Fourier transformation. In the 2D FTS approach discussed in previous chapters, a spectrum is displayed as a map on two frequencies, the absorption frequency ω_τ and emission frequency ω_t, while the waiting time T is fixed. With a different scheme of Fourier transform variables, an alternative approach can project the photon echo signal in the plane of ω_T and ω_t, with a constant τ. The spectrum projected in this way is denoted as $\mathcal{S}_\mathrm{I}(\tau, \omega_T, \omega_t)$, whereas the conventional 2D FTS is referred as $\mathcal{S}_\mathrm{I}(\omega_\tau, T, \omega_t)$. In this chapter, we demonstrate that the new 2D projection can isolate Raman coherences and other many-body correlations that are mixed in the conventional 2D FTS, thus provides complementary information to the latter one [135].

Raman coherences are of interest for the study of coherent processes in photosynthetic complexes [78, 136] and in semiconductors. In semiconductors, non-radiative Raman coherence between HH and LH excitonic states was measured from the quantum beats in a transient absorption experiment [137]. Further work studied the essential role of exciton-exciton interactions in producing the signal [138]. Evidence for inter-valence band coherences was also found by using the optical Stark effect [132]. Recently, time-integrated FWM was measured in three-pulse experiments for the simultaneous de-

phasing of both the Raman and optical coherences [139], allowing the determination of the correlation coefficient for the dephasing processes. The presence of non-radiative Raman coherences is essential for effects including electromagnetically-induced transparency, lasing without inversion, and slow light [140].

7.1   Coherent pathways contributing to the photon echo signal

To learn how Raman coherences can be isolated by the alternative 2D approach, we compare the contributions of coherent pathways to peaks in the two 2D projections. Within the rotating-wave approximation, three fundamental coherent pathways contribute to the photon echo signal emitted in the phase-matched direction $\mathbf{k}_I = -\mathbf{k}_1 + \mathbf{k}_2 + \mathbf{k}_3$. These pathways, corresponding to the processes of ground-state bleaching (GSB), excited-state emission (ESE), and excited-state absorption (ESA) [82], can be respectively represented by the Feynman diagrams labeled with (1), (2), and (3) in Fig. 3.2(a). We first consider the coherent pathway contributions from HH and LH excitons only, in this case only diagrams (1) and (2) are involved. For a three-level system with HH and LH exciton states $|e_H\rangle$ and $|e_L\rangle$, and ground state $|g\rangle$, with a transition frequency ω_H between $|e_H\rangle$ and $|g\rangle$ and ω_L between $|e_L\rangle$ and $|g\rangle$, there are four diagrams of the GSB type and four of the ESE type. They are all depicted in Fig. 3.6(a). The rephasing 2D spectrum of the $\mathcal{S}_I(\omega_\tau, T, \omega_t)$ projection is illustrated in Fig. 7.1(a), which is a replica of Fig. 3.6(b) to allow comparison between different 2D projections. Each diagonal peak or cross peak arises from the contributions of two different coherent pathways. The pathways corresponding to the Raman coherences between the two excited states, (2c) and (2d), mix up with (1c) and (1d), respectively, and contribute to the two cross peaks. With such a degeneracy, interference of the two types of coherent pathways forms, making it not possible to observe Raman coherences alone. In general, one has to measure $\mathcal{S}_I(\omega_\tau, T, \omega_t)$ spectra with varying waiting time T

and observes the oscillation of cross peak strength [78, 136]. This indirect approach for the study of Raman coherences requires a large number of 2D spectra to be measured and thus quite time consuming.
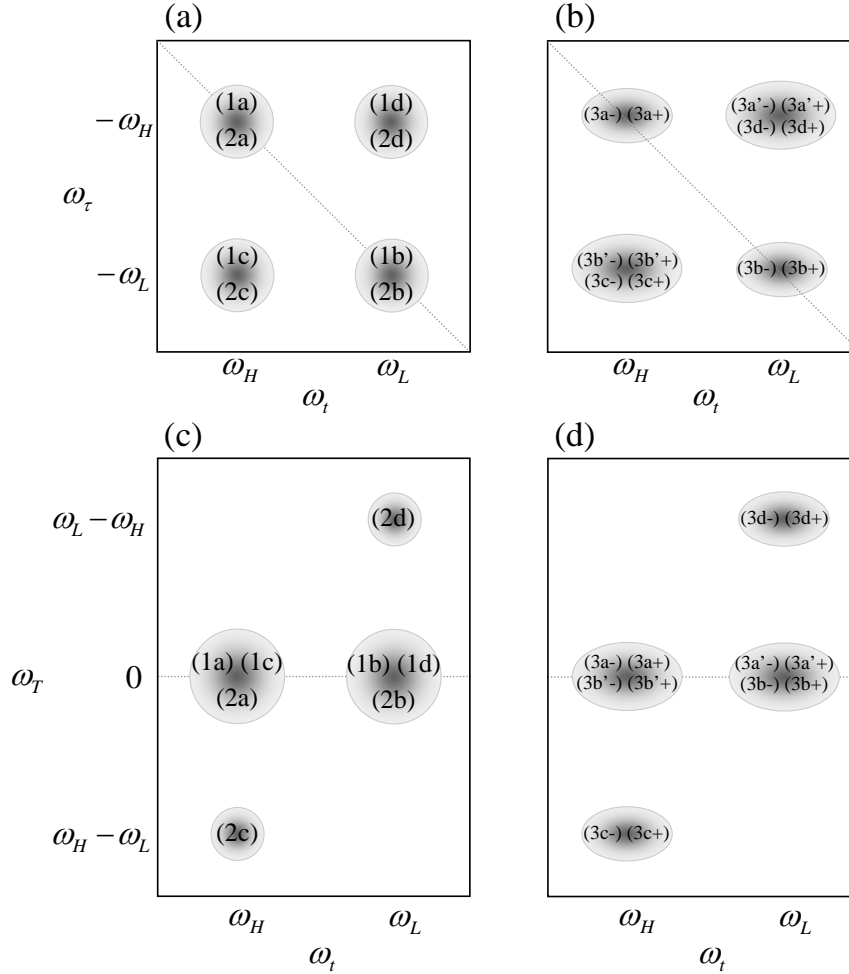

Figure 7.1: The schematic 2D spectrum arising from the contributions of type (1) and type (2) coherent pathways, and that from type (3) pathway contributions are shown respectively in (a) and (b) in the conventional $\mathcal{S}_I(\omega_\tau, T, \omega_t)$ 2D projection, and in (c) and (d) in the alternative $\mathcal{S}_I(\tau, \omega_T, \omega_t)$ projection.

In the $\mathcal{S}_I(\tau, \omega_T, \omega_t)$ 2D projection, coherent pathways distribute among peaks differently. As shown in Fig. 7.1(c), Raman coherence pathway (2c) contributes to the side peak at $\omega_t = \omega_H$ and $\omega_T = \omega_H - \omega_L$, whereas (2d) falls onto another side peak at $\omega_t = \omega_L$ and $\omega_T = \omega_L - \omega_H$, completely separated from other pathways. The

primary peak at $\omega_t = \omega_H$ and $\omega_T = 0$ arises from three pathways: (1a), (2a), and (1c), whereas the other primary one is from (1b), (2b), and (1d). Similarly, the coherent pathways involving two-exciton states also contribute to 2D spectra differently in the new projection. As listed in Fig. 3.7(a), there are six such diagrams derived from the type (3) diagram (ESA) in Fig. 3.2(a). The pathway (3a) leads to $|f_H\rangle$, the state of two HH excitons, pathway (3b) to $|f_L\rangle$, that of two LH excitons, and pathways (3a'), (3b'), (3c), and (3d) to $|f_M\rangle$, the state of mixed HH and LH excitons. The 2D spectrum with two-exciton contributions in the $\mathcal{S}_I(\omega_\tau, T, \omega_t)$ projection is shown schematically in Fig. 7.1(b)(duplicated from Fig. 3.7(b)), along with the $\mathcal{S}_I(\tau, \omega_T, \omega_t)$ spectrum in Fig. 7.1(d), separated from the 2D spectra of single-exciton contributions in (a) and (c) for clarity. Each two-exciton state can have three different conditions: the bound state, unbound state, and bare two-exciton state (two correlated excitons without energy shift arising from the correlation). Consequently, all peaks in the 2D spectra of (b) and (d) are elongated along ω_t axis to reflect the red-shift by bound two-excitons and blue-shift by unbound two-excitons. The pathways of bound and unbound two-excitons are indicated respectively by a suffix "-" and "+" to the labels of diagrams. Apparently, two-exciton coherent pathways contribute differently in the two projections. Pathways (3c) and (3d) are isolated as the respective side peak at $\omega_t = \omega_H$, $\omega_T = \omega_H - \omega_L$, and $\omega_t = \omega_L$, $\omega_T = \omega_L - \omega_H$ in the $\mathcal{S}_I(\tau, \omega_T, \omega_t)$ spectrum. The contribution from the ESA pathways (type (3) diagrams) to Raman coherence has a minus sign, as compared to that from ESE (type (2) diagrams), thus it reduces signal strength. However, the contribution from two-exciton states in semiconductor quantum wells is small if the excitation pulse is in near resonance with the single-exciton resonances. In this case, the two side peaks in the $\mathcal{S}_I(\tau, \omega_T, \omega_t)$ projection are dominated by the ESE pathways.

7.2 Experimental $\mathcal{S}_\mathrm{I}(\tau, \omega_T, \omega_t)$ spectra

In this section, we demonstrate the experimental implementation of $\mathcal{S}_\mathrm{I}(\tau, \omega_T, \omega_t)$ 2D projection. The same box-geometry described in Chapter 4 is employed to obtain photon echo signals in the $\mathbf{k}_\mathrm{I}$ phase-matched direction. The delay T between the second and third excitation pulses is scanned with a step size of 26.67 fs by a translation stage, whereas the delay τ is set to 0 and actively stabilized by the servo loop. The phase of the reference relative to the third pulse is also actively stabilized for the heterodyne detection. The $\mathcal{S}_\mathrm{I}(\tau, \omega_T, \omega_t)$ 2D spectrum is produced from the complex FWM electric field retrieved from the spectral interferometry with the reference. The direct frequency, ω_t, is obtained from the spectral interferometry, and indirect frequency, ω_T, from the Fourier transform with respect to T that is performed numerically.
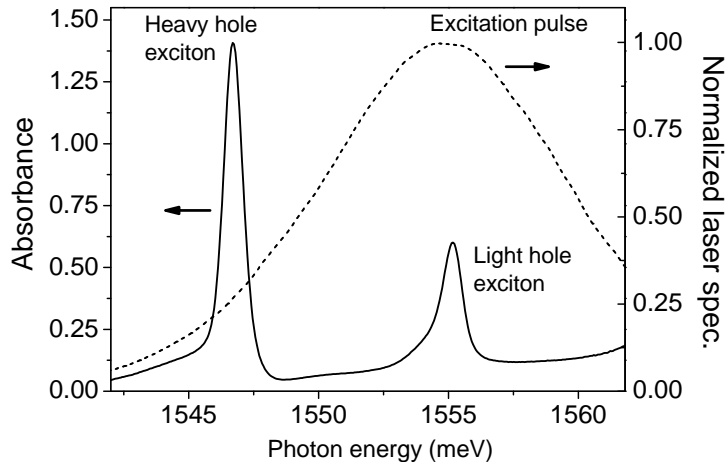

Figure 7.2: Linear absorption of the GaAs/Al$_{0.3}$Ga$_{0.7}$As multiple quantum well sample (solid line) and the excitation pulse spectrum (dash line).

A GaAs multiple quantum well sample with the same well structure as described in Section 4.2 was used for the 2D measurements. In Fig. 7.2, the linear absorption spectrum of the sample shows an energy separation of 8.4 meV between HH and LH exciton resonances. The laser is tuned to the LH exciton resonance to compensate for
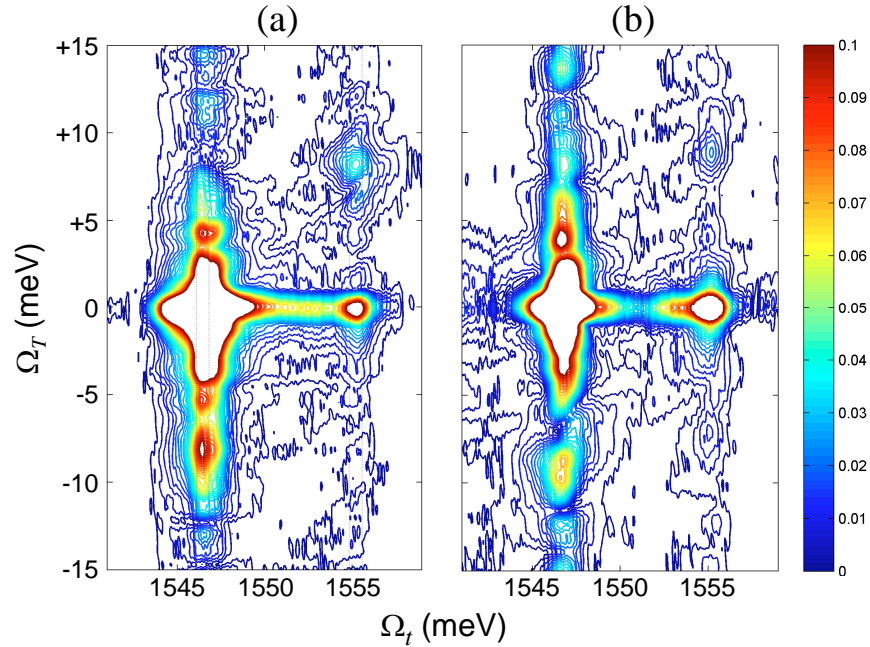
Figure 7.3: Experimental amplitude $\mathcal{S}_\mathrm{I}(\tau, \Omega_T, \Omega_t)$ spectra measured in the photon echo phase-matched direction with colinear-polarized (a) and cocircular-polarized (b) excitations. Both spectra are normalized to amplitude separately and represented with 100 contour lines at 10% of the full scale to enhance side peaks.

its weak oscillator strength. The excitation power for new experiments is comparable to that used in conventional measurements.

The $\mathcal{S}_\mathrm{I}(\tau, \omega_T, \omega_t)$ 2D spectra were measured with colinear- and cocircular-polarized excitations. The experimental results are shown in Fig. 7.3(a) and (b), where the two axes of the spectra are defined as $\Omega_t = \hbar\omega_t$ and $\Omega_T = \hbar\omega_T$ in photon energy. Both spectra are plotted at 10% of the full scale to enhance the weak side peaks. The two side peaks show up at $(\Omega_t, \Omega_T) = (1546.0, -8.4)$ and $(1553.4, 8.4)$, well separated from the strong primary peaks at $\Omega_T = 0$. The appearance of side peaks manifests the coherent pathway analysis in the previous section. The lower side peak arises from pathways (2c) of Raman coherence and (3c±) of two-exciton contributions, whereas the upper one from the pathways (2d) and (3d±). It is worth noting that the relative strength of side peaks in the spectrum with cocircular-polarized excitation (Fig. 7.3(b)) is smaller

than that in the case of colinear-polarized excitation (Fig. 7.3(a)).

We note that "windowing" is applied to the time series of FWM signal with waiting time T for the spectra in Fig. 7.3. The decay of Raman coherence with waiting time T happens simultaneously with the population relaxation, whereas the latter lasts much longer than the Raman coherence. Truncation at the end of the time series with limited length causes severe "ringing" along Ω_T after the Fourier transform. An appropriate window function is usually needed to suppress the ripples without undue linewidth broadening along transform direction [8]. The cross-sections along Ω_T at $\Omega_t = \Omega_H$ and Ω_L in the 2D spectrum with colinear-polarized excitation (Fig. 7.3(a)) are shown in Fig. 7.4(a) and (b), respectively. The weak side peaks are made visible from the ripples when a Hanning window is applied, which is of the form $h(T) = 0.5 + 0.5\cos(\pi T/T_0)$. The Hanning window 1 and 2 in Fig. 7.4 correspond to a T_0 equal to 60% and 100% of the total time series length, respectively.

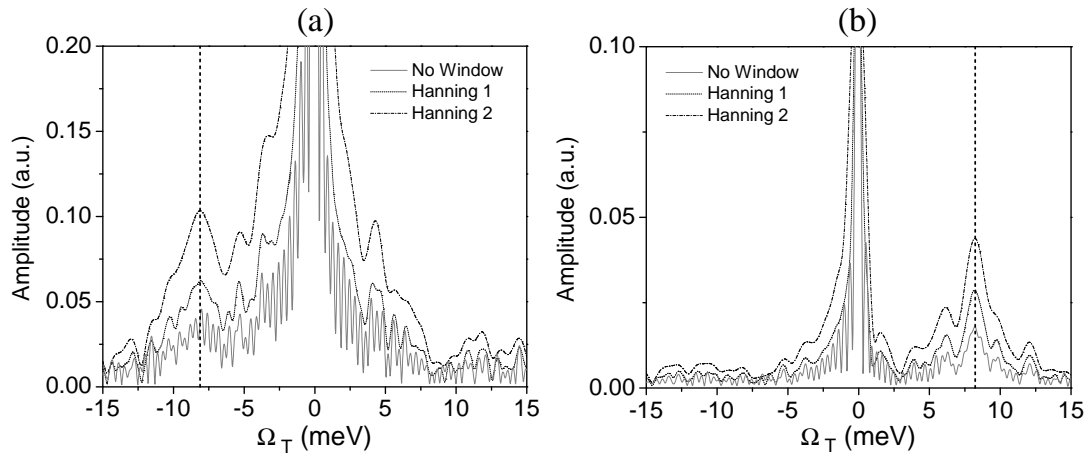Figure 7.4: Cross-sections along Ω_T at $\Omega_t = \Omega_H$ (a) and Ω_L (b) in experimental amplitude $\mathcal{S}_I(\tau, \Omega_T, \Omega_t)$ spectrum with colinear-polarized excitation. The suppression of ripples by applying window is demonstrated.

7.3 Microscopic calculations of $\mathcal{S}_{\mathrm{I}}(\tau, \omega_T, \omega_t)$ spectra

To better understand the experimental observations, we compare to microscopic calculations of the $\mathcal{S}_{\mathrm{I}}(\tau, \omega_T, \omega_t)$ spectra, which were performed by our collaborators in University of California, Irvine [135]. The calculations are based on a multi-band 1D tight-binding model [33], which includes HH, LH excitons and their continuum states in a tractable way and accounts for various features in time-integrated/time-resolved FWM [25] and 2D FTS [33, 107] qualitatively. The equations of motion are truncated according to the dynamics-controlled truncation scheme [124, 141]. In the calculations, material parameters are chosen to fit the HH and LH exciton resonance energies, oscillator strengths and energy splitting between them.
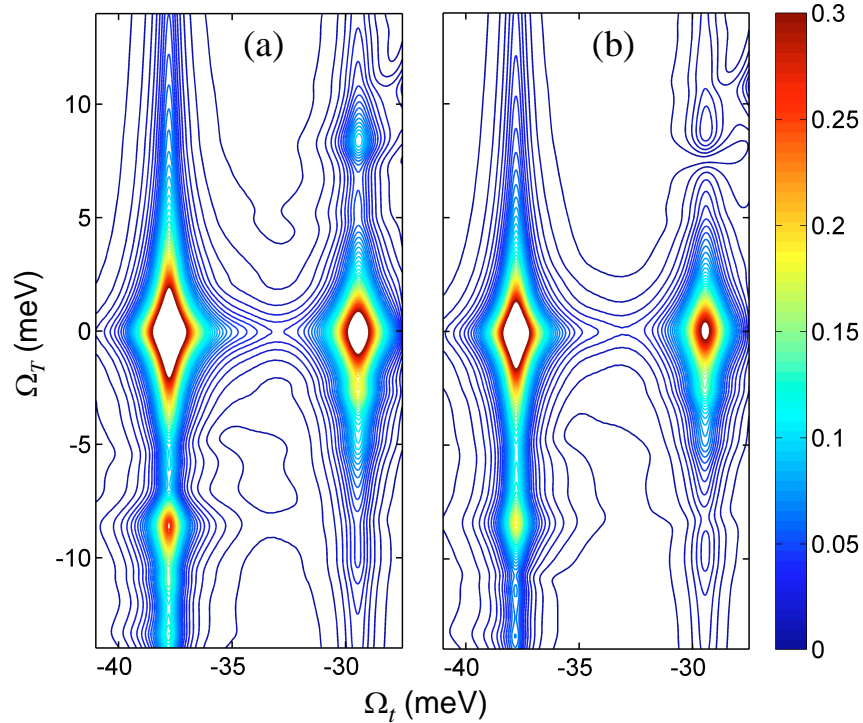

Figure 7.5: Calculated amplitude 2D spectra with colinear-polarized (a) and cocircular-polarized (b) excitations. Energy values along the Ω_t axis are relative to the top of the bandgap. Both spectra are normalized to amplitude separately and represented with 50 contour lines at 30% of the full scale.

Fig. 7.5 shows the calculated $\mathcal{S}_I(\tau, \Omega_T, \Omega_t)$ 2D spectra of colinear-polarized and cocircular-polarized excitation in (a) and (b), respectively. Energy values along the Ω_t axis are relative to the top of the bandgap. The HH (LH) exciton resonance energy is -37.9 meV (-29.5 meV). In each spectrum there are two Raman coherence peaks, one centered at $(\Omega_t, \Omega_T) = (-37.9, -8.4)$, and the other at $(\Omega_t, \Omega_T) = (-29.5, 8.4)$. We find that the relative strength of side peaks in (b) is smaller compared to that in (a). The appearance of side peaks and the relative peak strength agree with the experimental result in Fig. 7.3 qualitatively.

Figure 7.6: Calculated amplitude 2D spectra with colinear-polarized (a) and cocircular-polarized (b) excitations in the time-dependent Hartree–Fock approximation. Energy values along the Ω_t axis are relative to the top of the bandgap. Both spectra are normalized to amplitude separately and represented with 50 contour lines at 30% of the full scale.
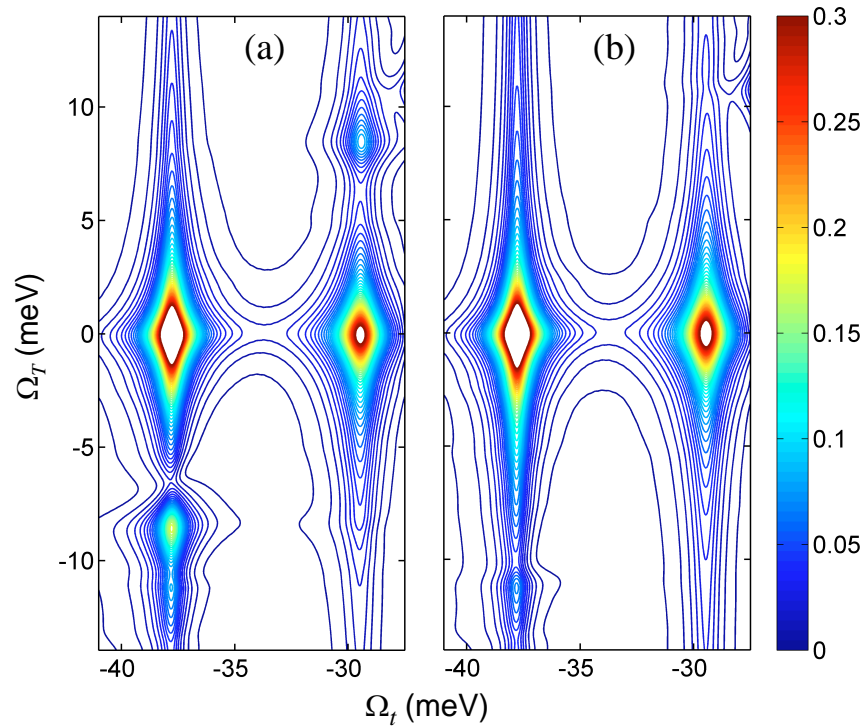
In comparison, Fig. 7.6 shows the calculated 2D spectra with colinear-polarized and cocircular-polarized excitations in the time-dependent Hartree–Fock (TDHF) ap-

proximation [33], i.e. without including correlated two-exciton states. There are still two side peaks corresponding to Raman coherences in Fig. 7.6(a), meaning HH and LH excitons are coupled in the case of colinear-polarized excitation, even within the TDHF approximation. However, the side peaks disappear completely in the spectrum with cocircular-polarized excitation in Fig. 7.6(b), where the weak features close to the side peak positions are from the continuum states. Therefore, there is no coupling between HH and LH excitons in the TDHF limit, with cocircular-polarized excitation. The side peaks presented in the full calculation (Fig. 7.5(b)) are from higher-order correlation effects beyond the TDHF approximation. The alternative 2D projection of photon echo signal, $\mathcal{S}_\mathrm{I}(\tau, \Omega_T, \Omega_t)$, provides additional microscopic information about the coupling of excitons.

Appendix A

2D FTS of Double Quantum Wells

An asymmetric double quantum well (DQW) structure consists of two quantum wells of unequal thickness separated by a barrier layer. With electronic coupling strength and tunneling rate between the two wells controlled conveniently by the barrier thickness, the DQW structure is a unique model system for many intriguing dynamic processes in semiconductors [2]. In practice, many optoelectronic devices employ DQW structures, where the electronic coupling between inter-well transitions has significant influences on the electro-optical properties [142].

We apply the approach of 2D FTS to DQW structures for the identification of electronic coupling and measurement of coupling strength [143]. Two different DQW samples are studied, both consisting of 10 periods of alternating $8\,\text{nm}$ and $9\,\text{nm}$ GaAs quantum wells. The thickness of the barrier, $\text{Al}_{0.3}\text{Ga}_{0.7}\text{As}$, is $10\,\text{nm}$ in one sample (referred as sample A) and $1.7\,\text{nm}$ in another (sample B). Based on numerical calculations of the single-particle eigenstates of the conduction band, HH, and LH valence sub-bands [144], the energy level structure and possible optical transitions for the two DQW samples are depicted schematically in Fig. A.1, where the electron, HH, and LH states in the wide (narrow) well are labeled as E1 (E2), HH1 (HH2), and LH1 (LH2), respectively. Four optical transitions are allowed in the DQW sample A, as shown in Fig. A.1(a). In the order of increasing energy, these transitions are HH1→E1, HH2→E2, LH1→E1, and LH2→E2. The corresponding exciton resonances observed experimen-

tally are denoted as $X_{\mathrm{HH1}\to\mathrm{E1}}$, $X_{\mathrm{HH2}\to\mathrm{E2}}$, $X_{\mathrm{LH1}\to\mathrm{E1}}$, and $X_{\mathrm{LH2}\to\mathrm{E2}}$, respectively. With a barrier of 10 nm thick, electron and hole wavefunctions are localized in individual wells, therefore no coupling is expected between exciton resonances in different wells. In the DQW sample with a barrier thickness of 1.7 nm, the electron wavefunctions are extended in both wells and overlap with the HH wavefunctions, resulting in six possible transitions: HH1→E1, HH2→E1, HH1→E2, HH2→E2, LH1→E1, and LH2→E2. The energetic splitting between the two HH states is so small that they are unresolved in our experiments. The four resonances observed are tentatively labeled as $X_{\mathrm{HH}\to\mathrm{E1}}$, $X_{\mathrm{HH}\to\mathrm{E2}}$, $X_{\mathrm{LH1}\to\mathrm{E1}}$, and $X_{\mathrm{LH2}\to\mathrm{E2}}$ from the lower to higher energies. The accurate assignment of these resonances is difficult due to complications caused by valence band mixing and strain effects.
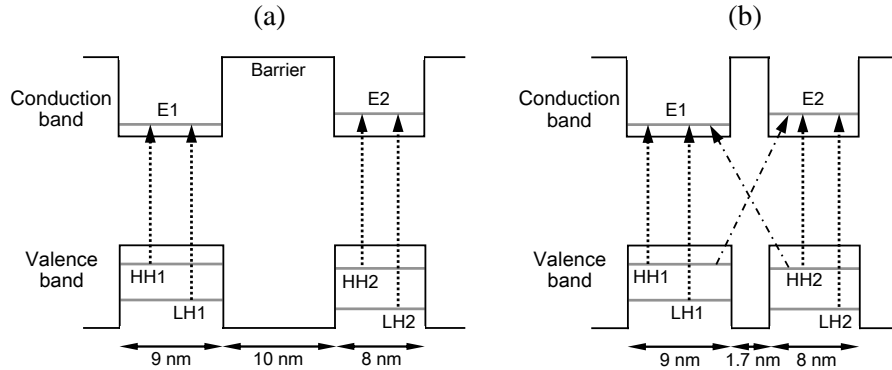
Figure A.1: Schematic energy level structure and optical transitions for the DQW sample with a barrier thickness of 10 nm (a) or 1.7 nm (b). The electron, HH, and LH states in the wide (narrow) well are labeled as E1 (E2), HH1 (HH2), and LH1 (LH2), respectively.

Next we discuss the manifestation of electronic coupling in 2D spectra. In the DQW sample A, transitions from the HH and LH states to the electron state confined in the same well are coupled, whereas no coupling is expected between transitions in different wells. Therefore, an amplitude 2D spectrum of the $\mathcal{S}_{\mathrm{I}}(\omega_\tau, T, \omega_t)$ type can be plotted schematically as Fig. A.2(a), where the red circles on the diagonal represent

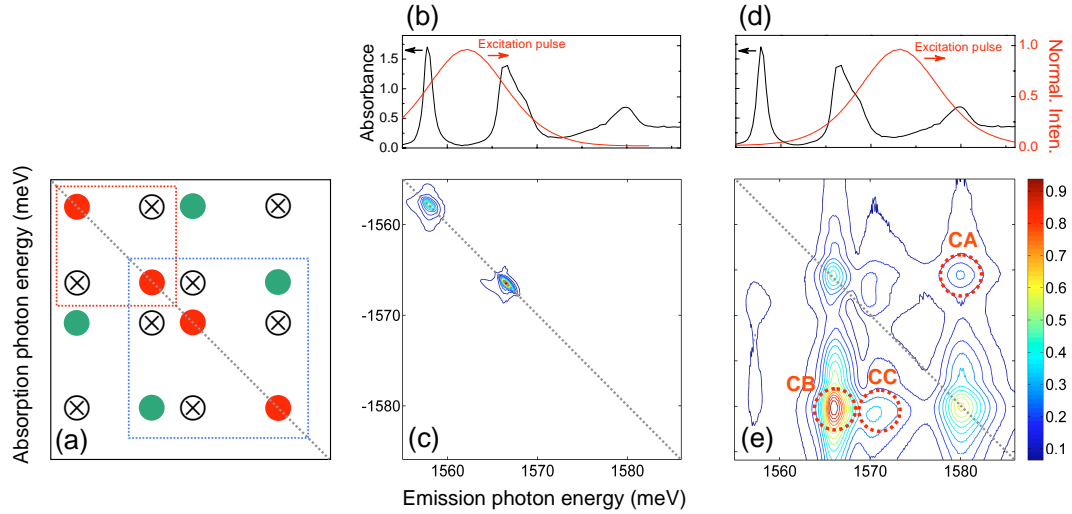Figure A.2: (a) Expected amplitude 2D spectrum for the DQW sample A (barrier thickness of 10 nm); (b) The linear absorption of sample A (black line) and the excitation pulse (red line) that is tuned to the middle of the lower two transitions; (c) The experimental amplitude 2D spectrum with the tuning in (b), corresponding to an area enclosed by the red box in (a); (d) The linear absorption (black line) and the excitation pulse (red line) that is tuned to the higher three transitions; (e) The experimental amplitude 2D spectrum with the tuning in (d), corresponding to an area enclosed by the blue box in (a). $T = 6.67$ ps for both 2D spectra.

the four exciton resonances, the off-diagonal green circles indicate the couplings due to common electron states, and the circles with a cross inside mean no cross peaks expected there. As depicted in Fig. A.2(b), the resonance peaks in the linear absorption spectrum of sample A arise from the transitions HH1→E1, HH2→E2, LH1→E1, and LH2→E2. Since the second and third transitions have quite close energy, they are not well resolved in the absorption. Due to limited bandwidth of the laser pulse, not all the four transitions can be excited simultaneously. The laser was first tuned to the middle of the lower two transitions, as shown in Fig. A.2(b), leading to an amplitude 2D spectrum displayed in Fig. A.2(c). Only two diagonal peaks appear without any cross peaks, confirming that these two resonances arise from the HH exciton transitions localized in the two spatially-separated quantum wells. Then a different laser tuning was used to cover the three transitions at higher energies, as shown in Fig. A.2(d). In

the resulted amplitude 2D spectrum in Fig. A.2(e), two cross peaks (CA and CB) arise as the indication of coupling between transitions HH2→E2 and LH2→E2. It is worth noting that the cross peak CB has the strongest strength, similar to the feature observed in the 2D spectra of ordinary multiple quantum wells. This feature is resulted from the many-body interactions of excitons, as discussed in Chapter 5.

The appearance of cross peak CC is surprising for a large barrier thickness of 10 nm. The same cross peak is still present even when the waiting time is reduced from 6.67 ps to 200 fs (spectrum not shown). This peak may arise from energy transfer, although it is not clear whether energy transfer can happen effectively between excitons localized in spatially-separated quantum wells. Possible transfer mechanisms include dipole-dipole interaction, intrinsic structural inhomogeneity, Auger process, and two-photon absorption [143]. It is difficult to identify the exact mechanism based on the measurements presented here. The fact that only one cross peak appears below the diagonal implies the mechanism of coupling between these two LH transitions may be incoherent relaxation. If this is the case, the energy transfer or relaxation happens on a time scale shorter than the laser pulse duration.

For the DQW sample B with a barrier thickness of 1.7 nm, four distinct resonances show up in the linear absorption spectrum in Fig. A.3(b). These resonances are due to the six possible transitions, HH1→E1, HH2→E1, HH1→E2, HH2→E2, LH1→E1, and LH2→E2. The speculated amplitude 2D spectrum is shown in Fig. A.3(a), where only coupling due to common electron states is considered to contribute to cross peaks. Because of the difficulties in assigning the transitions, it is not clear if some of the cross peaks would appear. These peaks are indicated by circles with a question mark inside. As shown in Fig. A.3(b), the laser pulse was tuned to excite all the resonances and the resulted amplitude 2D spectrum is displayed in Fig. A.3(c). A checker-broad pattern is observed, indicating that all the resonances are coupled with one another. This result suggests that there are contributions from effects of valence band mixing, which are
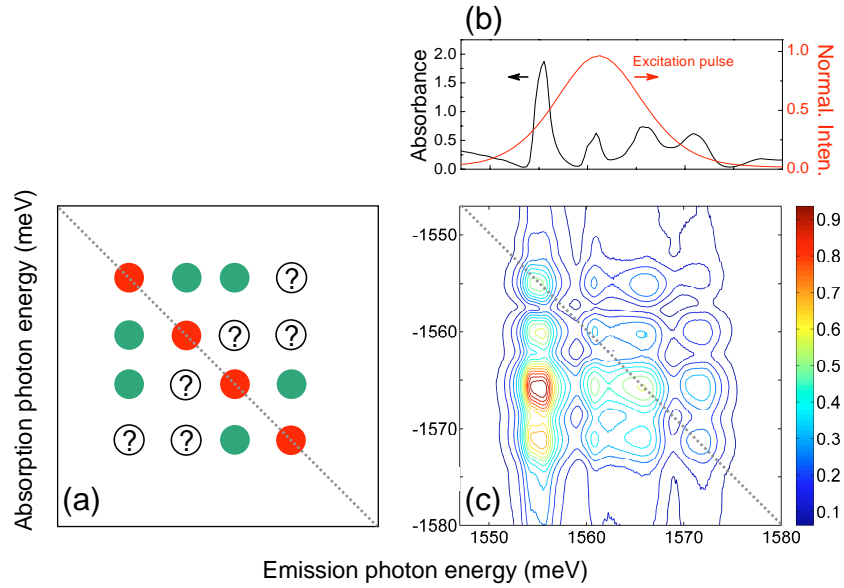
Figure A.3: (a) Expected amplitude 2D spectrum for the DQW sample B (barrier thickness of 1.7 nm); (b) The linear absorption of sample B (black line) and the laser pulse (red line) that excites all the transitions; (c) The experimental amplitude 2D spectrum with the tuning in (b), measured with $T = 6.67\,\text{ps}$.

not included in the calculations of the single-particle eigenstates. Valence band mixing would couple HH and LH states and account for the observed 2D spectrum.

The strength of cross peaks is observed to change with the waiting time. Fig. A.4 show the amplitude 2D spectra of sample B with $T = 280\,\text{fs}$ (a) and $400\,\text{fs}$ (b), which correspond to the respective maximal and minimal point in the scan of time-integrated FWM signal with T. These changes are resulted from the interference between different coherent pathways contributing to the cross peaks. As discussed in Chapter 7, the cross peaks in the $\mathcal{S}_\text{I}(\omega_\tau, T, \omega_t)$ type 2D spectra arise from two terms, referred as "ground state bleaching" and "excited state emission" [33]. The "excited state emission" terms, when appearing at the cross-peak positions, include the Raman coherence. As the waiting time T varies, the phase of the Raman coherence terms changes, leading to constructive or destructive interference with the coherent pathways of the "ground state bleaching"
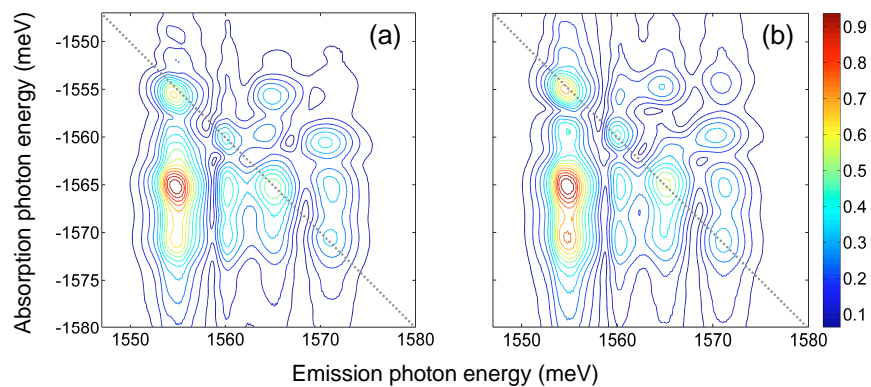
Figure A.4: Experimental amplitude 2D spectra of sample B with different waiting times. (a) $T = 280\,\mathrm{fs}$ and (b) $T = 400\,\mathrm{fs}$ correspond to the respective maximal and minimal point in the scan of time-integrated FWM signal with T.

terms. Such oscillatory behavior of cross peak strength has been observed in the 2D spectra of electronic transitions in photosynthetic systems [136].

Appendix B

2D FTS of Exciton Continuum

The carrier-carrier interactions in semiconductors have been demonstrated to have significant contributions to the coherent optical response [51, 145, 146, 147]. Unbound electron-hole pairs, i.e. exciton continuum states, can be created with laser pulses tuned above the exciton resonance. As observed in the $\mathcal{S}_\mathrm{I}(\omega_\tau, T, \omega_t)$ type 2D spectra, a vertical stripe due to the absorption of the continuum states appears at the emission photon energies of both HH and LH excitons. However, the continuum manifests as a diagonal feature in the 2D spectra, rather than a vertical stripe, if it acts as a set of inhomogeneously broadened transitions, as shown by the calculations in Chapter 5. The vertical stripes occur because unbound electron-hole pairs strongly couple to the excitonic resonances [51], resulting in a dominant signal at the resonances.

In order to explore the structure of continuum states, 2D FTS experiments have been performed with excitation pulses tuned well above the exciton resonance. The bulk exciton resonance appears at 1515 meV in a GaAs sample cooled to 10 K. Laser pulses with a tuning of 1521 meV and an excitation power of 4.0 mW per beam is used to obtain dominant continuum states. The continuum is excited by the full pulse bandwidth (FWHM ~ 12 meV) and the coherence is expected to exist on a timescale comparable to the pulse duration. Fig. B.1 depicts the experimental rephasing 2D spectra of exciton continuum states with colinear-polarized excitation, where amplitude and real part spectra with waiting time T of 50, 150, and 250 fs are shown. For different
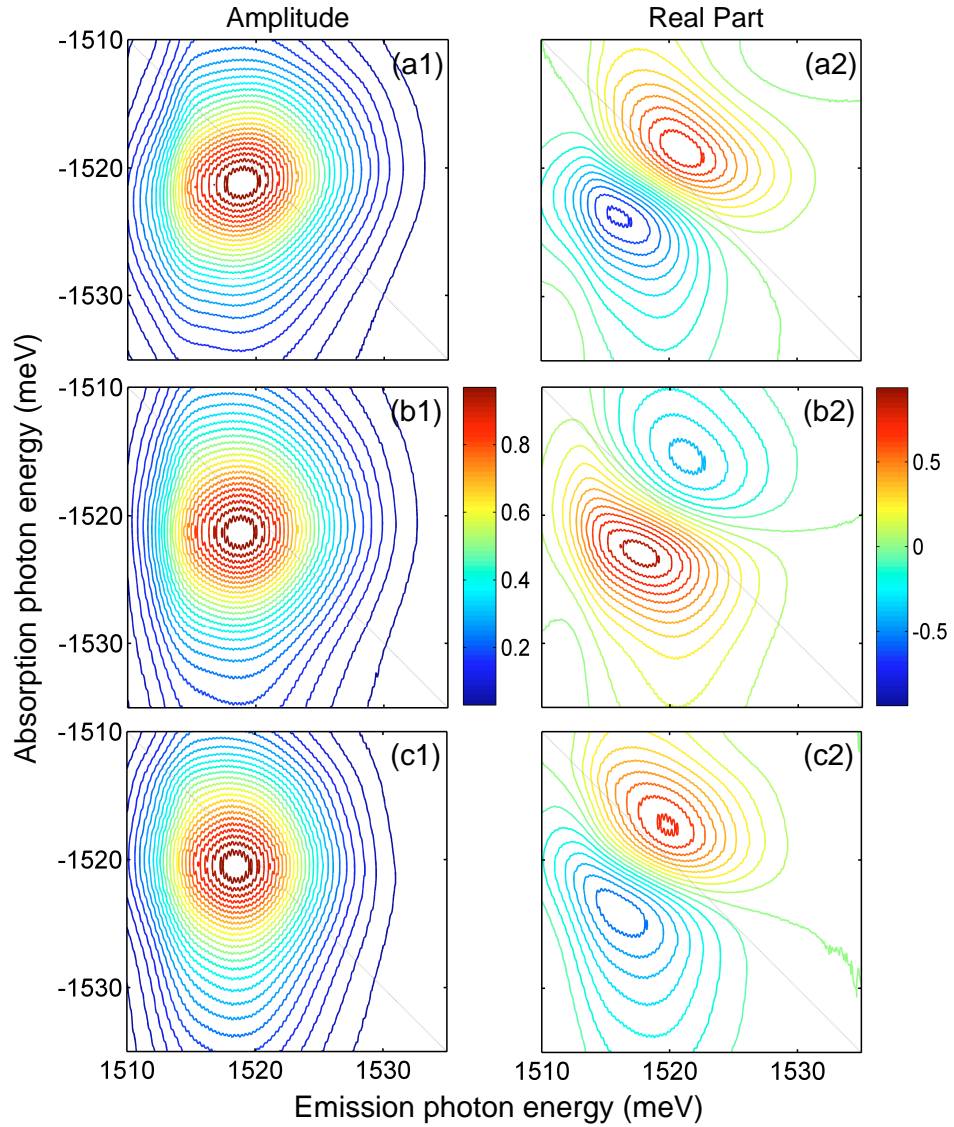
Figure B.1: Experimental rephasing 2D spectra of exciton continuum. Amplitude (left column) and real part (right column) spectra with waiting time T of 50, 150, and 250 fs are shown in row (a), (b), and (c), respectively. All spectra were obtained with colinear-polarized excitation.

values of T, a broad and almost round-shape peak appears in the amplitude plot, with a strongly-dispersive lineshape for the real part. The peak appears at a position with the absorption and emission photon energy equal to -1521 and 1518 meV, respectively. The red-shift from the diagonal along the emission axis is consistent with a weakening

of the Coulomb interaction for higher k-states and possibly an increase in the dephasing rate [148]. The red-shift increases slightly with T, however, it remains small even at a large T corresponding to the complete decoherence of the continuum states, implying that the incoherent scattering process may not dominate the spectra. Compared to the rephasing 2D spectra, the non-rephasing spectra of continuum are much weaker (not shown), indicating the continuum acts like an inhomogeneously broadened system. However, such a system would result in a diagonal feature in the rephasing spectra, which is in contradiction to the observation. This mixed behavior may imply that the continuum states have an underlying inhomogeneous structure, but the states are coupled together through many-body interactions.

While the amplitude 2D spectra are similar in the range of T discussed, the real part spectra present a phase inversion from $T = 50\,\text{fs}$ to $250\,\text{fs}$. The phase oscillation only occurs during the coherent lifetime of the population, therefore no phase inversion can be observed with larger T. It is possible that the coherent intraband scattering processes may result in such a phase inversion, although further investigations are needed to verify this.

2D FTS experiments with cocircular-polarized excitation were also performed. In the amplitude and real part spectra, only subtle differences can be observed from the case of colinear-polarized excitation with the same T and pulse power. The weak dependence on polarization is not surprising for the continuum, since the spin-splitting of the continuum states is negligible compared to the range of k-states simultaneously excited. In this regime, intraband electron-electron effects, rather than interband contributions, dominate over the initial coherence and relaxation.

Bibliography

[1] S. T. Cundiff, "Coherent spectroscopy of semiconductors," Opt. Expr. **16**, 4639 (2008).

[2] J. Shah, Ultrafast spectroscopy of semiconductors and semiconductor nanostructures, 2nd ed. (Springer ser. sol.-stat. sci.) (Springer, 1999).

[3] M. Wegener, D. S. Chemla, S. Schmitt-Rink, and W. Schäfer, "Line shape of time-resolved four-wave mixing," Phys. Rev. A **42**, 5675 (1990).

[4] K. Bott, O. Heller, D. Bennhardt, S. T. Cundiff, P. Thomas, E. J. Mayer, G. O. Smith, R. Eccleston, J. Kuhl, and K. Ploog, "Influence of exciton-exciton interactions on the coherent optical response in GaAs quantum wells," Phys. Rev. B **48**, 17418 (1993).

[5] H. Wang, K. Ferrio, D. G. Steel, Y. Z. Hu, R. Binder, and S. W. Koch, "Transient nonlinear optical response from excitation induced dephasing in GaAs," Phys. Rev. Lett. **71**, 1261 (1993).

[6] J. M. Shacklette and S. T. Cundiff, "Role of excitation-induced shift in the coherent optical response of semiconductors," Phys. Rev. B **66**, 045309 (2002).

[7] M. Koch, J. Feldmann, G. von Plessen, E. O. Göbel, P. Thomas, and K. Köhler, "Quantum beats versus polarization interference: An experimental distinction," Phys. Rev. Lett. **69**, 3631 (1992).

[8] R. R. Ernst, G. Bodenhausen, and A. Wokaun, Principles of nuclear magnetic resonance in one and two dimensions (Oxford University Press, Oxford, 1987).

[9] Y. Tanimura and S. Mukamel, "Two-dimensional femtosecond vibrational spectroscopy of liquids," J. Chem. Phys. **99**, 9496 (1993).

[10] J. D. Hybl, A. W. Albrecht, S. M. Gallagher Faeder, and D. M. Jonas, "Two-dimensional electronic spectroscopy," Chem. Phys. Lett. **297**, 307 (1998).

[11] A. Tokmakoff, M. J. Lang, D. S. Larsen, G. R. Fleming, V. Chernyak, and S. Mukamel, "Two-dimensional Raman spectroscopy of vibrational interactions in liquids," Phys. Rev. Lett. **79**, 2702 (1997).

[12] D. A. Blank, L. J. Kaufman, and G. R. Fleming, "Fifth-order two-dimensional Raman spectra of CS_2 are dominated by third-order cascades," J. Chem. Phys. **111**, 3105 (1999).

[13] M. C. Asplund, M. T. Zanni, and R. M. Hochstrasser, "Two-dimensional infrared spectroscopy of peptides by phase-controlled femtosecond vibrational photon echoes," Proc. Natl. Acad. Sci. **97**, 8219 (2000).

[14] M. T. Zanni, S. Gnanakaran, J. Stenger, and R. M. Hochstrasser, "Heterodyned two-dimensional infrared spectroscopy of solvent-dependent conformations of acetylproline-NH_2," J. Phys. Chem. B **105**, 6520 (2001).

[15] M. L. Cowan, B. D. Bruner, N. Huse, J. R. Dwyer, B. Chugh, E. T. J. Nibbering, T. Elsaesser, and R. J. D. Miller, "Ultrafast memory loss and energy redistribution in the hydrogen bond network of liquid H_2O," Nature **434**, 199 (2005).

[16] A. A. Maznev, K. A. Nelson, and J. A. Rogers, "Optical heterodyne detection of laser-induced gratings," Opt. Lett. **23**, 1319 (1998).

[17] G. D. Goodno, V. Astinov, and R. J. D. Miller, "Diffractive optics-based heterodyne-detected grating spectroscopy: Application to ultrafast protein dynamics," J. Phys. Chem. B **103**, 603 (1999).

[18] M. Khalil, N. Demirdöven, O. Golonzka, C. Fecko, and A. Tokmakoff, "A phase-sensitive detection method using diffractive optics for polarization-selective femtosecond Raman spectroscopy," J. Phys. Chem. A **104**, 5711 (2000).

[19] Q.-H. Xu, Y.-Z. Ma, I. V. Stiopkin, and G. R. Fleming, "Wavelength-dependent resonant homodyne and heterodyne transient grating spectroscopy with a diffractive optics method: Solvent effect on the third-order signal," J. Chem. Phys. **116**, 9333 (2002).

[20] D. Keusters, H.-S. Tan, and W. S. Warren, "Role of pulse phase and direction in two-dimensional optical spectroscopy," J. Phys. Chem. A **103**, 10369 (1999).

[21] P. Tian, D. Keusters, Y. Suzaki, and W. S. Warren, "Femtosecond phase-coherent two-dimensional spectroscopy," Science **300**, 1553 (2003).

[22] J. C. Vaughan, T. Hornung, T. Feurer, and K. A. Nelson, "Diffraction-based femtosecond pulse shaping with a two-dimensional spatial light modulator," Opt. Lett. **30**, 323 (2005).

[23] V. Volkov, R. Schanz, and P. Hamm, "Active phase stabilization in Fourier-transform two-dimensional infrared spectroscopy," Opt. Lett. **30**, 2010 (2005).

[24] T. Zhang, X. Li, C. N. Borca, and S. T. Cundiff, "Optical two-dimensional Fourier transform spectroscopy with active interferometric stabilization," Opt. Expr. **13** (2005).

[25] T. Meier, P. Thomas, and S. W. Koch, Coherent semiconductor optics: From basic concepts to nanostructure applications (Springer, Berlin, 2007).

[26] D. S. Chemla and J. Shah, "Many-body and correlation effects in semiconductors," Nature **411**, 549 (2001).

[27] J. Frenkel, "On the transformation of light into heat in solids. I," Phys. Rev. **37**, 17 (1931).

[28] J. Frenkel, "On the transformation of light into heat in solids. II," Phys. Rev. **37**, 1276 (1931).

[29] G. H. Wannier, "The structure of electronic excitation levels in insulating crystals," Phys. Rev. **52**, 191 (1937).

[30] M. Ueta, H. Kanzaki, K. Kobayashi, Y. Toyozawa, and E. Hanamura, Excitonic processes in solids (Springer ser. sol.-stat. sci., vol. 60) (Springer, 1986).

[31] N. Peyghambarian, S. W. Koch, and A. Mysyrowicz, Introduction to semiconductor optics (Prentice Hall, Englewood Cliffs, New Jersey, 1993).

[32] G. Bastard, Wave mechanics applied to semiconductor heterostructures (Halsted Press, 1988).

[33] L. Yang, I. V. Schweigert, S. T. Cundiff, and S. Mukamel, "Two-dimensional optical spectroscopy of excitons in semiconductor quantum wells: Liouville-space pathway analysis," Phys. Rev. B **75**, 125302 (2007).

[34] T. Meier, S. W. Koch, M. Phillips, and H. Wang, "Strong coupling of heavy- and light-hole excitons induced by many-body correlations," Phys. Rev. B **62**, 12605 (2000).

[35] C. F. Klingshirn, Semiconductor optics (3rd ed.) (Springer, 2006).

[36] L. Lepetit, G. Chériaux, and M. Joffre, "Linear techniques of phase measurement by femtosecond spectral interferometry for applications in spectroscopy," J. Opt. Soc. Am. B **12**, 2467 (1995).

[37] L. Schultheis, A. Honold, J. Kuhl, K. Köhler, and C. W. Tu., "Optical dephasing of homogeneously broadened two-dimensional exciton transitions in GaAs quantum wells," Phys. Rev. B **34**, 9027 (1986).

[38] L. Schultheis, J. Kuhl, A. Honold, and C. W. Tu, "Picosecond phase coherence and orientational relaxation of excitons in GaAs," Phys. Rev. Lett. **57**, 1797 (1986).

[39] T. Yajima and Y. Taira, "Spatial optical parametric coupling of picosecond light pulses and transverse relaxation effect in resonant media," J. Phys. Soc. Jap. **47**, 1620 (1979).

[40] K. Leo, M. Wegener, J. Shah, D. S. Chemla, E. O. Göbel, T. C. Damen, S. Schmitt-Rink, and W. Schäfer, "Effects of coherent polarization interactions on time-resolved degenerate four-wave mixing," Phys. Rev. Lett. **65**, 1340 (1990).

[41] V. V. Lozovoy, I. Pastirk, M. G. Comstock, and M. Dantus, "Cascaded free-induction decay four-wave mixing," Chem. Phys. **266**, 205 (2001).

[42] S. T. Cundiff, "Time domain observation of the Lorentz-local field," Laser Phys. **12**, 1073 (2002).

[43] D.-S. Kim, J. Shah, T. C. Damen, W. Schäfer, F. Jahnke, S. Schmitt-Rink, and K. Köhler, "Unusually slow temporal evolution of femtosecond four-wave-mixing signals in intrinsic GaAs quantum wells: Direct evidence for the dominance of interaction effects," Phys. Rev. Lett. **69**, 2725 (1992).

[44] S. Weiss, M.-A. Mycek, J.-Y. Bigot, S. Schmitt-Rink, and D. S. Chemla, "Collective effects in excitonic free induction decay: Do semiconductors and atoms emit coherent light in different ways?," Phys. Rev. Lett. **69**, 2685 (1992).

[45] A. Honold, L. Schultheis, J. Kuhl, and C. W. Tu, "Collision broadening of two-dimensional excitons in a GaAs single quantum well," Phys. Rev. B **40**, 6442 (1989).

[46] H. Wang, K. B. Ferrio, D. G. Steel, P. R. Berman, Y. Z. Hu, R. Binder, and S. W. Koch, "Transient four-wave-mixing line shapes: Effects of excitation-induced dephasing," Phys. Rev. A **49**, R1551 (1994).

[47] B. F. Feuerbacher, J. Kuhl, and K. Ploog, "Biexcitonic contribution to the degenerate-four-wave-mixing signal from a GaAs/$Al_xGa_{1-x}As$ quantum well," Phys. Rev. B **43**, 2439 (1991).

[48] E. O. Göbel, K. Leo, T. C. Damen, J. Shah, S. Schmitt-Rink, W. Schäfer, J. F. Müller, and K. Köhler, "Quantum beats of excitons in quantum wells," Phys. Rev. Lett. **64**, 1801 (1990).

[49] V. Lyssenko, J. Erland, I. Balslev, K.-H. Pantke, B. S. Razbirin, and J. M. Hvam, "Nature of nonlinear four-wave-mixing beats in semiconductors," Phys. Rev. B **48**, 5720 (1993).

[50] J. Feldmann, T. Meier, G. von Plessen, M. Koch, E. O. Göbel, P. Thomas, G. Bacher, C. Hartmann, H. Schweizer, W. Schäfer, and H. Nickel, "Coherent dynamics of excitonic wave packets," Phys. Rev. Lett. **70**, 3027 (1993).

[51] S. T. Cundiff, M. Koch, W. H. Knox, J. Shah, and W. Stolz, "Optical coherence in semiconductors: Strong emission mediated by nondegenerate interactions," Phys. Rev. Lett. **77**, 1107 (1996).

[52] M. U. Wehner, D. Steinbach, and M. Wegener, "Ultrafast coherent transients due to exciton-continuum scattering in bulk GaAs," Phys. Rev. B **54**, R5211 (1996).

[53] D. Birkedal, V. G. Lyssenko, J. M. Hvam, and K. El Sayed, "Continuum contribution to excitonic four-wave mixing due to interaction-induced nonlinearities," Phys. Rev. B **54**, 14250 (1996).

[54] D.-S. Kim, J. Shah, J. E. Cunningham, T. C. Damen, W. Schäfer, M. Hartmann, and S. Schmitt-Rink, "Giant excitonic resonance in time-resolved four-wave-mixing in quantum wells," Phys. Rev. Lett. **68**, 1006 (1992).

[55] X. Li, T. Zhang, C. N. Borca, and S. T. Cundiff, "Many-body interactions in semi-conductors probed by optical two-dimensional Fourier transform spectroscopy," Phys. Rev. Lett. **96**, 057406 (2006).

[56] C. N. Borca, T. Zhang, X. Li, and S. T. Cundiff, "Optical two-dimensional Fourier transform spectroscopy of semiconductors," Chem. Phys. Lett. **416**, 311 (2005).

[57] T. Zhang, I. Kuznetsova, T. Meier, X. Li, R. P. Mirin, P. Thomas, and S. T. Cundiff, "Polarization-dependent optical 2D Fourier transform spectroscopy of semiconductors," Proc. Natl. Acad. Sci. **104**, 14227 (2007).

[58] R. M. Hochstrasser, "Two-dimensional spectroscopy at infrared and optical frequencies," Proc. Natl. Acad. Sci. **104**, 14190 (2007).

[59] W. P. Aue, E. Bartholdi, and R. R. Ernst, "Two-dimensional spectroscopy. Application to nuclear magnetic resonance," J. Chem. Phys. **64**, 2229 (1976).

[60] G. Bodenhausen, R. Freeman, G. A. Morris, and D. L. Turner, "NMR spectra of some simple spin systems studied by two-dimensional Fourier transformation of spin echoes," J. Magn. Reson. **31**, 75 (1978).

[61] B. Vogelsanger, M. Andrist, and A. Bauder, "Two-dimensional correlation experiments in microwave Fourier transform spectroscopy," Chem. Phys. Lett. **144**, 180 (1988).

[62] B. Vogelsanger and A. Bauder, "Two-dimensional microwave Fourier transform spectroscopy," J. Chem. Phys. **92**, 4101 (1990).

[63] G. Wäckerle, S. Appelt, and M. Mehring, "Two-dimensional optical spectroscopy by periodic excitation of sublevel coherence with sub-Doppler resolution," Phys. Rev. A **43**, 242 (1991).

[64] D. Suter, H. Klepel, and J. Mlynek, "Time-resolved two-dimensional spectroscopy of optically driven atomic sublevel coherences," Phys. Rev. Lett. **67**, 2001 (1991).

[65] I. Noda, "Two-dimensional infrared spectroscopy," J. Amer. Chem. Soc. **111**, 8116 (1989).

[66] I. Noda, "Two-dimensional infrared (2D IR) spectroscopy: Theory and applications," Appl. Spectr. **44**, 550 (1990).

[67] R. A. Palmer, C. J. Manning, J. L. Chao, I. Noda, A. E. Dowrey, and C. Marcott, "Application of step-scan interferometry to two-dimensional Fourier transform infrared (2D FT-IR) correlation spectroscopy," Appl. Spectr. **45**, 12 (1991).

[68] L. Lepetit and M. Joffre, "Two-dimensional nonlinear optics using Fourier-transform spectral interferometry," Opt. Lett. **21**, 564 (1996).

[69] O. Golonzka, N. Demirdöven, M. Khalil, and A. Tokmakoff, "Separation of cascaded and direct fifth-order Raman signals using phase-sensitive intrinsic heterodyne detection," J. Chem. Phys. **113**, 9893 (2000).

[70] W. Zhao and J. C. Wright, "Doubly vibrationally enhanced four wave mixing: The optical analog to 2D NMR," Phys. Rev. Lett. **84**, 1411 (2000).

[71] O. Golonzka, M. Khalil, N. Demirdoven, and A. Tokmakoff, "Vibrational anharmonicities revealed by coherent two-dimensional infrared spectroscopy," Phys. Rev. Lett. **86**, 2154 (2001).

[72] N. Demirdöven, M. Khalil, and A. Tokmakoff, "Correlated vibrational dynamics revealed by two-dimensional infrared spectroscopy," Phys. Rev. Lett. **89**, 237401 (2002).

[73] M. Khalil, N. Demirdöven, and A. Tokmakoff, "Obtaining absorptive line shapes in two-dimensional infrared vibrational correlation spectra," Phys. Rev. Lett. **90**, 047401 (2003).

[74] S. M. Gallagher, A. W. Albrecht, J. D. Hybl, B. L. Landin, B. Rajaram, and D. M. Jonas, "Heterodyne detection of the complete electric field of femtosecond four-wave mixing signals," J. Opt. Soc. Am. B **15**, 2338 (1998).

[75] S. M. Gallagher Faeder and D. M. Jonas, "Two-dimensional electronic correlation and relaxation spectra: Theory and model calculations," J. Phys. Chem. A **103**, 10489 (1999).

[76] J. D. Hybl, A. Albrecht Ferro, and D. M. Jonas, "Two-dimensional Fourier transform electronic spectroscopy," J. Chem. Phys. **115**, 6606 (2001).

[77] J. Hybl, A. Yu, D. Farrow, and D. Jonas, "Polar solvation dynamics in the femtosecond evolution of two-dimensional Fourier transform spectra," J. Phys. Chem. A **106**, 7651 (2002).

[78] T. Brixner, J. Stenger, H. M. Vaswani, M. Cho, R. E. Blankenship, and G. R. Fleming, "Two-dimensional spectroscopy of electronic couplings in photosynthesis," Nature **434**, 625 (2005).

[79] T. Brixner, T. Mančal, I. V. Stiopkin, and G. R. Fleming, "Phase-stabilized two-dimensional electronic spectroscopy," J. Chem. Phys. **121**, 4221 (2004).

[80] T. Brixner, I. V. Stiopkin, and G. R. Fleming, "Tunable two-dimensional femtosecond spectroscopy," Opt. Lett. **29**, 884 (2004).

[81] S. Mukamel, Principles of nonlinear optical spectroscopy (Oxford University Press, Oxford, 1995).

[82] S. Mukamel, "Multidimensional femtosecond correlation spectroscopies of electronic and vibrational excitations," Ann. Rev. Phys. Chem. **51**, 691 (2000).

[83] C. Scheurer and S. Mukamel, "Design strategies for pulse sequences in multidimensional optical spectroscopies," J. Chem. Phys. **115**, 4989 (2001).

[84] S. Mukamel and D. Abramavicius, "Many-body approaches for simulating coherent nonlinear spectroscopies of electronic and vibrational excitons," Chem. Rev. **104**, 2073 (2004).

[85] D. M. Jonas, "Two-dimensional femtosecond spectroscopy," Ann. Rev. Phys. Chem. **54**, 425 (2003).

[86] P. Hamm, M. Lim, and R. Hochstrasser, "Structure of the amide I band of peptides measured by femtosecond nonlinear-infrared spectroscopy," J. Phys. Chem. B **102**, 6123 (1998).

[87] S. Woutersen and P. Hamm, "Structure determination of trialanine in water using polarization sensitive two-dimensional vibrational spectroscopy," J. Phys. Chem. B **104**, 11316 (2000).

[88] M. F. Emde, W. P. de Boeij, M. S. Pshenichnikov, and D. A. Wiersma, "Spectral interferometry as an alternative to time-domain heterodyning," Opt. Lett. **22**, 1338 (1997).

[89] J.-P. Likforman, M. Joffre, and V. Thierry-Mieg, "Measurement of photon echoes by use of femtosecond Fourier-transform spectral interferometry," Opt. Lett. **22**, 1104 (1997).

[90] N. Belabas and M. Joffre, "Visible-infrared two-dimensional Fourier-transform spectroscopy," Opt. Lett. **27**, 2043 (2002).

[91] M. Cho, N. F. Scherer, G. R. Fleming, and S. Mukamel, "Photon echoes and related four-wave-mixing spectroscopies using phase-locked pulses," J. Chem. Phys. **96**, 5618 (1992).

[92] J.-Y. Bigot, M.-A. Mycek, S. Weiss, R. G. Ulbrich, and D. S. Chemla, "Instantaneous frequency dynamics of coherent wave mixing in semiconductor quantum wells," Phys. Rev. Lett. **70**, 3307 (1993).

[93] W. P. de Boeij, M. S. Pshenichnikov, and D. A. Wiersma, "Heterodyne-detected stimulated photon echo: Applications to optical dynamics in solution," Chem. Phys. **233**, 287 (1998).

[94] X. Zhu, M. S. Hybertsen, and P. B. Littlewood, "Quantum beats in photon echo from four-waving mixing," Phys. Rev. Lett. **73**, 209 (1994).

[95] M. Koch, J. Feldmann, G. von Plessen, S. T. Cundiff, E. O. Göbel, P. Thomas, and K. Köhler, "Quantum beats in photon echo from four-waving mixing: Koch et al. reply," Phys. Rev. Lett. **73**, 210 (1994).

[96] M. Koch, J. Feldmann, E. O. Göbel, P. Thomas, J. Shah, and K. Köhler, "Coupling of exciton transitions associated with different quantum-well islands," Phys. Rev. B **48**, 11480 (1993).

[97] F. Jahnke, M. Koch, T. Meier, J. Feldmann, W. Schäfer, P. Thomas, S. Koch, E. Göbel, and H. Nickel, "Simultaneous influence of disorder and Coulomb interaction on photon echoes in semiconductors," Phys. Rev. B **50**, 8114 (1994).

[98] A. Euteneuer, E. Finger, M. Hofmann, W. Stolz, T. Meier, P. Thomas, S. W. Koch, W. W. Rühle, R. Hey, and K. Ploog, "Coherent excitation spectroscopy on inhomogeneous exciton ensembles," Phys. Rev. Lett. **83**, 2073 (1999).

[99] S. T. Cundiff, M. Koch, J. Shah, W. H. Knox, and W. Stolz, "Coherent Excitation of Magnetoexciton Wavepackets," phys. stat. sol. b **206**, 77 (1998).

[100] D. Gammon, E. S. Snow, and D. S. Katzer, "Excited state spectroscopy of excitons in single quantum dots," Appl. Phys. Lett. **67**, 2391 (1995).

[101] D. Gammon, E. S. Snow, and D. S. Katzer, "Naturally formed GaAs quantum dots," Surf. Sci. **362**, 814 (1996).

[102] B. V. Shanabrook, D. S. Katzer, and D. Park, "Homogeneous linewidths in the optical spectrum of a single Gallium Arsenide quantum dot," Science **273**, 87 (1996).

[103] D. Gammon, E. S. Snow, B. V. Shanabrook, D. S. Katzer, and D. Park, "Fine structure splitting in the optical spectra of single GaAs quantum dots," Phys. Rev. Lett. **76**, 3005 (1996).

[104] D. Gammon, A. L. Efros, T. A. Kennedy, M. Rosen, D. S. Katzer, D. Park, S. W. Brown, V. L. Korenev, and I. A. Merkulov, "Electron and nuclear spin interactions in the optical spectra of single GaAs quantum dots," Phys. Rev. Lett. **86**, 5176 (2001).

[105] D. S. Chemla, J.-Y. Bigot, M.-A. Mycek, S. Weiss, and W. Schäfer, "Ultrafast phase dynamics of coherent emission from excitons in GaAs quantum wells," Phys. Rev. B **50**, 8439 (1994).

[106] I. D. Abella, N. A. Kurnit, and S. R. Hartmann, "Photon echoes," Phys. Rev. **141**, 391 (1966).

[107] L. Yang and S. Mukamel, "Two-dimensional correlation spectroscopy of two-exciton resonances in semiconductor quantum wells," Phys. Rev. Lett. **100**, 057402 (2008).

[108] M. L. Cowan, J. P. Ogilvie, and R. J. D. Miller, "Two-dimensional spectroscopy using diffractive optics based phased-locked photon echoes," Chem. Phys. Lett. **386**, 184 (2004).

[109] J. C. Vaughan, T. Hornung, K. W. Stone, and K. A. Nelson, "Coherently controlled ultrafast four-wave mixing spectroscopy," J. Phys. Chem. A **111**, 4873 (2007).

[110] K. Gundogdu, K. W. Stone, D. B. Turner, and K. A. Nelson, "Multidimensional coherent spectroscopy made easy," Chem. Phys. **341**, 89 (2007).

[111] C. Dorrer, N. Belabas, J.-P. Likforman, and M. Joffre, "Spectral resolution and sampling issues in Fourier-transform spectral interferometry," J. Opt. Soc. Am. B **17**, 1795 (2000).

[112] A. V. Oppenheim, A. S. Willsky, and H. S., Signals and systems (2nd ed.) (Prentice Hall, 1996).

[113] R. W. Boyd, Nonlinear optics, 2nd ed. (Academic Press, 2002).

[114] F. Bloch, "Nuclear induction," Phys. Rev. **70**, 460 (1946).

[115] V. A. Sautenkov, H. van Kampen, E. R. Eliel, and J. P. Woerdman, "Dipole-dipole broadened line shape in a partially excited dense atomic gas," Phys. Rev. Lett. **77**, 3327 (1996).

[116] T. Guenther, C. Lienau, T. Elsaesser, M. Glanemann, V. M. Axt, T. Kuhn, S. Eshlaghi, and A. D. Wieck, "Coherent nonlinear optical response of single quantum dots studied by ultrafast near-field spectroscopy," Phys. Rev. Lett. **89**, 057401 (2002).

[117] J. M. Shacklette and S. T. Cundiff, "Nonperturbative transient four-wave-mixing line shapes due to excitation-induced shift and excitation-induced dephasing," J. Opt. Soc. Am. B **20**, 764 (2003).

[118] H. Haug and S. W. Koch, Quantum theory of the optical and electronic properties of semiconductors, 2nd ed. (World Scientific, Singapore, 1993).

[119] I. Kuznetsova, T. Meier, S. T. Cundiff, and P. Thomas, "Determination of homogeneous and inhomogeneous broadening in semiconductor nanostructures by two-dimensional Fourier-transform optical spectroscopy," Phys. Rev. B **76**, 153301 (2007).

[120] J. J. Olivero and R. L. Longbothum, "Empirical fits to the Voigt line width: a brief review," J. Quant. Spec. Radi. Trans. **17**, 233 (1977).

[121] T. Zhang, A. D. Bristow, I. Kuznetsova, T. Meier, P. Thomas, and S. T. Cundiff, "Direct determination of exciton homogeneous and inhomogeneous linewidths in semiconductor quantum wells with two-dimensional Fourier transform spectroscopy," in Quantum Electronics and Laser Science Conference (QELS), San Jose, CA, May 4-9, 2008.

[122] I. Kuznetsova and P. Thomas, private communication.

[123] M. Z. Maialle and L. J. Sham, "Interacting electron theory of coherent nonlinear response," Phys. Rev. Lett. **73**, 3310 (1994).

[124] V. M. Axt and A. Stahl, "A dynamics-controlled truncation scheme for the hierarchy of density matrices in semiconductor optics," Z. Phys. B **93**, 195 (1994).

[125] C. Sieh, T. Meier, A. Knorr, F. Jahnke, P. Thomas, and S. W. Koch, "Influence of carrier correlations on the excitonic optical response including disorder and microcavity effects," Eur. Phys. J. B **11**, 407 (1999).

[126] V. M. Axt and T. Kuhn, "Femtosecond spectroscopy in semiconductors: A key to coherences, correlations and quantum kinetics," Rep. Prog. Phys. **67**, 433 (2004).

[127] N. H. Kwong, I. Rumyantsev, R. Binder, and A. L. Smirl, "Relation between phenomenological few-level models and microscopic theories of the nonlinear optical response of semiconductor quantum wells," Phys. Rev. B **72**, 235312 (2005).

[128] C. Sieh, T. Meier, F. Jahnke, A. Knorr, S. W. Koch, P. Brick, M. Hübner, C. Ell, J. Prineas, G. Khitrova, and H. M. Gibbs, "Coulomb memory signatures in the excitonic optical Stark effect," Phys. Rev. Lett. **82**, 3112 (1999).

[129] E. Finger, S. Kraft, M. Hofmann, T. Meier, S. W. Koch, W. Stolz, W. W. Rühle, and A. Wieck, "Coulomb correlations and biexciton signatures in coherent excitation spectroscopy of semiconductor quantum wells," phys. stat. sol. b **234**, 424 (2002).

[130] I. Kuznetsova, Investigation of semiconductor nanostructures using optical two-dimensional Fourier-transform spectroscopy, PhD thesis Philipps Universität, Marburg, Germany (2007).

[131] A. L. Smirl, M. J. Stevens, X. Chen, and O. Buccafusca, "Heavy-hole and light-hole oscillations in the coherent emission from quantum wells: Evidence for exciton-exciton correlations," Phys. Rev. B **60**, 8267 (1999).

[132] M. E. Donovan, A. Schülzgen, J. Lee, P.-A. Blanche, N. Peyghambarian, G. Khitrova, H. M. Gibbs, I. Rumyantsev, N. H. Kwong, R. Takayama, Z. S. Yang, and R. Binder, "Evidence for intervalence band coherences in semiconductor quantum wells via coherently coupled optical Stark shifts," Phys. Rev. Lett. **87**, 237402 (2001).

[133] T. F. Albrecht, K. Bott, T. Meier, A. Schulze, M. Koch, S. T. Cundiff, J. Feldmann, W. Stolz, P. Thomas, S. W. Koch, and E. O. Göbel, "Disorder mediated biexcitonic beats in semiconductor quantum wells," Phys. Rev. B **54**, 4436 (1996).

[134] J. C. Kim, D. R. Wake, and J. P. Wolfe, "Thermodynamics of biexcitons in a GaAs quantum well," Phys. Rev. B **50**, 15099 (1994).

[135] L. Yang, T. Zhang, A. D. Bristow, S. T. Cundiff, and S. Mukamel, "Isolating excitonic Raman coherence in semiconductors using two-dimensional correlation spectroscopy," submitted to J. Chem. Phys.

[136] G. S. Engel, T. R. Calhoun, E. L. Read, T.-K. Ahn, T. Mančal, Y.-C. Cheng, R. E. Blankenship, and G. R. Fleming, "Evidence for wavelike energy transfer through quantum coherence in photosynthetic systems," Nature **446**, 782 (2007).

[137] K. B. Ferrio and D. G. Steel, "Raman quantum beats of interacting excitons," Phys. Rev. Lett. **80**, 786 (1998).

[138] S. A. Hawkins, E. J. Gansen, M. J. Stevens, A. L. Smirl, I. Rumyantsev, R. Takayama, N. H. Kwong, R. Binder, and D. G. Steel, "Differential measurements of Raman coherence and two-exciton correlations in quantum wells," Phys. Rev. B **68**, 035313 (2003).

[139] A. G. V. Spivey, C. N. Borca, and S. T. Cundiff, "Correlation coefficient for dephasing of light-hole excitons and heavy-hole excitons in GaAs quantum wells," Sol. Stat. Comm. **145**, 303 (2008).

[140] M. O. Scully and M. S. Zubairy, Quantum optics (Cambridge University Press, Cambridge, 1997).

[141] V. M. Axt and S. Mukamel, "Nonlinear optics of semiconductor and molecular nanostructures; a common perspective," Rev. Mod. Phys. **70**, 145 (1998).

[142] J. Khurgin, "Electro-optical switching and bistability in coupled quantum wells," Appl. Phys. Lett. **54**, 2589 (1989).

[143] X. Li, T. Zhang, S. Mukamel, R. P. Mirin, and S. T. Cundiff, "Investigation of electronic coupling in semiconductor double quantum wells using optical two-dimensional Fourier transform spectroscopy," in preparation.

[144] I. H. Tan, G. L. Snider, L. D. Chang, and E. L. Hu, "A self-consistent solution of Schrödinger–Poisson equations using a nonuniform mesh," J. Appl. Phys. **68**, 4071 (1990).

[145] P. C. Becker, H. L. Fragnito, C. H. B. Cruz, R. L. Fork, J. E. Cunningham, J. E. Henry, and C. V. Shank, "Femtosecond photon echoes from band-to-band transitions in GaAs," Phys. Rev. Lett. **61**, 1647 (1988).

[146] A. Lohner, K. Rick, P. Leisching, A. Leitenstorfer, T. Elsaesser, T. Kuhn, F. Rossi, and W. Stolz, "Coherent optical polarization of bulk GaAs studied by femtosecond photon-echo spectroscopy," Phys. Rev. Lett. **71**, 77 (1993).

[147] J. Wühr, V. M. Axt, and T. Kuhn, "Nonperturbative Coulomb correlations generated by simultaneous excitation of excitonic and band-to-band continuum transitions," Phys. Rev. B **70**, 155203 (2004).

[148] T. Zhang, X. Li, S. T. Cundiff, R. P. Mirin, and I. Kuznetsova, "Polarized optical two-dimensional Fourier transform spectroscopy of semiconductors," in Ultrafast Phenomena XV, Proceedings of the 15th International Conference, Pacific Grove, USA, Jul. 30 - Aug. 4, 2006, edited by P. Corkum, D. Jonas, R. J. D. Miller, and A. M. Weiner volume 88 pp. 368–370 Springer 2007.

[149] W. Schäfer and M. Wegener, Semiconductor optics and transport phenomena (Springer, Berlin, 2002).

[150] V. M. Axt and A. Stahl, "The role of the biexciton in a dynamic density matrix theory of the semiconductor band edge," Z. Phys. B **93**, 205 (1994).

[151] X. Chen, W. J. Walecki, O. Buccafusca, D. N. Fittinghoff, and A. L. Smirl, "Temporally and spectrally resolved amplitude and phase of coherent four-wave-mixing emission from GaAs quantum wells," Phys. Rev. B **56**, 9738 (1997).

[152] Y. Z. Hu, R. Binder, S. W. Koch, S. T. Cundiff, H. Wang, and D. G. Steel, "Excitation and polarization effects in semiconductor four-wave-mixing spectroscopy," Phys. Rev. B **49**, 14382 (1994).

[153] M. Zanni, N.-H. Ge, Y. S. Kim, and R. M. Hochstrasser, "Two-dimensional IR spectroscopy can be designed to eliminate the diagonal peaks and expose only the crosspeaks needed for structure determination," Proc. Natl. Acad. Sci. **98**, 11265 (2001).

[154] I. Kuznetsova, P. Thomas, T. Meier, T. Zhang, X. Li, R. P. Mirin, and S. T. Cundiff, "Signatures of many-particle correlations in two-dimensional Fourier-transform spectra of semiconductor nanostructures," Sol. Stat. Comm. **142**, 154 (2007).

[155] M. Lindberg, Y. Z. Hu, R. Binder, and S. W. Koch, "$\chi^{(3)}$ formalism in optically excited semiconductors and its applications in four-wave-mixing spectroscopy," Phys. Rev. B **50**, 18060 (1994).

[156] S. Weiser, T. Meier, J. Möbius, A. Euteneuer, E. J. Mayer, W. Stolz, M. Hofmann, W. W. Rühle, P. Thomas, and S. W. Koch, "Disorder-induced dephasing in semiconductors," Phys. Rev. B **61**, 13088 (2000).

[157] L. Yang and S. Mukamel, "Revealing exciton-exciton couplings in semiconductors using multidimensional four-wave mixing signals," Phys. Rev. B **77**, 075335 (2008).

[158] F. Rossi and T. Kuhn, "Theory of ultrafast phenomena in photoexcited semiconductors," Rev. Mod. Phys. **74**, 895 (2002).

[159] M. Khalil, N. Demirdoven, and A. Tokmakoff, "Coherent 2D IR spectroscopy: Molecular structure and dynamics in solution," J. Phys. Chem. A **107**, 5258 (2003).

[160] M. D. Webb, S. T. Cundiff, and D. G. Steel, "Observation of time-resolved picosecond stimulated photon echoes and free polarization decay in GaAs/AlGaAs multiple quantum wells," Phys. Rev. Lett. **66**, 934 (1991).

[161] D. Zigmantas, E. L. Read, T. Mančal, T. Brixner, A. T. Gardiner, R. J. Cogdell, and G. R. Fleming, "Two-dimensional electronic spectroscopy of the B800CB820 light-harvesting complex," Proc. Natl. Acad. Sci. **103**, 12672 (2006).

[162] C. N. Borca, A. G. VanEngen Spivey, and S. T. Cundiff, "Anomalously fast decay of the LH-HH exciton Raman coherence," phys. stat. sol. b **238**, 521 (2003).

[163] H. P. Wagner, W. Langbein, and J. M. Hvam, "Mixed biexcitons in single quantum wells," Phys. Rev. B **59**, 4584 (1999).

[164] M. Phillips and H. Wang, "Coherent oscillation in four-wave mixing of interacting excitons," Sol. Stat. Comm. **111**, 317 (1999).

[165] X. Li, Y. Wu, D. Steel, D. Gammon, T. H. Stievater, D. S. Katzer, D. Park, C. Piermarocchi, and L. J. Sham, "An all-optical quantum gate in a semiconductor quantum dot," Science **301**, 809 (2003).

[166] S. Yokojima, T. Meier, V. Chernyak, and S. Mukamel, "Femtosecond four-wave-mixing spectroscopy of interacting magnetoexcitons in semiconductor quantum wells," Phys. Rev. B **59**, 12584 (1999).

[167] W.-M. Zhang, T. Meier, V. Chernyak, and S. Mukamel, "Intraband terahertz emission from coupled semiconductor quantum wells: A model study using the exciton representation," Phys. Rev. B **60**, 2599 (1999).

[168] C. N. Borca, T. Zhang, and S. T. Cundiff, "Two-dimensional Fourier transform optical spectroscopy of GaAs quantum wells," in SPIE Proceedings Ultrafast Phenomena in Semiconductors and Nanostructure Materials VIII, edited by K.-T. Tsen, J.-J. Song, and H. Jiang volume 5352 pp. 331–339 SPIE 2004.

[169] T. Zhang, L. Yang, A. D. Bristow, S. Mukamel, and S. T. Cundiff, "Exciton Raman coherence revealed in two-dimensional Fourier transform spectroscopy of semiconductors," in Quantum Electronics and Laser Science Conference (QELS), San Jose, CA, May 4-9, 2008.

[170] M. Cho, "Ultrafast vibrational spectroscopy in condensed phases," Phys. Chem. Comm. **5**, 40 (2002).

[171] N.-H. Ge, M. Zanni, and R. Hochstrasser, "Effects of vibrational frequency correlations on two-dimensional infrared spectra," J. Phys. Chem. A **106**, 962 (2002).

[172] C. Fang, J. Wang, A. K. Charnley, W. Barber-Armstrong, A. B. Smith III, S. M. Decatur, and R. M. Hochstrasser, "Two-dimensional infrared measurements of the coupling between amide modes of an α-helix," Chem. Phys. Lett. **382**, 586 (2003).

[173] G. D. Goodno, G. Dadusc, and R. J. D. Miller, "Ultrafast heterodyne-detected transient-grating spectroscopy using diffractive optics," J. Opt. Soc. Am. B **15**, 1791 (1998).

[174] A. W. Albrecht, J. D. Hybl, S. M. Gallagher Faeder, and D. M. Jonas, "Experimental distinction between phase shifts and time delays: Implications for femtosecond spectroscopy and coherent control of chemical reactions," J. Chem. Phys. **111**, 10934 (1999).

[175] A. W. Albrecht Ferro, J. D. Hybl, S. M. Gallagher Faeder, and D. M. Jonas, "Erratum: 'Experimental distinction between phase shifts and time delays: Implications for femtosecond spectroscopy and coherent control of chemical reactions' [J. Chem. Phys. **111**, 10934 (1999)]," J. Chem. Phys. **115**, 5691 (2001).

[176] P. Hamm, M. Lim, and R. M. Hochstrasser, "Non-markovian dynamics of the vibrations of ions in water from femtosecond infrared three-pulse photon echoes," Phys. Rev. Lett. **81**, 5326 (1998).

[177] D. S. Larsen, K. Ohta, Q.-H. Xu, M. Cyrier, and G. R. Fleming, "Influence of intramolecular vibrations in third-order, time-domain resonant spectroscopies. I. Experiments," J. Chem. Phys. **114**, 8008 (2001).

[178] K. Ohta, D. S. Larsen, M. Yang, and G. R. Fleming, "Influence of intramolecular vibrations in third-order, time-domain resonant spectroscopies. II. Numerical calculations," J. Chem. Phys. **114**, 8020 (2001).

[179] M. K. Lawless and R. A. Mathies, "Excited-state structure and electronic dephasing time of Nile blue from absolute resonance Raman intensities," J. Chem. Phys. **96**, 8037 (1992).

[180] R. M. Hochstrasser, "Multidimensional ultrafast spectroscopy," Proc. Natl. Acad. Sci. **104**, 14189 (2007).

[181] S.-H. Shim, D. B. Strasfeld, Y. L. Ling, and M. T. Zanni, "Automated 2D IR spectroscopy using a mid-IR pulse shaper and application of this technology to the human islet amyloid polypeptide," Proc. Natl. Acad. Sci. **104**, 14197 (2007).

[182] E. L. Read, G. S. Engel, T. R. Calhoun, T. Mančal, T.-K. Ahn, R. E. Blankenship, and G. R. Fleming, "Cross-peak-specific two-dimensional electronic spectroscopy," Proc. Natl. Acad. Sci. **104**, 14203 (2007).

[183] D. V. Kurochkin, S. R. G. Naraharisetty, and I. V. Rubtsov, "A relaxation-assisted 2D IR spectroscopy method," Proc. Natl. Acad. Sci. **104**, 14209 (2007).

[184] B. Auer, R. Kumar, J. R. Schmidt, and J. L. Skinner, "Hydrogen bonding and Raman, IR, and 2D-IR spectroscopy of dilute HOD in liquid D_2O," Proc. Natl. Acad. Sci. **104**, 14215 (2007).

[185] K. Kwak, S. Park, and M. D. Fayer, "Dynamics around solutes and solute solvent complexes in mixed solvents," Proc. Natl. Acad. Sci. **104**, 14221 (2007).

[186] W. Zhuang, D. Abramavicius, D. V. Voronine, and S. Mukamel, "Simulation of two-dimensional infrared spectroscopy of amyloid fibrils," Proc. Natl. Acad. Sci. **104**, 14233 (2007).

[187] H. S. Chung, Z. Ganim, K. C. Jones, and A. Tokmakoff, "Transient 2D IR spectroscopy of ubiquitin unfolding dynamics," Proc. Natl. Acad. Sci. **104**, 14237 (2007).

[188] J. Bredenbeck, J. Helbing, K. Nienhaus, G. U. Nienhaus, and P. Hamm, "Protein ligand migration mapped by nonequilibrium 2D-IR exchange spectroscopy," Proc. Natl. Acad. Sci. **104**, 14243 (2007).